Correlation between structure, doping and performance of thermoelectric materials

Yu Zhao

Dissertation submitted to the faculty of the Virginia Polytechnic Institute and State University in partial fulfillment of the requirements for the degree of

Doctor of Philosophy
In
Materials Science and Engineering

Shashank Priya, Chair
Alex O. Aning
William T. Reynolds, Jr.
Scott T. Huxtable

August 14th, 2014
Blacksburg, VA

Keywords: thermoelectric, nanostructure, thermal conductivity, doping, electrical properties

Correlation between structure, doping and performance of thermoelectric materials

Yu Zhao

ABSTRACT

Thermoelectric materials can convert thermal energy into electrical energy and vice-versa. They are widely used in energy harvesters, thermal sensors, and cooling systems. However, the low efficiency and high cost of the known material compositions limit their widespread utilization in electricity generation applications. Therefore, there is a strong interest in identifying new thermoelectric materials with high figure of merit. In response to this need, this dissertation works on the synthesis, structure, doping mechanism, and thermoelectric properties of zinc oxide (ZnO) and lead tellurium (PbTe). The main focus is on ZnO based materials and in improving their performance. The influences of micro- or nano-structures on thermal conductivity, as well as the correlation between the electrical property and synthesis conditions, have been systematically investigated.

ZnO is a likely candidate for thermoelectric applications, because of its good Seebeck coefficient, high stability at high temperature, non-toxicity and abundance. Its main drawbacks are the high thermal conductivity (κ) and low electrical conductivity (σ). To decrease κ, two novel structures—namely, precipitate system and layered-and-correlated grain microstructure—have been proposed and synthesized in ZnO. The mechanisms

governing the nature of thermal behavior in these structures have been explored and quantified. Due to strong phonon scattering, the nano-precipitates can reduce the thermal conductivity of ZnO by 73%. The ZnO with layered-and-correlated grains can further reduce κ by about 52%, which compares favorably with the dense ZnO with nano-precipitates. The figure of merit of this ZnO based structure was 0.14×10^{-3} K^{-1} at 573 K. In order to understand the electrical behavior in nanostructured ZnO, the impact of Al doping and chemical defects in ZnO under different synthesis conditions were studied. Under varying sintering temperatures, atmospheres and initial physical conditions, ZnO exhibited very distinct σ. High temperature, lack of oxygen, vacuum condition, and chemically synthesized powder can increase the carrier concentration and σ of ZnO.

A promising alloy system, PbTe-PbS, undergoes natural phase separation by nucleation and growth, and spinodal decomposition depending on the thermal treatment. The correlation between the thermal treatment, structure, and the thermoelectric properties of $Pb_{0.9}S_{0.1}Te$ has been studied. The nano-precipitates were incorporated in the annealed alloy resulting in a 40% decrease in κ. The PbS precipitation was shown to enhance the carrier concentration and improves the Seebeck coefficient. These concomitant effects result in a maximum ZT of 0.76 at 573 K.

Throughout the thesis, the emphasis was on understanding the impact of the microstructures on thermal conductivity and the effect of the synthesis condition on thermal and electrical properties. The process and control variables identified in this study provide practical ways to optimize the figure of merit of ZnO and PbTe materials for thermoelectric applications.

Acknowledgements

First, I would like to express my deep gratitude to my advisor, Dr. Shashank Priya for his guidance in my studies. He gave research opportunities for me to explore and guided me intelligently and patiently. I benefited so much from his vast knowledge and great passion in science. As an international student, I also greatly appreciate his support and encouragement throughout my graduate studies.

I am grateful to my committee members: Dr. Alex Aning, Dr. William Reynolds, and Dr. Scott Huxtable. During my PhD study, Dr. Aning gave me so much help and provided critical suggestions on my research. He always asked about my progress and encourages me every time when we meet. Dr. Reynolds generously shared his knowledge about nanoscale characterization and material calculation, and very patiently guided me to think and analyze characterization questions. Dr. Huxtable also patiently explained thermoelectric measurement processes and was generous with his time and talent. All their advice, experience, and encouragement have contributed significantly to my research and understanding of fundamentals.

I would like to extend my appreciation to Dr. Hsin Wang, Dr. Andy Miner, and Dr. Armin Feldhoff for their great support on thermoelectric measurements and valuable discussion on thermoelectric materials; to Dr. Giti Khodaparast for her kind help on Hall Effect measurement and encouragement; to Dr. Hao-Hsiang Liao and Mr. Jue Wang for help on property measurements, useful discussions and support with my research; to Dr. BoYun Jang for help with PL measurements; to Mr. Charles Farley for his help with Raman spectra measurement; and to Mr. Cary Hill for particle size distribution analysis. I

want to thank Stephen McCartney, Christopher Winkler, and Andrew Giordani from the Nanoscale Characterization and Fabrication Laboratory of Virginia Tech who taught me material characterization and aided in my analyses. I also want to thank Dr. David Clark, Dr. Celine Hin, and Dr. Kathy Lu for valuable discussions.

I would like to thank my colleagues in the Center for Energy Harvesting Materials and Systems over the years. Many thanks go to: Dr. Yongke Yan, Dr. Ashok Kumar, Dr. Su Chul Yang, Dr. Deepam Maurya, Dr. Bo Chen, Dr. Chee-sung Park, Dr. Kyung-Hoon Cho, Dr. Vishwas Bedekar, Dr. Ronnie Varghese, Dr. Shashaank Gupta, Dr. Dragan Avirovik, Dr. Daniel Apo, Dr. Alex Villanueva, Dr. Beomjin Yoo, Dr. Saranya Dorairajan, Yuan Zhou, Hyun-Cheol Song, Christian Folgar, Nathan Sharpes, Lijuan Yang, and the visiting scholars Reema Gupta and Preeyakarn Eaksuwanchai. I also want to thank all my friends at Blacksburg and at home. Thank you for the help and friendship.

The excellent faculty and staff have facilitated my research and provided the best resources available. I would also like to thank Kim Grandstaff, Beth Howell, Ai Fukushima, Erin Singleton, and Lauren Mills.

Most importantly, I want express my deepest appreciation to my parents, Guoda Zhao and Yanan Yao. Without their love, support, and encouragement, I would not have been able to complete this journey. I am very grateful to my husband, Mingkai Mu. He has given me endless care and support in my life and throughout the course of this doctoral program.

Finally, I acknowledge the financial support from provided by The National Science Foundation and Department of Energy Thermoelectrics Partnership.

Table of Contents

List of Figures

List of Tables

Chapter1 Introduction and Literature Review

1.1 Introduction

There is an urgent need for alternative energy sources with high efficiency to fulfill increasing energy demands and reduce the environment pollution. Every year, more than 50% of the overall energy dissipates, mainly in the form of waste heat. The process of thermal energy harvesting can recover part of the energy from the waste heat so that the better overall process efficiency can be achieved. Thermoelectric technology is being investigated as a viable option for thermal energy harvesting.

Thermoelectric effect is an encouraging technique to convert heat into electricity and vice-versa[1]. Thermoelectric devices offer several distinct advantages over other alternatives. These plusses include their relatively silent operation, their long lifetime, the fact that they do not rely on harmful gaseous components or other materials that may require periodic replenishment, as well as their ability to function well under high temperatures and in constrained or even radioactive environments. Thus, thermoelectric devices show promise for thermal energy harvesting and waste energy recovery applications in transportation, industrial or commercial processes.

For good exchange efficiency between heat and electricity, thermoelectric materials need to feature a high figure of merit (ZT), which requires high Seebeck coefficient, high electrical conductivity and low thermal conductivity[2, 3]. Since the 1950's, numerous studies have been conducted towards discovering new thermoelectric materials and microstructures for achieving better figure of merit[4]. Currently, the materials with best thermoelectric property are alloy semiconductors. However, they suffer from oxidation and stability problems at high temperature in air and are harmful to humans and the

environment. Because of low efficiency and the high cost of raw materials, thermoelectric materials are still the bottleneck for wide application.

This research principally focuses on the thermoelectric oxide, zinc oxide (ZnO), which has good Seebeck coefficient[5], features good stability at high temperature, is abundant, and can be prepared simply. In order to reduce the high thermal conductivity[6] of ZnO, the phonon scattering phenomenon of precipitate structures at nano/micro-scale and grain size has been investigated. Unlike metallic alloys that should be dense to avoid oxidation, thermoelectric ZnO with porous structures have been proposed and the effect of the porous layer on the thermal conductivity has been explored. The electrical properties of ZnO with special microstructures have also been evaluated under varying sintering conditions (temperature, atmosphere, and initial physical condition). For comparative analysis of precipitate system, another thermoelectric alloy, PbTe-PbS, was studied and the effect of precipitate on thermal conductivity was identified.

1.2 Literature Review

1.2.1 Discovery of thermoelectric effect

A basic understanding of thermoelectric devices (thermoelectric generators and thermoelectric refrigerators) has been developed over several decades since the discovery of thermoelectric effect. Specifically, three separate effects have been identified: the Seebeck effect, the Thomson effect, and the Peltier effect.

Seebeck effect corresponds to the conversion of temperature differences directly into electricity[1, 7]. In 1821, Thomas Johann Seebeck discovered that a compass needle was deflected by a closed loop formed by two dissimilar conductors when a temperature

gradient was applied by heating one junction of the conductor[8]. He contributed this phenomenon to magnetism; in fact, the phenomenon was due to the magnetism formed by an electric current that was generated by the temperature difference. In 1851, Lord Kelvin observed a change of heat within a single homogeneous material in a temperature gradient when an electric current passed through it, which is referred to as Thomson effect[1, 8]. Conversely, an electrical voltage is generated in certain materials subjected to a temperature gradient, referred to as absolute Seebeck effect[7]. Absolute Seebeck effect is the basic principle of thermoelectric generator. Peltier effect is the reverse process of the Seebeck effect: heat is absorbed or released when a current crosses at an electrified interface of two different conductors[1, 8]. This effect is utilized in the thermoelectric refrigeration/cooling application.

1.2.1.1 Thermoelectric device and figure of merit

A typical thermoelectric generator or refrigerator consists of a group of *n*-type and *p*-type thermoelectric elements[8], shown in Figure 1.1.

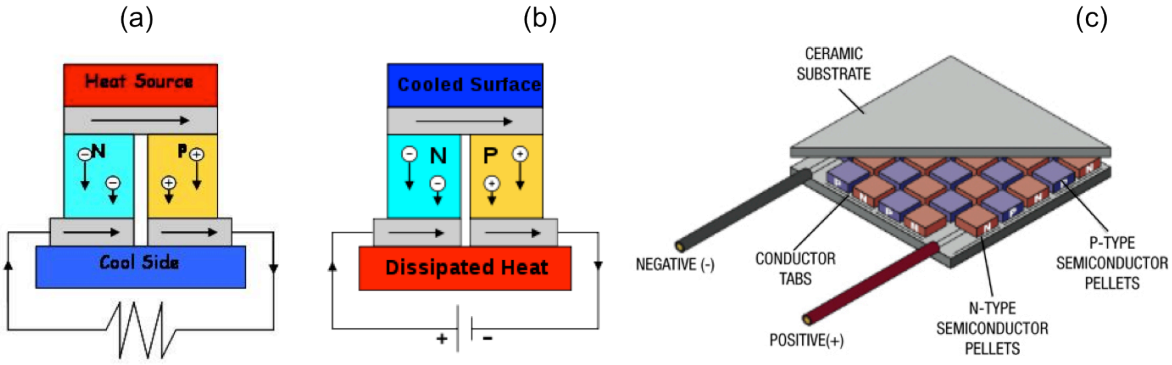

Figure 1.1 Thermoelectric circuit[8] composed of two materials with different Seebeck coefficients (*p*-type and *n*-type semiconductors), configured as (a) thermoelectric

generator and (b) thermoelectric refrigerator; (c) thermoelectric generator module construction, including a number of *p*-type and *n*-type couples.

The efficiency of a thermoelectric generator is given as[9]:

$$\eta = \frac{(T_1 - T_2)}{T_1}\frac{(M-1)}{(M + T_2/T_1)} \tag{1.1}$$

$$M = (1 + ZT_M)^{1/2}, T_M = (T_1 + T_2)/2$$

where T_1 and T_2 are absolute temperatures on two ends of a material. It is obvious that the efficiency increases with M, which is related to figure of merit *Z*. Figure 1.2 displays the efficiency variation with temperature at different figure of merit *Z*.

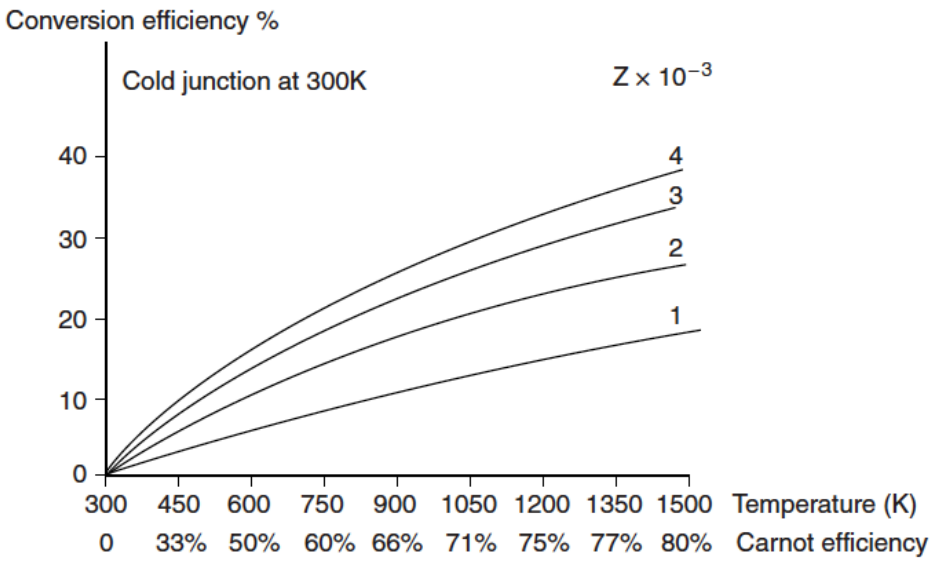

Figure 1.2 Generator efficiency as a function of temperature and figure of merit of thermocouple material[1].

Similarly, the performance coefficient for a refrigerating couple is as follows[9]:

$$\phi_{max} = \frac{T_1[(1+ZT_M)^{\frac{1}{2}} - T_2/T_1]}{(T_2 - T_1)[(1+ZT_M)^{\frac{1}{2}} + 1]} \tag{1.2}$$

Very often in literature, the Z and T are combined together. Efficiency depends on material properties through the dimensionless figure of merit[9]:

$$ZT = \frac{S^2\sigma}{\kappa}T \tag{1.3}$$

For a pair of materials, it corresponds to equation 1.4[9]:

$$Z = \frac{\left(S_p - S_n\right)^2}{\left[\left(\rho_p\kappa_p\right)^{\frac{1}{2}} + \left(\rho_n\kappa_n\right)^{\frac{1}{2}}\right]^2} \tag{1.4}$$

where S is Seebeck coefficient, σ is electrical conductivity, κ is thermal conductivity, ρ is electrical resistivity, and T is absolute temperature. To maximize ZT, S must be large so that a small temperature difference can create a large voltage, σ must be large in order to minimize the joule-heating losses, and κ should be small to reduce the heat leakage and maintain a temperature difference. The difficulty arises because all these parameters S, σ, and κ are mutually exclusive[3]. The nature of S, σ, and κ is discussed in detail below.

1.2.1.2 Electric transport

Seebeck coefficient represents a material's ability to generate a voltage in response to a temperature gradient across the material[8]:

$$S = -\frac{\Delta V}{\Delta T} \tag{1.5}$$

Thermodynamically, Seebeck coefficient is the amount of net entropy transported per charge carrier[10]. Carrier diffusion and phonon drag effects cause the transfer of entropy in the presence of a temperature gradient[11, 12]. In the solid-state material, carriers (electrons or holes) diffuse to the cold side, leaving immobile nuclei at the hot side. This process gives rise to an electric field and a voltage difference. The separation of charges creates an electric field that drives the carriers in opposite direction (from the hot to the cold side), after which the two forces reach a balance. In the case of certain materials, an increase in temperature difference can rebuild the balance, thus leading to an increase in voltage. On the other hand, a temperature difference also creates a heat current where phonons propagate down the temperature gradient[11, 13]. Phonon-carrier interactions make the phonons impart some energy to the diffusing carriers via momentum transfer; therefore, the phonons "drag" (slow down) the carrier moving from cold side to hot side. This effect contributes to the total Seebeck coefficient. Phonon-drag can produce a large enhancement of the Seebeck coefficient at low temperature, and this contribution wanes with increasing temperature[11].

In the case of metal, the calculation of *S* can be derived from Mott equation[14]:

$$S = \frac{\pi^2}{3} \cdot \frac{{k_B}^2 T}{e} \cdot \frac{dln\sigma(E)}{dE}\Big|_{E=E_f} \tag{1.6}$$

where T is temperature, k_B is the Boltzmann's constant, e is electronic charge, and σ is the conductivity when the electron energy, E, is equal to the Fermi energy, E_F. The value of Seebeck coefficient is dependent on the electronic band structure, and the curvature of the electronic density of states (DOS) at Fermi energy[2, 14]. Only carriers near the Fermi level can participate in electronic transport. With variations of DOS around the Fermi energy, the temperature gradient is able to create a chemical potential difference that drives the carrier transport.

For metals or degenerate semiconductors (parabolic band, energy-independent scattering approximation), Seebeck coefficient is also given by equation 1.7[2, 15]:

$$S = \frac{8\pi^2 k_B^2}{3eh^2} m^* T \left(\frac{\pi}{3n}\right)^{2/3} \tag{1.7}$$

where m^* is effective mass, h is the Planck constant, and n is carrier concentration. Electrical conductivity represents a material's ability to conduct an electric current, which is calculated via the following equation:

$$\sigma = en\mu;\ n = g(E)f(E);\ \mu = \frac{e\tau}{m^*} \tag{1.8}$$

where n is carrier concentration, μ is carrier mobility, $g(E)$ is electronic density of state, $f(E)$ is the Fermi function, and τ is relaxation time.

The product of the square of Seebeck coefficient and electrical conductivity is referred to as power factor of thermoelectric materials. Both S and σ are related to carrier concentration based on equations (1.7) and (1.8), while the dependence of n is the opposite. An increase in electrical conductivity with carrier concentration will simultaneously lead to a decrease in the Seebeck coefficient. To maximize ZT, the power factor should be optimized with respect to carrier concentration[2].

1.2.1.3 Thermal transport

Thermal conductivity (κ) describes a material's ability to to conduct heat. It is the sum of heat transported by phonons and electrons in solid materials ($\kappa = \kappa_{latt} + \kappa_{elec}$). Lattice thermal conductivity (κ_{latt}) is understood as the "intrinsic" thermal conductivity of materials, which is attributed to the lattice vibration, known as phonons. Lattice thermal conductivity is the only parameter not related to charge carrier concentration. Considering scattering of phonons, the physical approximation of κ_{latt} is given in equation 1.9[16]:

$$\kappa_{latt} = \frac{1}{3} Cvl \tag{1.9}$$

where C is the specific heat at constant volume, l is phonon mean free path, and v is the average velocity of sound in a material.

The electronic contribution to thermal conductivity is dependent on the electrical conductivity, which is expressed by the Wiedemann-Franz law[17]:

$$\kappa_{elec} = L\sigma T \tag{1.10}$$

where L is the Lorenz number, typically with a value of L_0= 2.45x10^{-8} WΩK^{-2}. The Weidmann-Franz law limits the ratio σ/κ_{elec}^{2}. The highest value of Z is reached when the product $\rho\kappa$ is minimized. For a given thermoelectric couple pair, a simple exercise is to show that $\rho\kappa$ is minimized when[9]:

$$\frac{L_n A_p}{L_p A_n} = \left(\frac{\rho_p \kappa_n}{\rho_n \kappa_p}\right)^{1/2} \tag{1.11}$$

where the L and A are the length and cross-sectional area, respectively, of thermoelectric legs in devices. One desirable feature is that lattice thermal conductivity is much larger than electronic thermal conductivity for semiconductors. Thereby, κ_{latt} reduction is a significant strategy to find and design thermoelectric materials[2]. One primary focus of this dissertation is to identify lattice thermal conductivity reduction by enhancing phonon scattering using nano- and micro- inclusions.

1.2.2. Improvement in *Z* and current thermoelectric materials

In order to obtain high conversion efficiency, thermoelectric materials should exhibit both high figure of merit Z, and good stability in the desired operating temperature regime. But as mentioned earlier, it is difficult to control the parameters S, σ, and κ individually (S and σ; σ and κ). Some semiconductors are considered to be good thermoelectric materials. They exhibit larger Seebeck coefficient than conductors because

of their excess electron or hole density and high carrier concentration alterability. In addition, their moderate carrier concentration leads to relatively low κ values. Most importantly κ_{latt} is relative larger compared with κ_{elec} in these materials.

One strategy for obtaining a high figure of merit is by reducing lattice thermal conductivity. Generally low lattice thermal conductivity is related to complex crystal structure and heavy elements in materials[2]. For example, skutterudites and clathrates feature a crystal framework with cages, which are filled by heavy elements, resulting in thermal conductivity decrease[2]. Another scheme for achieving a high figure of merit relies on modifying the power factor ($S^2\sigma$) by utilizing band structure engineering[2]. The power factor is the product of Seebeck coefficient and electrical conductivity. With an increase in carrier density, electrical conductivity increases but Seebeck coefficient decreases. There is a maximum in power factor in the carrier concentration range of 10^{19} to 10^{21} cm^{-3} [2]. Further, Heremans predicted and experimentally proved that a distortion (resonant levels close to the Fermi level) of the electronic density of states by doping enhances the Seebeck coefficient in PbTe alloy without deteriorating electrical conductivity[18]. Even though calculations for the presence of resonant levels using doping elements in other materials have been published as well, few experimental results are available to validate those predictions.

Theoretical predictions[19] were made in early 1990s' that ZT could be enhanced by synthesizing nanostructured materials. Phonon scattering by nanostructure is an effective method to lower lattice thermal conductivity. When the structure scale is close to the phonon mean free path of a given material, effective phonon scattering would occur resulting in a significant reduction in lattice thermal conductivity. Electron mean free

path is usually shorter than that of phonon, so that the negative influence on electrical conductivity is not severe. Based upon this underlying concept, the thermal conductivity in some thermoelectric alloys was successfully decreased and *ZT* larger than 1 was achieved[20].

Table 1.1 lists the thermoelectric materials extensively investigated in the literature exhibiting reasonable figure of merit. Commonly used thermoelectric materials, such as chalcogenide compounds represented as Bi(Sb)Te[21], PbTe[22] and related alloys, show best figure of merit at low and medium temperature range (room temperature to 800K). Skutterudites Co_4Sb_{12}[23] and SiGe[24] compounds have shown good performance in the medium-to-high temperature range (800-1200K). Recently, metal oxides such as $NaCoO_2$ [25], $Ca_3Co_4O_9$ [26], ZnO [5], and $SrTiO_3$ [27], have been investigated as a cost-effective rare-earth free substitute. Table 1.1 also summarizes various nanostructures that have been used in thermoelectric materials over the past several decades. Both low-dimension nanostructured alloys (e.g. superlattice, quantum dots superlattice, and nanowire) and bulk alloys with nanoscale features (e.g. nanocrystals and nanograins) have been designed and studied.

Table 1.1 Thermoelectric properties and synthesis method for common thermoelectric materials (Based upon the reported experimental literature results)

Composition and structure	***z*T**	**T (K)**	***κ*** **($Wm^{-1}K^{-1}$)**	***S*** **(μV/K)**	***σ*** **(S/cm)**	**Preparation method**	**Ref.**
Alloy based-low dimensional structure							
Bi_2Te_3 / Sb_2Te_3 superlattice	2.4	300	0.22 (⊥)			Low Temperature	[21]

						growth	
$(Bi,Sb)_2(Te,Se)_3$ QDSL	1.6	300		-219		MBE	[28]
PbTe/ $Pb_{1-x}Eu_xTe$ thin film quantum well	1.23 (2D)					MBE	[29]
Si nanowire	1	200	~0.8			SNAP process	[30, 31]
SiGe QDSL			0.9			MBE	[32]
Alloy based-bulk, crystal							
Bi_2Te_3 bulk with nanograin	1.4	372	1	220	500	BM, HP	[33]
$Bi_{0.52}Sb_{1.48}Te_3$ bulk with nanograin	1.56	300	0.7	230	700	Melt spinning SPS	[34]
$CsBi_4Te_6$ (SbI_3 doping) single crystal	0.82	225	~2	~170	~2520	Single crystal growth	[35]
$AgPb_mSbTe_{m+2}$ (m=18) bulk with nanodots	2.2	800	~1	-335	~200	Ingot synthesis, annealing	[36]
PbTe-2%Sb, 0.5%Pb bulk with nanodots	1.4	700	~1.4	-200	750	Melting and rapid cooling	[37]
$(GeTe)_{0.8}(Ag_2Te)_{0.4}(Sb_2Te_3)_{0.6}]_{0.2}$ bulk	1.68	700				HP	[38]
$Na_{0.95}Pb_mSbTe_{m+2}$	~1.7	650	1	339	165	Ingot	[39]

(m=22) bulk with nanodots						synthesis	
PbTe-12%PbS-2%Na bulk with nanodots	1.8	800	~1.2	~280	~300	Melting and rapid cooling	[40]
PbTe-2%Tl	1.5	773	1	320	~100	Ingot synthesis	[18]
PbTe-6% CaTe bulk with nanodots	1.5	765	~1.1	~250	~265	Ingot synthesis, annealing	[41]
PbTe-1%CdTe-0.055% PbI_2 bulk with nanodots	1.2	720	~1.1	-225	~400	Ingot synthesis, annealing	[42]
PbTe-2% SrTe bulk with nanodots	2.2	900	0.96	280	~300	Ingot synthesis, annealing	[43]
Ag_9TlTe_5 bulk	1.23	700	0.22	319	38	Ingot synthesis, sintering	[44]
$Ba_{0.08}La_{0.05}Yb_{0.04}Co_4Sb_{12}$ Skutterudites bulk	1.7	850	2.6	-195	1300	Ingot synthesis, SPS	[45]
$Ba_{0.14}In_{0.23}Co_4Sb_{11.84}$ Skutterudites bulk	1.34	850	~2.5	-200	900	Ingot synthesis, SPS	[46]
$Yb_{14}MnSb_{11}$ single crystal	1	1223	7.5	190	180	Single crystal growth	[47]
SiGe bulk with nanograin	1.3	1172	~2.5	-240	~600	HP	[48]

Zn_4Sb_3 bulk	1.3	670	6.5	190	500	Ingot synthesis, HP	[49]
BaGaGe crystal	1.35	900	~1.3	-170	600	Czochralski	[50]
$(Zr_{0.5}Hf_{0.5})_{0.5}Ti_{0.5}NiSn_{1-y}Sb_y$ bulk	1.5	700	~2.6	-310	~660	Arc melting, HP	[51]
$Cu_{2-x}Se$ bulk with liquid-like structure	1.5	1000	~0.8	300	125	Ingot synthesis	[52]
Oxide based							
$Na_xCoO_{2-\delta}$ single crystal	1.2	800	5.1	200	1900	Flux grow method	[25]
$(Ca_2CoO_3)_{0.7}CoO_2$ single crystal	0.87	973	3	240	430	Single crystale growth	[26]
$(Ca_{2.8}Ag_{0.05}Lu_{0.15})Co_4O_9$ lamella grain with nano inclusion	0.6	1100	1.4	230	~140	BM, SPS	[53]
$SrTi_{0.8}Nb_{0.2}O_3$ bulk	0.37	1000					[54]
$Zn_{0.96}Al_{0.02}Ga_{0.02}O$ bulk	0.65	1247	~5	~-250	~417	Solid reaction	[55]
ZnO-2% Al bulk with nano inclusion	0.44	1000	1.8	-310	~85	Chemical synthesis, Solid reaction	[56]

* k is thermal conductivity measured in watts per kelvin per meter; S is Seebeck coefficient measured in volt per kelvin; σ *is* electrical conductivity measured in siemens per meter; T is absolute temperature measured in kelvin.

* MBE: Molecular beam epitaxy; BM: Ball milling; SPS: Spark plasma sintering; SNAP: superlattice nanowire pattern transfer

* QDSL: quantum dots superlattice

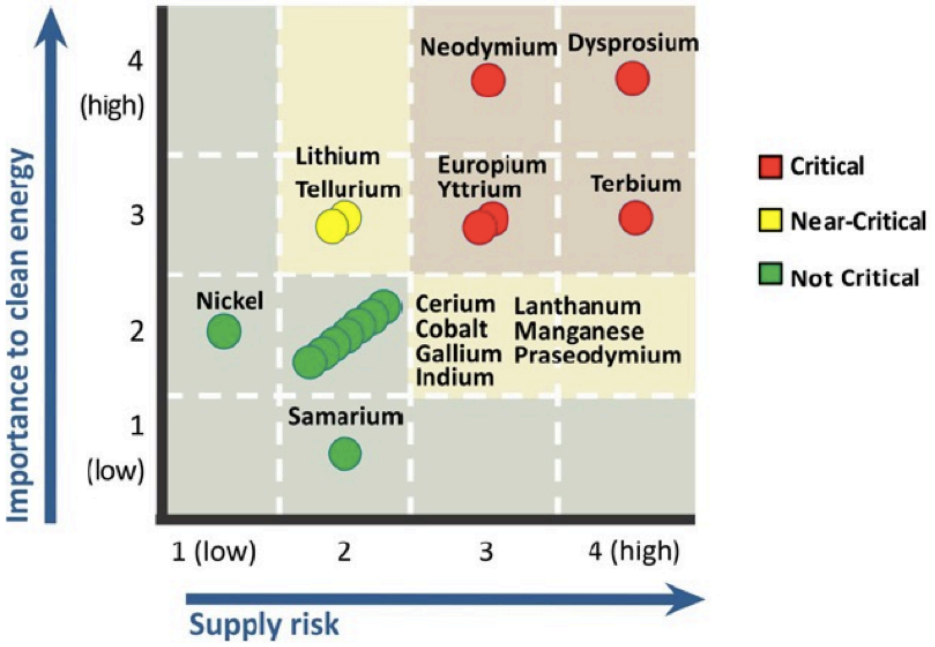

Figure 1.3 Medium-Term (2015-2025) criticality materix. Taken from: DOE's 2011 Critical Materials Strategy[57].

From the literature (Table 1.1), BiTe-based, PbTe-based and some other alloys provide improved figure of merit higher than 1.5. However the poor stability in air prevents their commercialization in high temperature platforms. Further, for expanding the range of application, the cost of thermoelectric materials is as important as performance properties. High cost of materials and complex fabrication processes limits the potential of many alloy compositions. Figure 1.3 illustrates the likely availability of raw materials.

The main element "Te" used in both Bi_2Te_3 and PbTe based alloys belongs to the critical material category that is currently or will continue to be in short supply. Silver, which is used for inducing nanodots in PbTe is a precious metal. Some other rare earth elements, such as Yb, La, Ce, are also in short supply. Moreover, complex synthesis techniques (like thin film deposition processes and spark plasma sintering) are neither practical nor economically feasible for commercial use. Also, important to note is that some elements are harmful to both humans and the environment, such as Pb and Tl. All these considerations and restrictions connected to the design of thermoelectric materials severely limit their practical and widespread commercial application.

When factors in the requirement of high temperature operation with the various restrictions discussed above, it is clear that the list of potential candidates is limited to oxides such as $Ca_3Co_4O_9$, ZnO, and several others. Over the past few decades, there has been a great progress in understanding of *n*- and *p*-type polycrystalline oxides, as shown in Figure 1.4. These oxides have excellent stability in air at high temperature. They employ non-toxic elements that are abundantly available. In short, these thermoelectric oxides represent a cheaper and environmentally friendly alternative for thermal energy harvesting. Comparing the thermoelectric properties of alloy- and oxide-based thermoelectric materials, the main challenges for polycrystalline oxides are relatively high thermal conductivity and low electrical conductivity. They exhibit optimized *ZT* that is only half or one-third of that of alloys. The nanostructuring approach promises to address these challenges and offers the opportunity to improve the performance of these cost-effective materials.

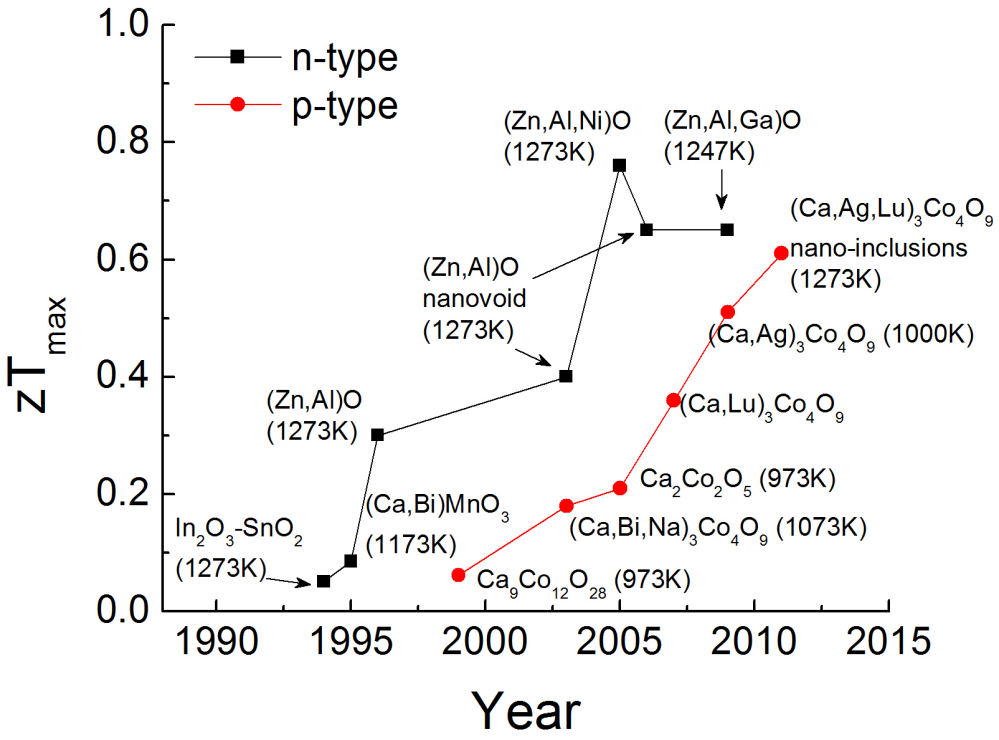

Figure 1.4 Development of *n*-type[5, 55, 58-62] and *p*-type[53, 63-66] polycrystalline oxide thermoelectric materials.

Among thermoelectric oxides, zinc oxide is a promising *n*-type semiconductor[5]. ZnO has a good Seebeck coefficient around 200μV/K at room temperature[5]. The Zn-O bond has significant covalent nature, and thereby ZnO exhibits large carrier mobility compared with other oxides. Further, bulk ZnO has excellent stability at high temperature in air. These various properties make it an excellent candidate for use in high temperature thermoelectric materials. Current research on thermoelectric ZnO is discussed in detail in Section 1.2.4.

1.2.3. Role of nanostructure in improving thermoelectric properties

1.2.3.1 Influence of nanostructure on thermal conductivity

Phonons are quanta of excitations in normal modes of lattice vibration motion, which transport heat through solid materials. They are termed as acoustic or optical phonons according to their polarization. Acoustic phonons mainly contribute towards lattice thermal conductivity. At low temperature, the contribution from transverse acoustic (TA) phonons is dominant, while longitudinal acoustic (LA) phonons prevail at higher temperature[67].

Thermal conductivity describes the ability of a material to conduct heat, which is largely determined by phonon distribution. Phonons encounter resistance through various scattering processes, such as scattering by other phonons, lattice disorders (vacancies, interstitials, and dopants), boundaries, and charge carriers, all of which restrict the phonon mean free path. Phonons have a spectrum of wavelengths, all contributing to the value of κ. Phonons with short wavelength are scattered by impurity atoms while larger structure such as interfaces scatter long wavelength phonons[68]. Based on specific heat of solids, κ_{latt} is expressed by the following relation[16]:

$$\kappa_{latt} = Cv^2\tau \tag{1.12}$$

where C and v denote the specific heat and velocity of sound at macroscopic level, respectively. Phonon relaxation time, τ, as a result of various scattering processes, can be expressed by Matthiessen's rule:

$$\tau_c^{-1} = \sum_i \tau_i^{-1} \tag{1.13}$$

The phonon mean free path is an important variable in understanding thermal conductivity. Considering phonons boundary scattering, Casimir obtained the following equation for κ_{latt}[16]:

$$\kappa_{latt} = \frac{1}{3} Cvl \tag{1.14}$$

$$l_c^{-1} = \sum_i l_i^{-1}$$

The mean free path *l* represents the distance between "collisions" through which phonons are randomly scattered. Phonon scattering through various processes governs the phonon mean free path and the relaxation time, which, in turn, modifies phonon group velocity ($v_g = l/\tau$) and their propagation direction. Both the parameters *l* and τ are closely related to microscopic properties. For electron, the mean free path is shorter than phonon mean free path. Therefore, suitable strategy is possible where structure can selectively scatter phonons without strongly affecting electrons.

Nanostructure in materials is possible to cause a spatial confinement of phonons, and in turn, influence phonon dispersion. Structure with a scale much larger than the mean free path of phonons does not significantly influence phonon movement. However, if feature size is similar or smaller than the mean free path of phonons, the acoustic phonons can be scattered effectively[68]. In other words, long-wavelength phonons (low-frequency, long mean free path) would be inhibited from transport, and only high-frequency phonons

would be allowed to propagate. Nanoscale systems have length-scale-directional limitations. For example, in 0D systems all longitudinal and transverse phonons are confined; phonon movement in 1D systems is restricted in two directions; and in 2D systems one dimension acts as a constraint for phonon movement. The dimensional constraints associated with phonon propagation, which are illustrated in Figure 1.5, can significantly reduce phonon transport in the constrained direction—providing that the constrained length scale is less than the phonon mean free path (nanoscale).

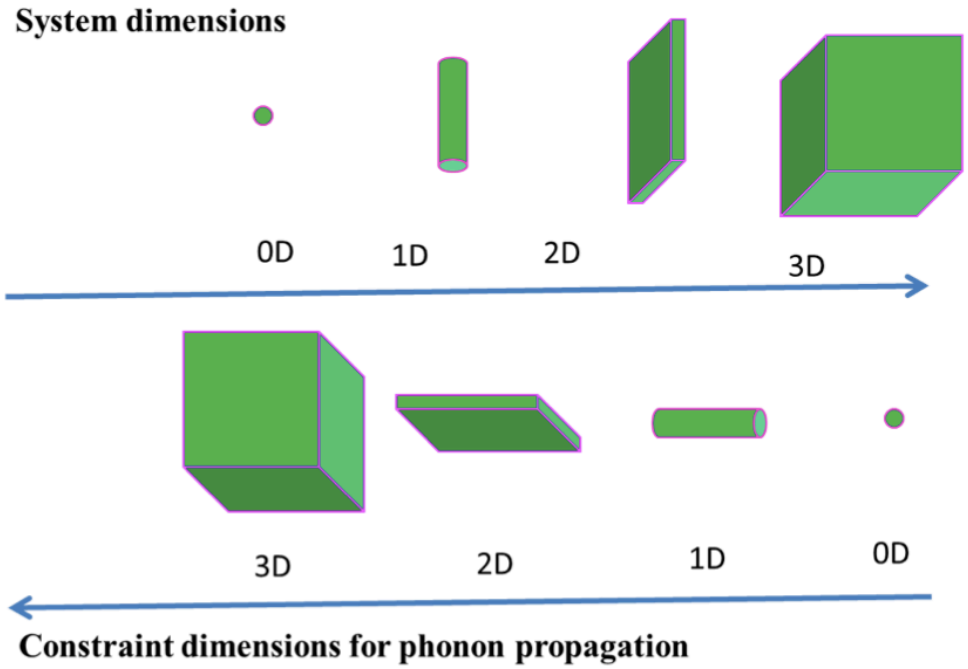

Figure 1.5 The 0D, 1D, 2D and 3D systems showing the directional constraints for phonon propagation.

Surface roughness (δ) of interface also plays a critical role in reducing lattice thermal conductivity. For a nanowire of diameter '*d*' with scattering parameter "*p*", the mean free path due to the boundary scattering is expressed as[69]:

$$l_b = (1 + p)d/(1 - p) \tag{1.15}$$

where, *p* is given by Ziman's relation $p = \exp(-16\pi^3\delta^2/\lambda^2)$ in which δ is surface roughness and λ is phonon wavelength. The thermal conductivity values investigated by Martin et al.[70] were found to have $(d/\delta)^2$ dependence. Research has also shown that strong phonon confinement could be achieved in the nanostructures coated with elastically dissimilar materials[71]. Thus both reduced dimensions and increased surface roughness can reduce lattice thermal conductivity.

Several studies have been conducted to examine the influence of nanostructures on electron scattering in semiconductors[67]. At the macroscopic level, the electronic contribution to heat conduction is given by following relation[72]:

$$\kappa_{elec} = \pi^2 k_b^2 \frac{N_f}{2E_f T} \tag{1.16}$$

where N_f is the number of free electrons, k_b is the Boltzmann constant, E_f is the Fermi energy level and T is the absolute temperature.

The ratio of electronic thermal conductivity to phonon thermal conductivity can be expressed as[72]:

$$\kappa_{elec}/\kappa_{latt} = 5N_f\Theta_D^3/24\pi^2 NT^2T_f \quad (1.17)$$

where N_f/N is the average number of free electrons contributed by each atom, T_f is Fermi temperature and Θ_D is Debye temperature. With increase in temperature, the contribution of lattice vibration to thermal conductivity increases. If one examines the temperature ($T_o = \sqrt{(5N_f \ \Theta_D^3/24 \ \pi^2 \ N \ T^2 \ T_f)}$), when electrons have significant effect on thermal conductivity say $\kappa_{elec} = \kappa_{latt}$, the temperature value is only a few percent of the Debye temperature. This result indicates that electron contribution to thermal conductivity can only be realized at very low temperatures.

Therefore, lattice thermal conductivity, which represents a major contributor to overall thermal conductivity, can be significantly decreased by strong phonon scattering on nanostructure. The first experimental evidence that confirmed this effect is related to low-dimensional thermoelectric materials[21]. Breakthroughs in *ZT* values (larger than 2) have been mostly realized through the study of low-dimensional thermoelectric materials (e.g., 2D superlattice and quantum dots superlattice shown in Figure 1.6a and b, and 1D nanowire), well summarized in a recent review paper [73]. These studies have provided a fundamental understanding of the effect of nanostructure on thermoelectric properties. Nevertheless, most low-dimensional thermoelectric materials are fabricated by slow and complex thin film deposition techniques and hard to keep the temperature gradient. One of the important outcomes of prior research has been a push towards developing strategies for achieving nanostructured bulk materials. Two types of bulk nanostructures (nanodots in Figure 1.6c and nanograins in Figure 1.6d) have been extensively investigated in recent years.

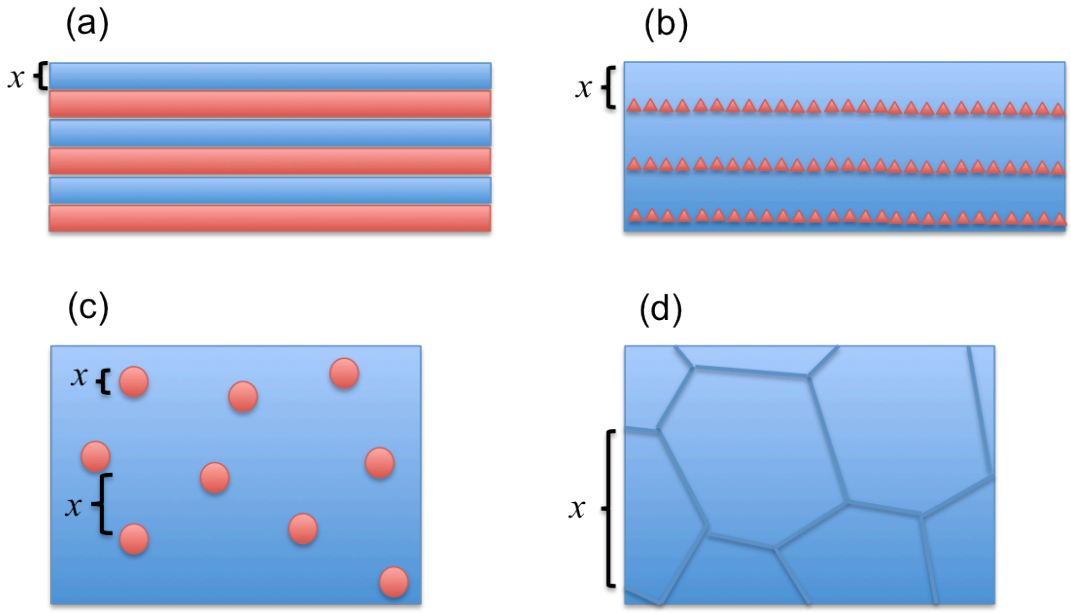

Figure 1.6 Schematic images of nanostructures: (a) superlattice, (b) quantum dots superlattice, (c) bulk with nanodots, (d) bulk with nanograins. The sizes of *x* are all in nanoscale.

1.2.3.2 Nanostructures in low dimensional materials

In the early 1990s, theoretical calculations were made on Bi_2Te_3 quantum-well superlattice structures (a schematic for ultra-thin multi-layers is shown in Figure 1.6a), which predicted significant enhancement in *ZT* because of the highly anisotropic effective-mass tensor[74]. Although no direct experimental results confirmed these calculations, a significant reduction in lattice thermal conductivity of the cross-plane in super-lattice structure was observed in thermoelectric materials[21]. The superlattice period around 50Å for Bi_2Te_3/Se_2Te_3 alloy is desirable for minimizing κ_{latt}[21]. Phonon blocking by 2D superlattice has been demonstrated in SiGe alloys too[75,76]. Acoustic impedance

mismatch at interface plays a determining role in phonon reflection. The suppression of perpendicular thermal transport by internal reflection and acoustic mismatch was predicted by calculation[77]. Other examples of significantly reduced lattice thermal conductivity in supperlattice systems include PbTe/$PbTe_xSe_{1-x}$[78], GaAs/$Al_xGa_{1-x}As$[79], and $In_xGa_{1-x}As/Al_yIn_zGa_{1-z}As$[80]. Phonon mean free path *l*, is restricted in superlattice structure leading to lower thermal diffusivity as described in the studies noted above.

Similar to superlattice structures, a quantum dot superlattice structure (QDSL) also features ultra-thin multi-layers (the schematic structure is shown in Figure 1.6b, and real images in Ge/Si are shown in Figure 1.7). In contrast to a superlattice structure, one type of layers in a QDSL consists of randomly distributed nanodots of a second phase (Figure 2.7b). It is also termed nano dot superlattice (NDSL). Compared with the superlattice structure, QDSL has larger size roughness feature, which is effective for scattering mid-to-long-wavelength phonons. The PbSeTe/PbTe QDSL material has been shown to provide improved thermoelectric performance owing to the presence of PbSe quantum nanodot layers embedded in a PbTe matrix[81]. According to the Debye-Callaway model, half heat is carried by phonons with the mean free path less than 19 nm in PbTe alloys[82]. The κ_{latt} minimization has been attributed to short phonon mean free paths in PbTe. The phonon mean free path in Si is larger than 100 nm[32], so Si exhibits larger lattice thermal conductivity in comparison to PbTe-based alloys; phonons with a mid-long mean free path carry a large fraction of heat. Therefore the QDSL could exhibit more effective phonon scattering performance in Si-based materials. A minimum κ_{latt} of 0.9 $Wm^{-1}K^{-1}$ is achieved in Si by nanodot layers with 1.2 nm height and 70% relative surface density,

with the period of 3.6 nm[32]. The minimum κ_{latt} is well below the κ_{latt} limit in amorphous Si of 2.5 $Wm^{-1}K^{-1}$ [32].

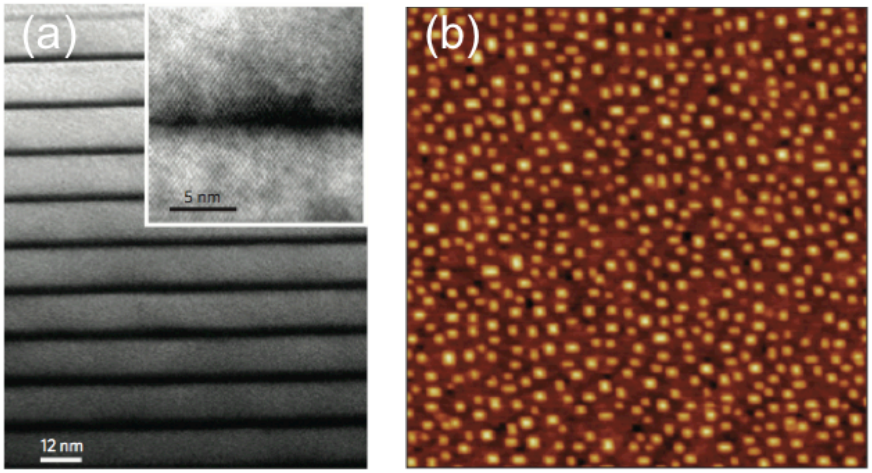

Figure 1.7 (a) Bright-field TEM image of a Ge/Si sample with superlattice period of 12 nm. The dark areas correspond to the Ge layers. The inset shows a high resolution TEM of a nanodot; (b) AFM image of a single Ge/Si(001) dot layer before overgrowth with Si.[32]

Nanowires also influence phonon motion and then drastically reduces thermal conductivity[30, 31]. The Si nanowire maintains similar Seebeck coefficient and electrical conductivity values as bulk Si while exhibiting 100-fold reduction in κ[30]. The decrease of κ depends on diameter and roughness of the nanowire[30]. Lead chalcogenide (PbS, PbSe, PbTe) nanowires were found to exhibit similar reduction in κ with a decrease in the diameter [83].

1.2.3.3 Nanostructures in bulk materials

Bulk materials do not require exact low dimensional geometry. As long as a high density of nanostructures exists, strong phonon scattering would occur to reduce lattice thermal conductivity. Nanostructures such as nanodots (the schematic structure shown in Figure 1.6c) in bulk materials could shorten phonon mean free path. PbTe-based materials provide good examples. Nanodots formations in PbTe-based alloys have been extensively investigated in recent years with modifiers such as Sb[37, 84-86], Bi (BiSb)[85, 86], Pb[37, 86], SnTe[87], Ag_2Te[88], and BaTe[89]. Nearly all nanocrystals in the PbTe-based alloys noted above lead to lattice misfit and large strain (significant acoustic impedance mismatch/roughness). These inclusions block the propagation of mid-to-long-wavelength phonons hence intensely reducing κ_{latt}. Another commonly-studied system, PbTe-PbS alloys, undergoes spinodal decomposition during annealing around 500°C, resulting in semi-coherent heterogeneities in PbTe matrix, as shown in Figure 1.8[90, 91]. When the amount of PbS is relatively high (16% atomic percent), spinodal-laminated structures with the period of about 2 nm are formed. Results show that nanodots are more effective in scattering phonons than the laminate structure[30]. In most cases, however, charge carriers were somewhat scattered leading to a decrease in electrical conductivity. Recently, SrTe nanocrystals were found to provide phonon blocking and charge transmitting functions[43, 92]. Due to a very small valence band offset of PbTe and SrTe, there was no negative influence on the electrical conductivity as a result of SrTe crystals.

In comparison to the quantum dots superlattice, the nanodots in bulk thermoelectric materials have two advantages: (i) the synthesis process is simple, which is suitable for large-scale fabrication, and (ii) the structure is thermodynamically stable.

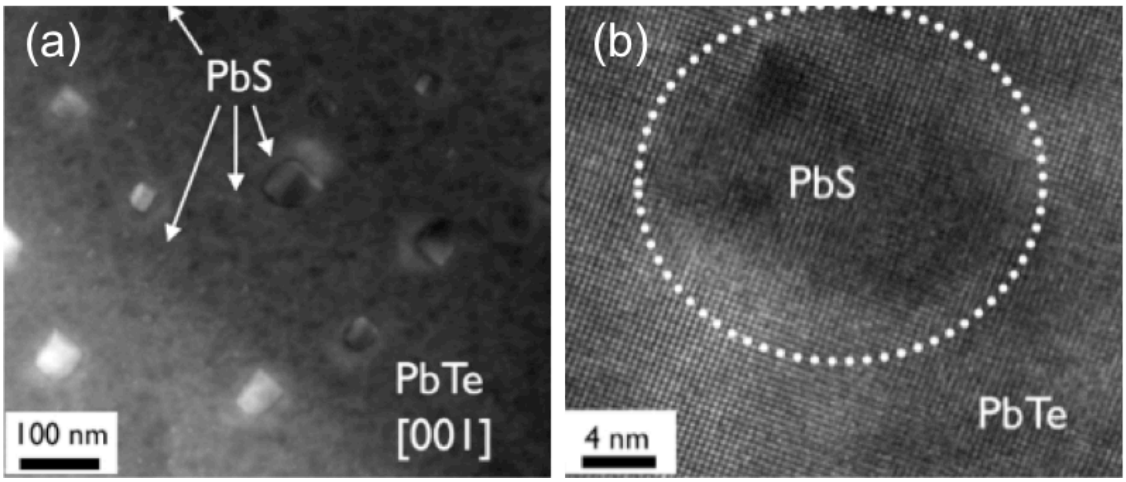

Figure 1.8 (a) STEM image of PbTe-PbS 8% showing two PbS particle sizes in PbTe matrix: larger about 100 nm and smaller 2-10 nm; (b) HRTEM image of precipitates (smaller particles in (a)) located in PbTe matrix.[90]

Based on successful applications in bulk thermoelectric alloys, the nano-inclusion concept has also been applied to thermoelectric oxides in order to produce low thermal conductivity also. $Ca_3Co_4O_9$ ceramic systems with textured microstructures have been obtained by using SPS (spark plasma sintering)[93]. During the ball-milling process and SPS, a spontaneously oriented lamellar structure (Figure 1.9a) with Ag inclusions was formed. Grains within the lamellar structure were randomly oriented with high angle boundary[53]. Ag inclusions (Figure 1.9b) with a diameter of 350 nm consisted of both spherical and cubical shape particles. This lamellar grain, together with Ag nano-inclusion and heavy element Eu doping have been shown to result in a 40% decrease in thermal conductivity[53].

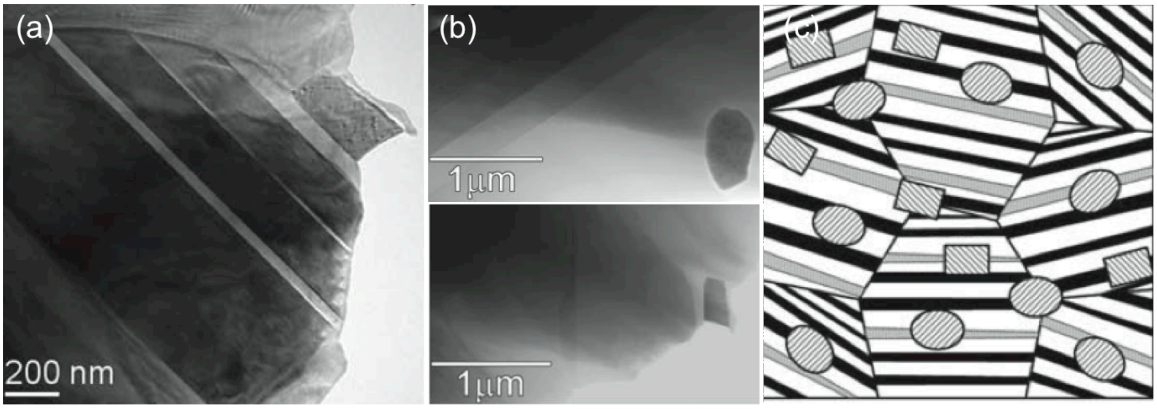

Figure 1.9 (a) BF-TEM images of $Co_3Co_4O_9$ with heavy doping of Ag and Eu; (b) STEM of Ag precipitates in $Co_3Co_4O_9$; (c) Heavily doped aligned lamellar structures with embedded nanosize inclusions in schematic form.[53]

The second method for creating bulk nanocomposites is to develop nanograins in polycrystalline material (the schematic structure is shown in Figure 1.6d). It has been reported that nanosize grains with sharp grain boundaries (Figure 1.10a) in BiSbTe[33] exhibit strong phonon scattering thereby reducing the thermal conductivity by a factor of two. Another interesting experiment is on $Bi_{0.52}Sb_{1.48}Te_3$ ribbons synthesized by melt spinning having grains in the dimension of 5-10 nm dimension, amorphous structures on contact surface and dendritic structure on their free surface[34]. After SPS, the bulk alloy retained all of the noted microstructures in these ribbons, which achieved low thermal conductivity about 0.67 $Wm^{-1}K^{-1}$ with the lattice contribution of 0.26 $Wm^{-1}K^{-1}$ [34]. In a SiGe system, the average phonon mean free path is large to 300 nm[48], and thus the thermal conductivity can be effectively deceased by nanocrystalline (Figure 1.10b).

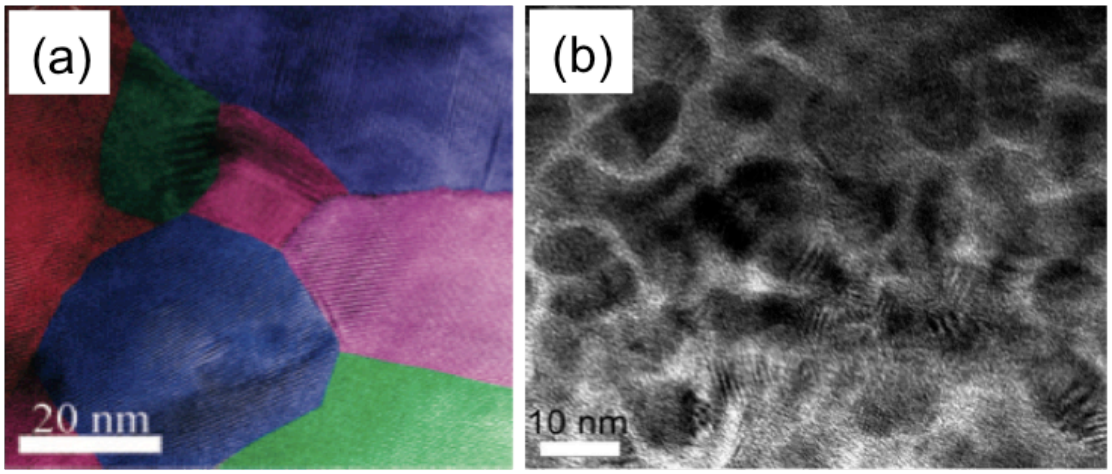

Figure 1.10 TEM images showing (a) nanosize grain, high crystallinity, random orientation, and clean grain boundaries in BiSbTe bulk alloy[33]; (b) nanograins in SiGe bulk alloy[48].

1.2.3.4 Influence of mesoscale structure on thermal conductivity

In actuality, a fraction of the heat is carried by a phonon long mean free path and the micron scale structures have phonon scattering effect also. An investigation of the Si-Ge system[94] with three different grain sizes (10-25μm, 5-10 μm, and less than 5 μm) has shown that the decrease of grain size resulted in a reduction of thermal conductivity. A recent study in PbTe[43] confirmed that an additional reduction in thermal conductivity has been achieved by further scattering of phonons with longer mean free paths (0.1-1μm, mesoscale) by grain boundary, shown in Figure 1.11.

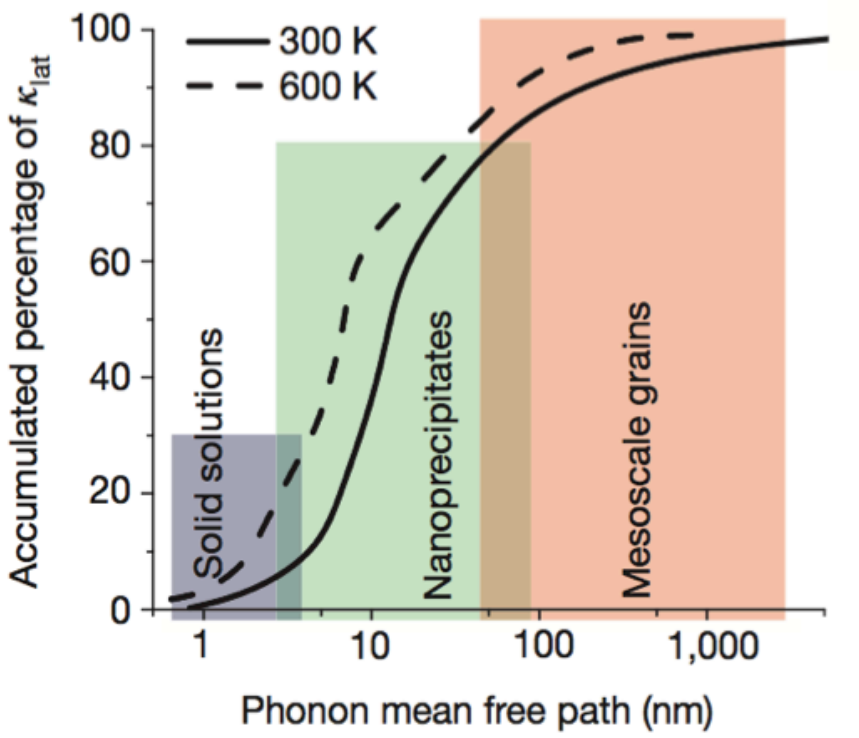

Figure 1.11 Contributions of phonons with different mean free paths to the cumulative value for κ_{latt} in PbTe.[43]

1.2.3.5 Synthesis techniques towards nanostructure

Selecting the appropriate synthesis technique is essential for the fabrication of nanostructures in thermoelectric materials. For low-dimensional systems (0D structure in QDSL, 1D nanowire, and 2D superlattice in thin film), fabrication methods are mostly based upon complex thin film deposition processes. For example, molecular beam epitaxy (MBE) has been applied in the fabrication of several thermoelectric alloys[28, 29, 32] and pulsed laser flash evaporation, ion-beam sputtering, metal organic chemical vapor deposition, molecular beam epitaxy, and electro-deposition techniques have been utilized for the synthesis of bismuth telluride thin films[95]. Low-dimensional materials are not

practical for large-scale commercial use because multi-layer deposition processes are slow and expensive, and it is hard to maintain the temperature difference in thin film. The large-scale fabrication of bulk nanostructured materials with compatible geometry is possible by using simple and mature technologies.

For bulk materials with nanoscale grain size, the fabrication process consists of two steps: (1) synthesis of nano particles and (2) consolidation of the nano particles to form dense body. Small particles can be fabricated using mechanical alloying, hydrothermal reaction, chemical reaction, and melt spinning. High-energy ball-milling method has been used in synthesize BiSbTe and SiGe nano powders[33, 48]. In such cases, nano powders need to be compacted and sintered into dense bulk. In order to prevent rapid grain growth, a high sintering temperature and long sintering time should be avoided. Hot pressing, which is a pressure-assisted sintering process, has been used to prepare PbSe and SiGe polycrystalline materials[48, 96]. By applying pressure, much lower sintering temperature and shorter time are needed for sintering. Using this method, nano powders form a grain boundary and grow into a bulk material, but the grains are still in nanoscale dimension. Spark plasma sintering represents another modification of pressure-assisted sintering process, in which a spark discharges to heat compact samples under high pressure[43].

Although nano powder fabrication, hot pressing and spark plasma sintering are quite mature techniques, there are some challenges for deploying them in the synthesis of alloys with nanograins. Firstly, an inert gas is required to protected metallic alloys from oxidation, especially for alloy nano particles with a very high surface ratio. The density of bulk alloy should be high to prevent it from oxidation and environmental degradation

during high-temperature applications. To achieve high density, a high magnitude of pressure during hot pressing or spark plasma sintering is necessary, increasing the quality and complexity of the equipment needed to carry out this process. Lastly, the small grain is usually not stable at high temperatures. For example, SiGe with nanograins that shows a good figure of merit at relatively high temperature may deteriorate under continuous operation at high temperature.

Phase transformation provides a solution for fabricating nanostructures in bulk materials. Phase transformation processes are driven by Gibbs or Helmholtz free energies, resulting in the entire system's statistical tendency to increase its entropy. Some material compositions are homogenous and stable in liquid state and solid solution. Below temperature of phase transformation, entropic force drives precipitation of insoluble phases from the matrix. This approach has been utilized to fabricate nanostructure in PbTe-based alloys and achieve high thermoelectric performance[36, 37, 39, 40, 42, 43, 84, 85, 90-92]. Composition selection and annealing process are critical for achieving nanostructures. For example, as shown in Figure 1.12, using different regimes of the phase diagram of PbTe-Sb_2Te_3[97], bulk alloys with nanocrystals, lamella structure, oriented epitaxial like interfaces or semi-coherent interfaces can be obtained in figure 1.12. As illustrated by this figure's blue line, with continuous cooling the solubility of Sb_2Te_3 in PbTe decreases, and the Sb_2Te_3 phase begins to precipitate from the PbTe matrix. The size of the precipitates is small since the diffusion process in the solid state is much more difficult than that in the liquid state. For the critical composition (green arrow), annealing below the eutectoid temperature allows metastable phase $Pb_2Sb_6Te_{11}$ to decompose into PbTe and Sb_2Te_3 phases in lamellar structure[97, 98]. Since, the nanodots or

lamellar structures are driven by thermodynamic force, these microstructures are stable in materials.

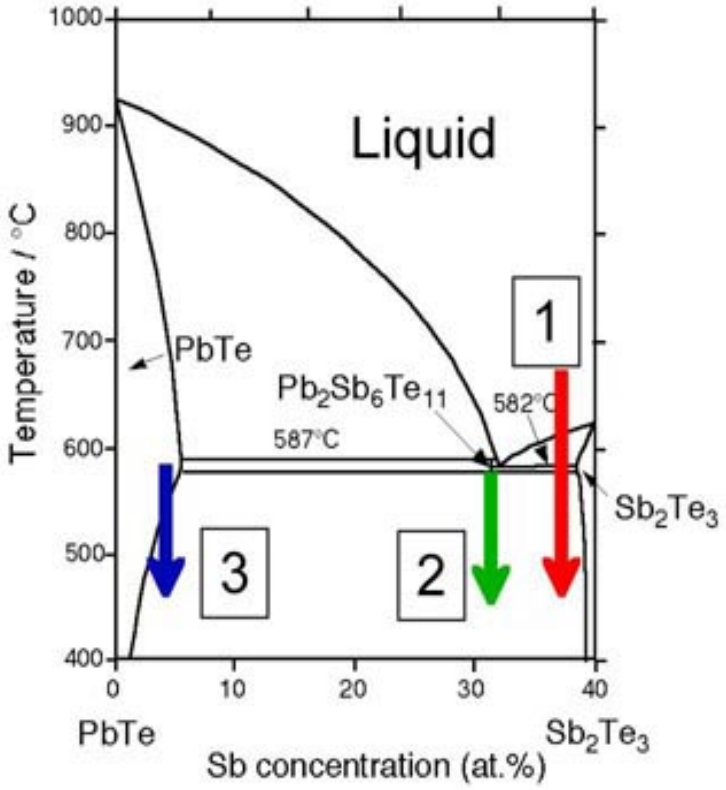

Figure 1.12 Phase diagram of PbTe- Sb_2Te_3[97]. The blue, green and red arrows show different phase transformation during decreasing temperature.

1.2.4 ZnO as a thermoelectric material and challenges

ZnO is a naturally *n*-type wide-band gap semiconductor possessing hexagonal wurtzite-type crystal structure[6]. It is a promising thermoelectric material because of its good Seebeck coefficient (around -200μV/K) and good stability at high temperature in air[5, 6, 99].

The Zn-O bond has a rather covalent character, leading to high carrier mobility among the oxides[6]. However, the simple wurtzite crystal structure and light Zn and O elements give rise to high thermal conductivity in ZnO crystal as large as 100 W/mK at room temperature[6]. The polycrystalline ZnO displays large thermal conductivity of around 50 W/mK according to experimental results[5, 100]. Similar to other thermoelectric oxides, it exhibits low σ because of relatively low carrier concentration compared with alloy semiconductors. Therefore reduction of thermal conductivity and enhancement of electrical conductivity are the primary tasks towards improving the figure of merit of ZnO.

1.2.4.1 Thermal conductivity minimizing

For ZnO, the lattice thermal conductivity contributes 90% or more of the overall thermal conductivity[100]. As discussed in 1.2.3, slowing down phonon propagation in ZnO crystal lattice can become a significant way towards lowering the value of κ. According to previous researches, several methods have been tried to decrease thermal conductivity of ZnO.

It has been observed that the thermal conductivity of ZnO decreases with Al_2O_3 addition[58]. With 5 atom % Al, the thermal conductivity reached below 20 W/mK at room temperature and 11 W/mK at 300 °C. Besides, Co-doping with Ga and Al in ZnO exhibited a reduction in κ to ~ 5 W/mK at 300 °C[55]. A ZnO ceramic with a large concentration of Ga is highly porous, as shown in Figure 1.13a. The strong suppression in the value of κ was attributed to high porosity and a granular texture. The pores impede phonon transport, but tend to deteriorate electrical conductivity as well. Using spark

plasma sintering, Al, Ga dual-doped ZnO bulk can get high density at temperatures of 1223K and above[101]. In this study, samples didn't display as low thermal conductivity as Al, Ga dual-doped ZnO bulk in previous study [101]. The co-addition of Al_2O_3 and NiO was also reported to play a role in decreasing thermal conductivity too, from 12.5 to 10 W/mK at 300 °C[58], which was attributed to defects induced by the substituted atoms, and the grain boundary of the secondary phase. Recently, nano-inclusions have been used as phonon scattering centers in bulk ZnO samples and were found to reduce the thermal conductivity substantially (~ 15% of bulk value at room temperature)[56]. The inclusion is secondary phase precipitates, shown in Figure 1.13b. The reduction of κ was ascribed to ZnO grain boundary, ZnO-$ZnAl_2O_4$ boundary, point defects and porosity[56]. This study, however, did not address which of those factors play the dominant role and how the structure size impacts thermal conduction behavior. More systematic experiments are needed to clarify phonon scattering mechanisms in ZnO.

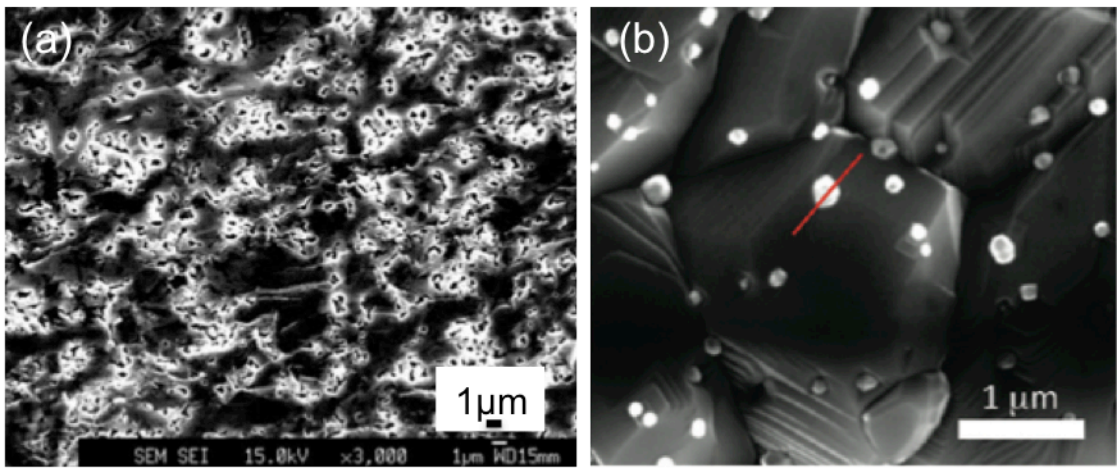

Figure 1.13 (a) SEM micrograph from fracture surfaces of $Zn_{0.73}Al_{0.02}Ga_{0.05}O$ ceramic[55]; (b) SEM micrograph from bulk ZnO nanocomposite pellets obtained by assembly of ZnO nanocrystals with 1 atom % Al (brighter particles are second phase)[56].

Introducing nanograins is another method and several trials have involved in ZnO too. The percentage of heat carried by phonons with a mean free path shorter than L_β has been calculated and is displayed in Figure 1.14[102]. It is obvious that with smaller grain size, more percentage of heat is carried by phonons with smaller mean free path, indicating smaller thermal conductivity based on equation 1.14 (L_β is l). Although doping elements in ZnO can decrease ZnO grain size, it is still in the micron range. Using pulsed electric current sintering, very low temperature (200 °C) was applied to obtain bulk ZnO having nanograins[103]. The resulting small grains (about 30nm) resulted in a low thermal conductivity ~ 5 W/mK at room temperature[103], because of enhanced boundary scattering. However, its electrical conductivity deteriorated more than 1000 times as well, attributed to carrier trap associated with the grain boundary.

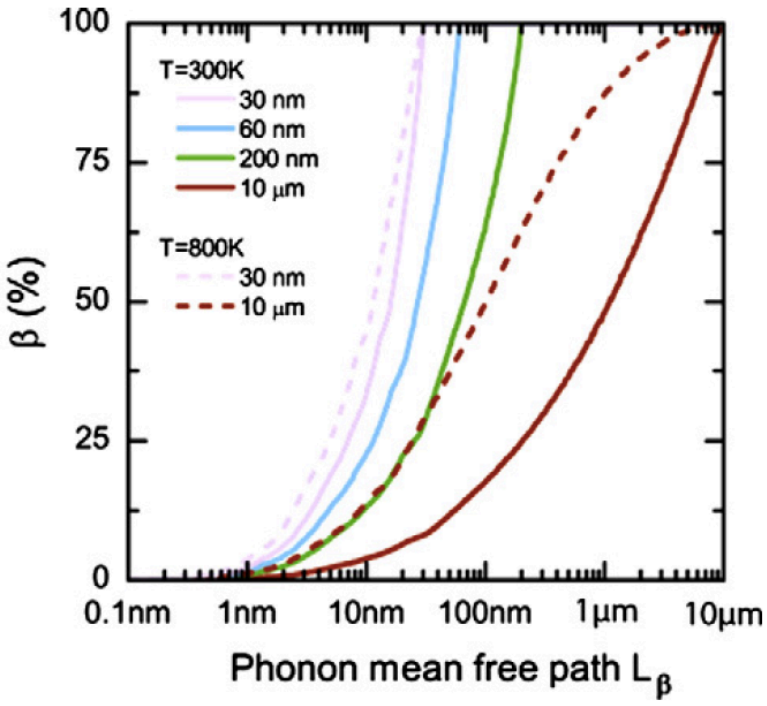

Figure 1.14 Calculations of the percentage, β, of heat carried by phonons with a mean free path shorter than L_β. β is calculated for grain sizes of 10 μm, 200 nm, 60 nm, 30 nm in ZnO at temperature of 300K and 800K[102].

Furthermore, porosity has been shown to reduce thermal conductivity in the study of Ga- and Al-doped ZnO in above discussion. Another way to generate pores is via the pore foaming technique. Using combustible nanosize polymer particles as a void forming agent (VFA), the nanosize voids introduced in a ZnO matrix (figure 1.15) was reported to reduce κ values by 16-25% [59]. However, milling with VFA also resulted in the dramatic deterioration of electrical property. The foaming technique[104] employing polystyrene was also used to introduce micro-pores in ZnO. Silicon carbide and aluminum nitride were utilized as micro-pores foaming precursors. The thermal conductivity displayed only a slight decrease with addition of both precursors, but the electrical conductivity declined

as well. Same degradation of electrical conductivity has been reported in porous SiGe and Si[105, 106]. Instead of conventional dense thermoelectric materials, the porous structure is an option to lower κ if its degradation on electrical conductivity can be avoided.

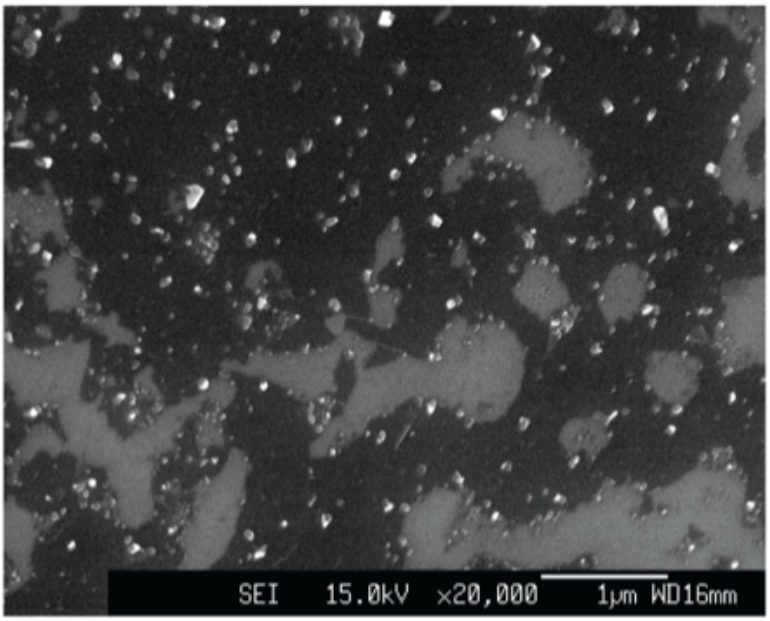

Figure 1.15 SEM image of a polished cross section of the sintered ZnAlO sample charged with 10wt% of 150nm VFA mixed using planetary mill for 45 s.[59]

1.2.4.2 Electrical properties

ZnO is naturally an *n*-type semiconductor because of a deviation from stoichiometry. The native defects in ZnO are complex, and in recent years most studies have identified Zn_i as the donor instead of V_O[6, 107, 108]. The *n*-type doping of ZnO is much easier to fabricate than the *p*-type doping so this study focuses on *n*-type bulk ZnO. According to equation 1.8, electrical conductivity is determined by carrier concentration and mobility. The experimental and theoretical results of the carrier concentration and mobility of pure

ZnO is shown in Figure 1.16. ZnO has relatively high carrier mobility among oxides but the carrier density needs be increased in order to higher electrical conductivity[6].

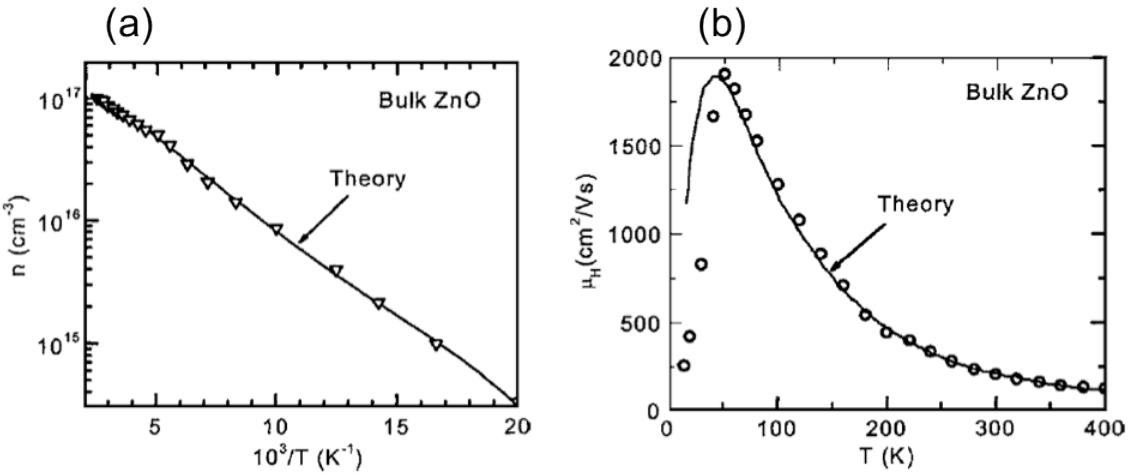

Figure 1.16 Experimental carrier concentration (triangles) and mobility (circles) and their theoretical fit (solid line) as a function of temperature for bulk ZnO[6].

The choice of doping elements, effective doping concentration and sintering conditions are able to modify chemical defects and affect electrical behavior. Aluminum is a common dopant for ZnO. Previous studies have revealed that the σ of Al_2O_3-modified ZnO can be increased by more than three orders of magnitude[5, 100]. This enhancement is due to Al^{3+} substitution on the Zn^{2+} site[109], which creates an extra electron for conduction. Nevertheless, doping depth is confined to the solubility of Al in ZnO, such as ~ 0.3 at. % at 1400°C[110]. The secondary phase $ZnAl_2O_4$ also has effect on the magnitude of electrical conductivity[109]. The $ZnAl_2O_4$ phase has a high electrical resistivity and could change the native defects concentration in a ZnO matrix. Further, a study has found that Al-doped ZnO sintered at 1100 ºC and 1400 ºC exhibited 50 times difference in electrical

conductivity[111]. This result confirms that sintering temperature also influences the electrical conductivity in ZnO. According to the phase diagram of Al_2O_3-ZnO (Figure 1.17), the reaction between ZnO and Al_2O_3 is distinct under varying temperature, which may change the function of Al in a ZnO matrix. Additionally, Berardan et al.[112] reported that Al-doped ZnO samples sintered in ambient nitrogen displayed larger electrical conductivity in comparison to those sintered in ambient air. The authors attributed this finding to oxygen vacancy formation. Given these diverse reports, a comprehensive study is essential for understanding the influence of temperature and atmosphere on the role of Al in the electrical conductivity of ZnO

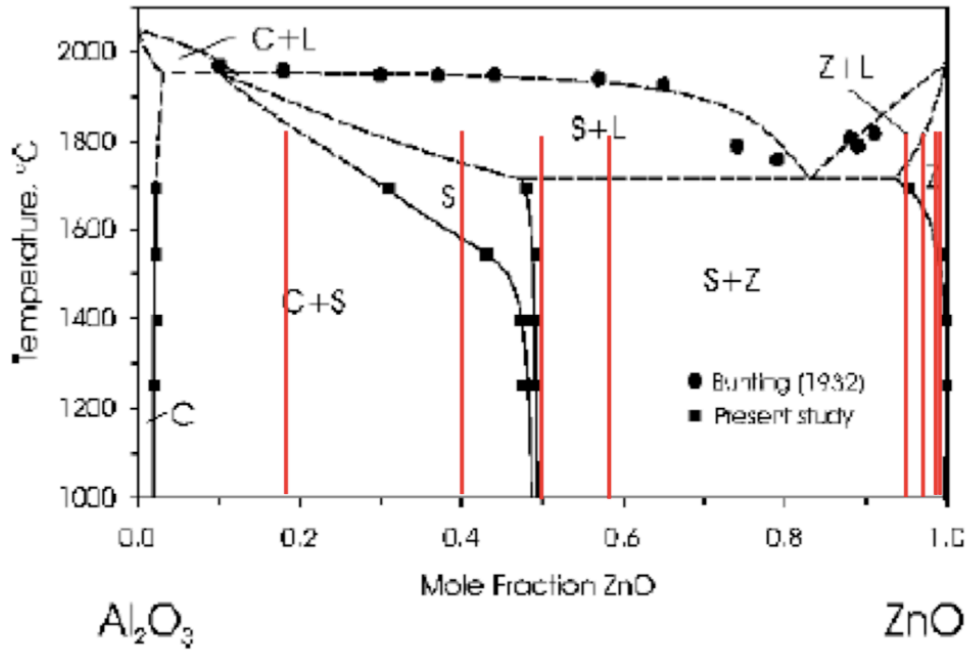

Figure 1.17 Phase diagram of Al_2O_3-ZnO

In addition to aluminum, other dopants used in ZnO have been explored. Kim et al. reported a slight increase in electrical conductivity by co-doping of Al and Ni[58]. Later Ohtaki et al.[55] reported a higher solubility of Al in ZnO through Ga co-doping; the researchers, however, were unable to document any improvements in electrical conductivity. With the introduction of pores via Ga doping (Figure 1.13a), a negative influence on carrier mobility was reported[55]. When only Ga_2O_3 was added to ZnO, the electrical conductivity of ZnO can be enhanced by over two orders[113]. Several other dopant, such as TiO_2 [114], WO_3 [115], Sb and Sn [116, 117] have been used to improve electrical properties of ZnO. In all these studies, electrical conductivity increased because of doping while Seebeck coefficient decreased.

1.2.4.3 Challenges

Compared with the best thermoelectric alloys, the main challenges for ZnO are its relatively high thermal conductivity and low electrical conductivity. Elements doping, nano grain size, and pores have been utilized in ZnO to lower the thermal conductivity—with the unwanted outcome of degrading its electrical conductivity in most cases. Moreover, it is still not clear that which of the above structures plays the dominant role in phonon scattering and how the structure size affects the thermal conduction behavior in ZnO. The κ of ZnO is still high compared with some good thermoelectric alloys. New structures for lower κ need to be explored.

Further, the electrical conductivity of ZnO is sensitive to sintering conditions, which reinforces the need for a comprehensive study investigating the influence of sintering conditions on electrical behavior. The nanostructure synthesis usually requires low

temperature, yet the sintering temperature influences the electrical behavior also. Thus, the dilemma for researchers is how to create a structure in ZnO for low thermal conductivity, while at the same time improving electrical properties.

1.3 Dissertation Objective

This research was designed with four objectives:

(1) Investigate the correlation between microstructure and thermal conductivity;

(2) Reduce the thermal conductivity of ZnO by synthesizing novel microstructures;

(3) Investigate the impact of Al doping and defects in ZnO under different synthesis conditions;

(4) Improve electrical conductivity and optimize the power factor by tuning synthesis parameters.

1.4 Dissertation Outline

The dissertation is organized into seven chapters:

Introduction and literature review in Chapter 1 provides the basic principles of thermoelectric effects, describe different kinds of thermoelectric materials, review the primary methods for improving their thermoelectric properties and the influence of microstructures on thermal conductivity. The methods for improving thermoelectric properties of ZnO are surveyed in detail.

Chapter 2 introduces the experimental methods and measurements used in this research. This chapter details characterization techniques and thermoelectric property testing

In Chapter 3, nano- and micron-scale precipitate structures together with various grain sizes are designed. The influence of these structures on phonon scattering and thermal conductivity in bulk ZnO is discussed.

In Chapter 4, a new layered-and-correlated grain structure embedded with nanoscale precipitates is achieved in bulk ZnO. The stripe shaped interspaces exhibit ordered orientation along the grain layers instead of random distribution, which is promising for low thermal conductivity. The mechanisms for formation of this layered-and-correlated grain structure are explored.

In Chapter 5, a systematic study on nature of Al doping and defect chemistry in ZnO under different sintering conditions (temperature, atmosphere, and initial physical conditions) has been conducted.

Chapter 6 discusses the thermal treatment and its influence of microstructure and thermoelectric properties of $Pb_{0.9}S_{0.1}Te$.

Finally, conclusions and future research plans are described in Chapter 7.

Chapter2 Experimental and Property Characterizations

2.1 Synthesis Techniques

ZnO powders were prepared using ball-milling and sol-gel chemical synthesis methods. The bulk ZnO was synthesized using powder compact at varying high temperatures and atmospheres (air, nitrogen, vacuum). High temperatures corresponding to 1100, 1200, 1300, 1400 °C were used for sintering. Relatively lower temperatures (800, 900, 1000 °C) were used to study the mechanism of grain growth. The tube furnace (Figure 2.1a) was utilized to control the gas flow during sintering and vacuum condition was achieved by sealing samples in vacuumed quartz tube. Figure 2.1b displays a group of $Zn_{1-x}Al_xO$ pellets sintered under air. The detailed synthesis processes and conditions are provided in each chapter.

The alloy samples were all synthesized in vacuumed quartz tubes in order to prevent them from oxidation. In the quartz tubes, mixed metallic powders were placed in a graphite crucible to avoid the reaction between sample and quartz. An induction furnace (Figure 2.1c) was used to achieve the quick heating and rapid cooling. A normal box furnace was used to anneal the alloys which were sealed in quartz tubes. Figure 2.1d shows a $Pb_{0.9}S_{0.1}Te$ alloy sample.

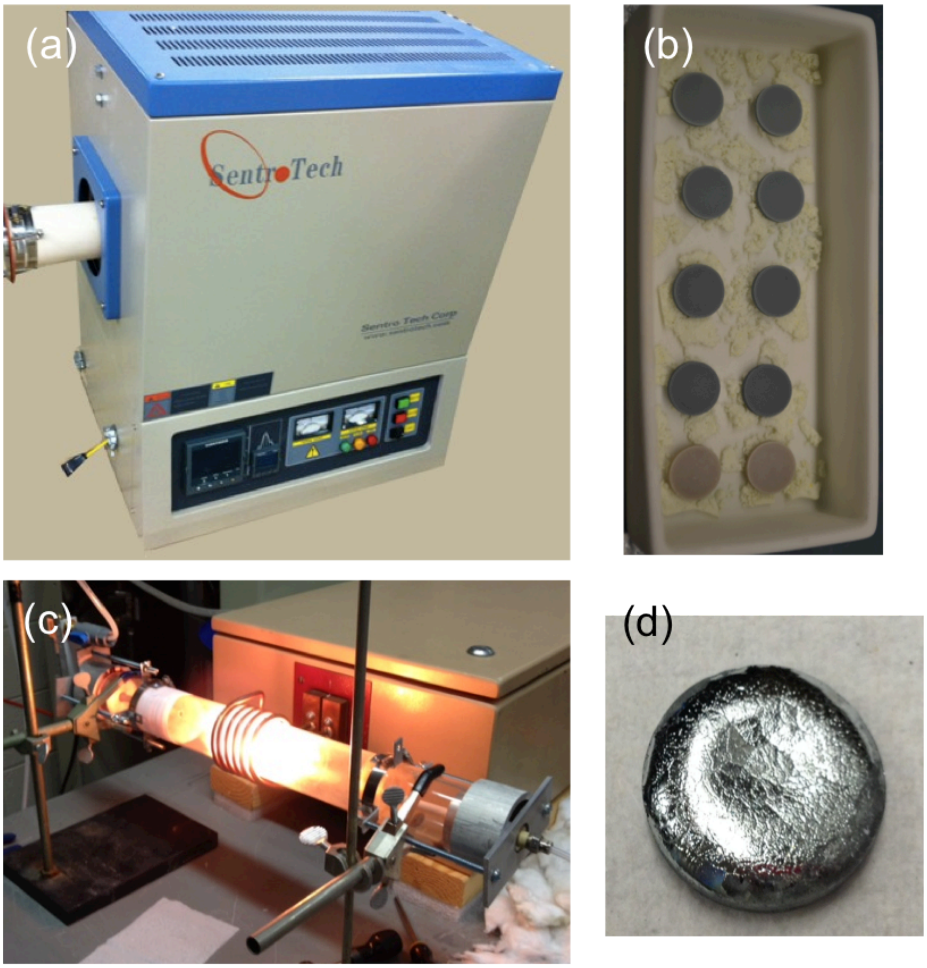

Figure 2.1 (a) Tube furnace for ZnO sintering under different atmospheres; (b) $Zn_{1-x}Al_xO$ ($0 \leq x \leq 0.04$) samples after sintering under air flow; (c) induction furnace for PbTe-based alloy melting which can heat up and cool down rapidly; (d) one $Pb_{0.9}S_{0.1}Te$ alloy after melting in induction furnace.

2.2 Materials Characterization

2.2.1 Powder X-ray diffraction (XRD)

X-ray diffraction (PANalytical X'Pert, Cu Kα; Philips, Almelo, the Netherlands) was used to investigate the phases of bulk samples and synthesized powders. The voltage and

current used were 45V and 30A. Scans were obtained typically from 25 to 80 degrees, 2 theta scan with a step size of 0.02 degrees.

2.2.2 Scanning Electron Microscope (SEM)

SEM (LEO (Zeiss) 1550 field-emission) was conducted to investigate the microstructure of powders and fresh surface of bulk samples. The energy of the beam used was 5kV. Gold was coated on ZnO samples by Cressington Sputter Coater before SEM analysis.

2.2.3 Energy Dispersive Spectrometer (EDS)

Oxford INCA Energy E2H X-ray energy dispersive spectrometer system with silicon-drifted detector was utilized for elemental scanning and mapping. The energy of the beam used was 20kV.

2.2.4 Particle Size Analyzer

Size distributions of sol-gel chemical synthesized and ball-milled ZnO powders were measured using Particle size analyzer (Horiba Partica LA-950 Laser Diffraction). The powders were put in water with several drops of dispersant and dispersed in ultrasonic machine for half an hour before measurement.

2.2.5 Transmission Electron Microscope (TEM)

TEM investigations were conducted on JEOL 2100, which is a state-of-the-art field thermionic emission analytical electron microscope. TEM samples were prepared by conventional polishing and dimpling in a water-free environment to around 30μm thickness. Then the samples were thinned to the electron transparent thickness by ion milling at liquid nitrogen temperature, which prevented samples from overheating.

2.2.6 Absorbance measurement

UV-Vis-NIR spectrophotometer (Hitachi U 4100) was used for absorbance measurement. The ZnO powders or crushed powders from bulk ZnO were held in a quartz sample container during scanning. The testing was carried in a dark environment.

2.2.7 Raman spectrum

Raman spectra were collected using 100 mW-514 nm argon laser integrated with JY Horiba LabRam HR800 (high resolution 800 mm focal length spectrometer) and Andor electronically cooled CCD detection system (1024x256).

2.2.8 Photoluminescence spectrometer

PL spectra were collected using luminescence spectrometer (Perkin-Elmer, LS50B, USA) equipped with a 200 W Xe lamp and red-sensitive photomultiplier tube (Hamamatsu, R928, Japan).

2.3 Thermoelectric Measurements

2.3.1 Electrical property measurements

Seebeck coefficient was determined by voltage difference per temperature difference (equation 1.6). The measurements were done by the system shown in Figure 2.2 in an argon environment.

The electrical conductivity was measured by the Van der Pauw method on two systems. One used Stanford Research Systems SR830 Lock in Amplifier and Keithley 2000 Multimeter. Tungsten probes were used to touch four points at the perimeter of samples. The R measurements were done using A/C with a lock-in amplifier, so DC offsets from

thermoelectric effects are not present. Another system (shown in Figure 2.2) used an Agilent 34970A switch; with a Keithley 6220 current source that supplied precise currents for the electrical resistivity measurements; and with a Keithley 2182A nano-voltmeter that allowed for extremely sensitive voltage measurements. The sample dimension requires much larger diameter in plane than thickness.

Samples with high resistivity were tested by voltage-current method using Precision Premier II tester (Radiant Technologies). Impedance measurements were performed using Versa STAT 3 analyzer as a function of frequency (0.1Hz to 1MHz).

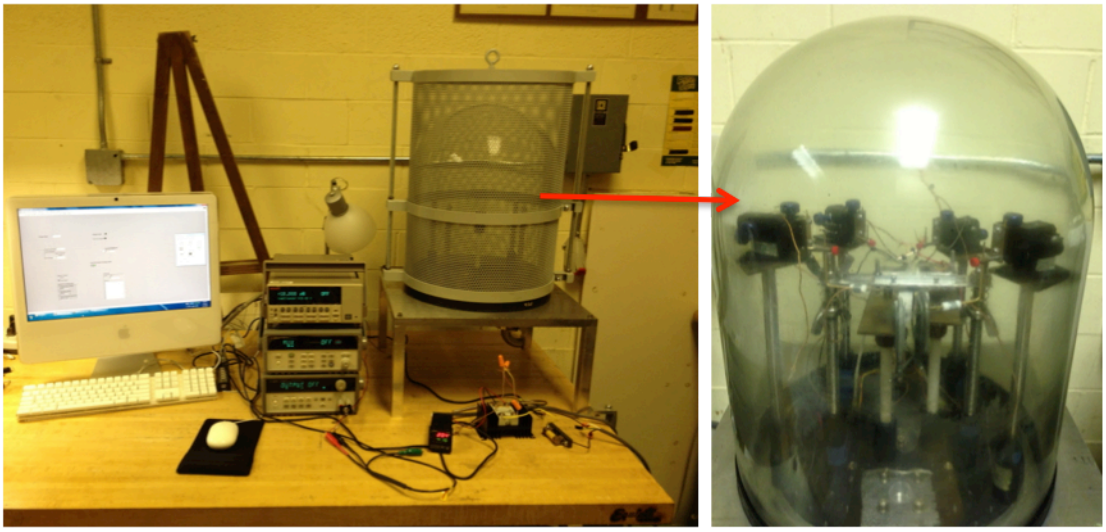

Figure 2.2 Thermoelectric property measurement system. To the left of the bell are an Agilent 34970A switch, a Keithley 6220 current source, and a Keithley 2182A nano-voltmeter.

2.3.2 Hall Effect measurement

Hall measurements were carried out in the Van der Pauw geometry, shown in Figure 2.3 left. Carrier density can be calculated by following relationship:

$$V_H = \frac{BI}{nqt} \tag{2.1}$$

where V_H is Hall voltage, B is magnetic field, I is the current across the plate length, and t is sample thickness. The sample dimension is about 10×10×1mm. Indium electrodes were made in each corner of sample plane (shown in Figure 2.4 right) and anneal at 300 °C for 10 min under nitrogen flow.

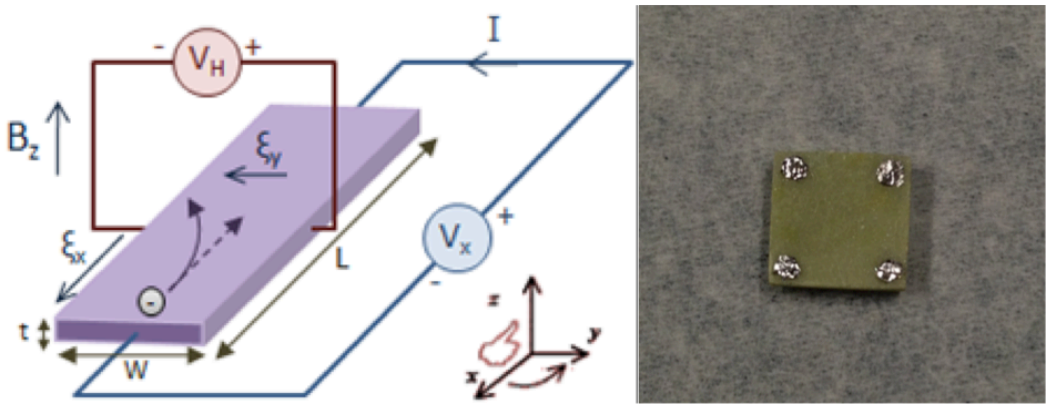

Figure 2.3 Hall Effect measurement setup for electrons on the left and one ZnO sample with Indium electrodes for measurement on the right.

2.3.3 Thermal conductivity measurement

Thermal conductivity κ was determined by combining thermal diffusivity α and heat capacity c_p of samples ($\kappa = \alpha\rho c_p$, ρ is the density). The thermal diffusivity of a material determines the speed of heat propagation by conduction during changes of temperature with time. A common method for measuring α is flash method, which has advantage of fast speed and excellent accuracy. α is extracted from its relationship with sample

thickness (d) and the time required to reach half of the maximum temperature increase ($t_{0.5}$): α=0.1388 d^2 / $t_{0.5}$. For samples in Chapter 3, α was measured using TA Instruments FL5000 flash diffusivity system and c_p measured using Netzsch 404 DSC. The sample dimension is 12.7 mm diameter and around 1 mm thickness. For samples in Chapter 4 and Chapter 6, the thermal diffusivity measurement was carried out using Xenon flash technique in a custom measurement system (Xenon Flash Bulb System, EG&G Electro-optics Model LS-187). The sample dimension is 10 mm diameter and around 1 mm thickness. The density is determined by Archimedes' method.

The electronic contribution to total thermal conductivity κ_{elec} was calculated using the Wiedemann-Franz law, $\kappa_{elec} = \sigma T$L, where σ is electrical conductivity, T is temperature, and L is 2.45×10^8 WΩK^2 as degenerate semiconductors. The lattice component κ_{latt} was then calculated using the relation $\kappa_{latt} = \kappa - \kappa_{elec}$.

Chapter3 Precipitate Structure and Grain Boundary on Thermal Conductivity of Bulk ZnO

In this chapter, the thermal conduction behavior of ZnO-Al bulk with precipitates structures (micro- or nano-scale: micro-composites or nano-composites) and varying ZnO grain sizes is discussed. The reduction in thermal conductivity of micro-composites is about 15% for ZnO-4% Al, however, nano-composites exhibit a large κ reduction, about 73% at room temperature. Raman spectra indicate that phonon confinement in nano-precipitates ($ZnAl_2O_4$) causes the drastic decrease in the value of thermal conductivity. ZnO grain size also has a contribution towards the thermal conductivity.

3.1 Synthesis and Phase Analysis of ZnO with Precipitates

Two sets of $Zn_{1-x}Al_xO$ ($0 \leq x \leq 0.04$) samples were synthesized using solid-state reaction method. For the first set of samples, micron size precursor powders, ZnO (~75 μm, purity>99.9%) and Al_2O_3 (~60 μm, purity>99.9%) were used. These samples were sintered at 1400°C for 5 h in air to obtain micron size precipitates, referred to as ZnO-Al micro-composites. The second set of samples were synthesized using nanosize precursor powders, ZnO (~30 nanometer, purity >99.7%) and Al_2O_3 (40-50 nanometer, purity>99.5%), and sintered at 1100 °C for 5 h in air to obtain ZnO with nanosize precipitated phase, referred to as ZnO-Al nano-composites.

X-ray diffraction patterns of these two sets of $Zn_{1-x}Al_xO$ bulk pellets are shown in Figure 3.1a and b. All samples reveal hexagonal wurtzite type zinc oxide phase formation (JCPDS # 36-1451). It is evident that ionic radius of Al^{3+} (0.39 Å) in four-fold coordination is smaller than Zn^{2+} (0.60 Å) and therefore, if Al^{3+} occupies Zn^{2+} sites, a

decrease in lattice parameter should be noticed [118]. An increase in Zn vacancies may also lead to the smaller values of lattice parameters *a* and *c*. The samples synthesized using micron-size powders exhibit lattice parameters *a* and *c* as 3.245(9) and 5.201(4) Å for x = 0.0. Incorporation of Al in the ZnO lattice should lead to shrinkage and subsequently lowering of *a* and *c* values; while *a* and *c* values [3.243(0) and 5.199(3) Å respectively for Al content x = 0.02] were almost the same as for pure ZnO. This result indicates that very few Al atoms occupy Zn^{2+} sites. XRD patterns of the samples obtained using nanosize precursor powders exhibit lattice parameters as *a* = 3.247(5) and *c* = 5.203(5) Å at x = 0. The nanostructured samples also show no obvious decrease in lattice parameter with increasing Al content. Typical values of *a* and *c* being [3.248(9) Å, 3.247(5) Å, 3.246 (5) Å] and [5.202(0) Å, 5.201(2) Å, 5.200(2) Å] for Al content x = 0.01, 0.02 and 0.03, respectively. Further, on examining the XRD patterns carefully, a signature of gahnite phase, $ZnAl_2O_4$, (JCPDS # 5-0669) can be noticed in all the $Zn_{1-x}Al_xO$ samples with Al content $x > 0.01$, which is shown in zoomed-in vision of XRD data and marked with arrow in Figure 3.1. It's possible that only a few Al atoms stay in the ZnO matrix and most in the $ZnAl_2O_4$ second phase.

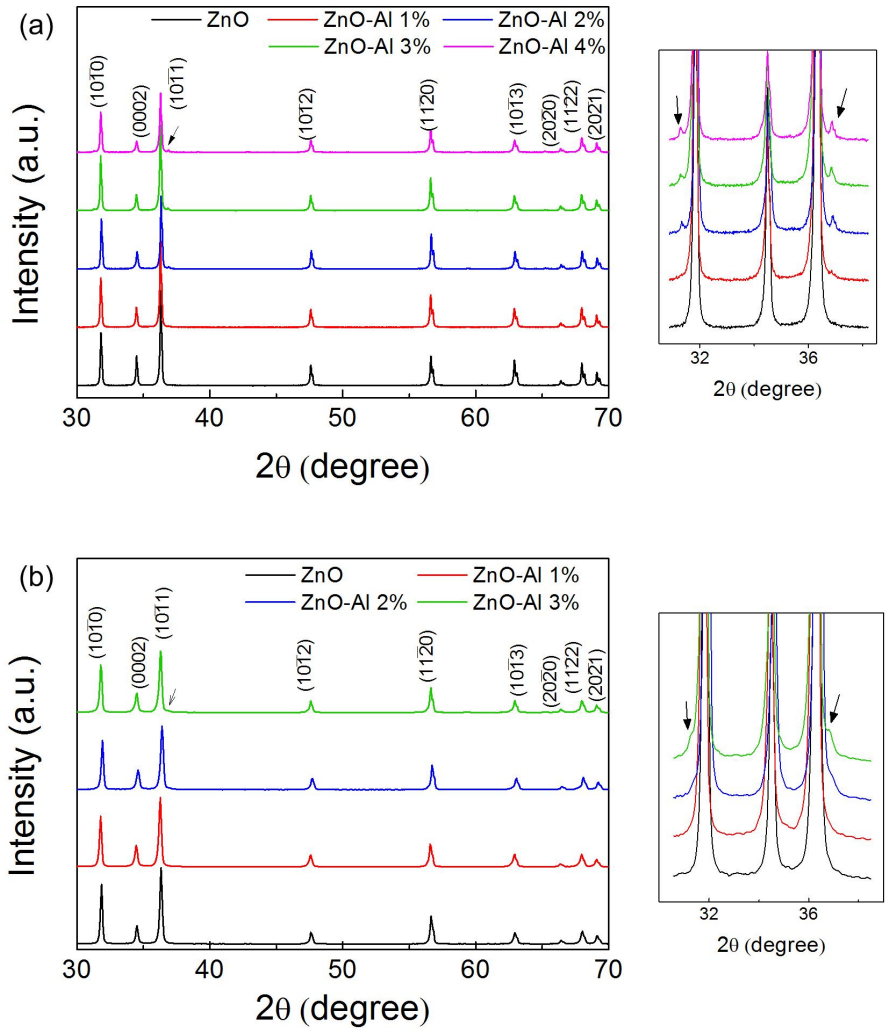

Figure 3.1 XRD patterns of ZnO-Al (a) micro-composites; (b) nano-composites.

Figure 3.2 shows the scanning electron micrographs of two series of sintered $Zn_{1-x}Al_xO$ pellets. $ZnAl_2O_4$ precipitates can be observed in all Al-doped ZnO samples. Increase in Al concentration increases the fraction of gahnite precipitates and inhibits grain growth in both series of samples. Typical size of micron-size precipitates is 1-4 μm for the ZnO-Al micro-composites. Elemental mapping performed using EDS on a typical $Zn_{0.96}Al_{0.04}O$ sample confirms that $ZnAl_2O_4$ phase distributes uniformly both inside and at grain

boundaries of ZnO grains (Figure 3.2f). The ZnO grain size has some decrease with increase in Al content, from around 30 μm to around 20 μm. According to the microstructure images, ZnO-Al micro-composites are dense and the density estimated using Archimedes' method for ZnO-Al micro-composites containing 0, 1, 2, 3 and 4% Al was found to be more than 95%.

Figure 3.2g-j shows the SEM micrographs of the $Zn_{1-x}Al_xO$ ($0 \leq x \leq 0.03$) samples synthesized using nanosize precursor powders. The grain size is much smaller in comparison to the ZnO-Al micro-composites samples. Further, the grain size is drastically reduced with Al incorporation, from 15 μm to around 2 μm. The typical values of $ZnAl_2O_4$ precipitates are 50 to 400 nm. The density estimated using Archimedes' method for ZnO-Al nano-composites containing 0, 1, 2 and 3% Al was found to be ~95% of relative density. The porosity of these two sets of samples can be considered similar and doesn't have large effect on thermal conduction property.

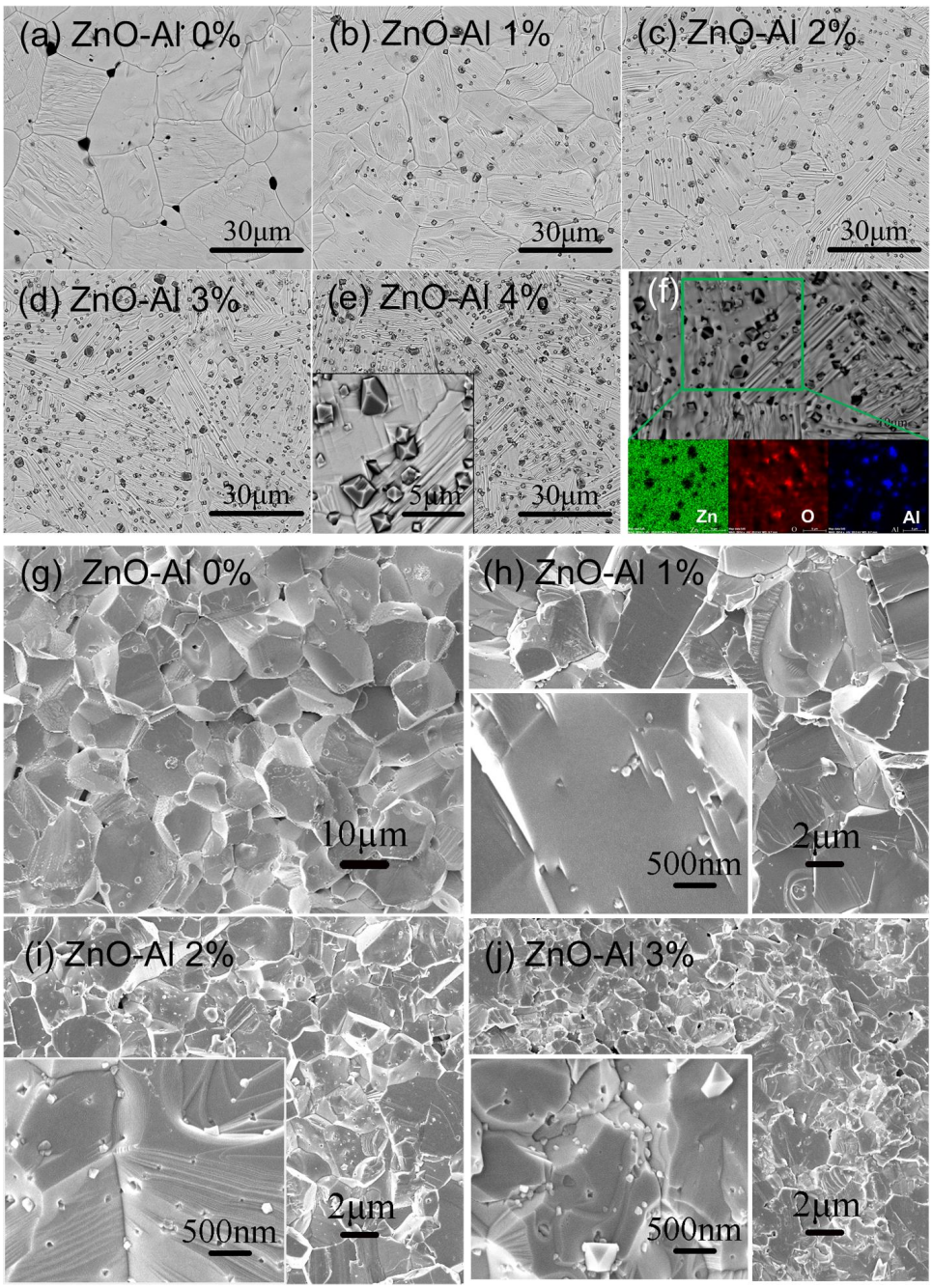

Figure 3.2 (a)-(e) Contrast SEM micrographs using backscattered electron of $Zn_{1-x}Al_xO$ ($0 \leq x \leq 0.04$) micro-composites; The darker particles are $ZnAl_2O_4$ precipitates; (f) EDS elemental mapping of $(Zn_{0.96}Al_{0.04})O$ sample on element Zn, O and Al; (g)-(j) SEM micrographs of $Zn_{1-x}Al_xO$ ($0 \leq x \leq 0.03$) nano-composites; The inserts are higher magnification and the brighter particles are $ZnAl_2O_4$ precipitates.

3.2 The Effect of Precipitates Size on Thermal Conductivity

The thermal conductivity (κ) of both series of samples are shown in Figure 3.3. Thermal diffusivity was measured by the thermal flash technique and the thermal conductivity was calculated from the following relation:

$$\kappa = \rho \alpha c_p \tag{3.1}$$

where ρ is the material density, α is the thermal diffusivity, and c_p is the heat capacity. Both series of samples exhibit reduction in the values of κ with increasing temperature as a result of thermal softening and higher frequency phonon interactions at elevated temperatures[119]. However with increasing Al content, micro- and nano- composites display different κ behavior. ZnO-Al micro-composites exhibit a decrease in the κ with increase in Al content, relative decrease in value of κ being ~15% for the samples containing 4% Al over the whole temperature range. For ZnO-Al nano-composites, the reduction is much more obvious, especially in low temperature range. The value of κ drops to its minimum for the samples containing 2% Al and then increases again for 3% Al addition. The thermal conductivity of ZnO-2%Al is 7.5 W/m.K at room temperature and then decreases to 3.7 W/m.K at 600°C. These values are 73% and 40% lower than pure ZnO bulk synthesized under the same conditions.

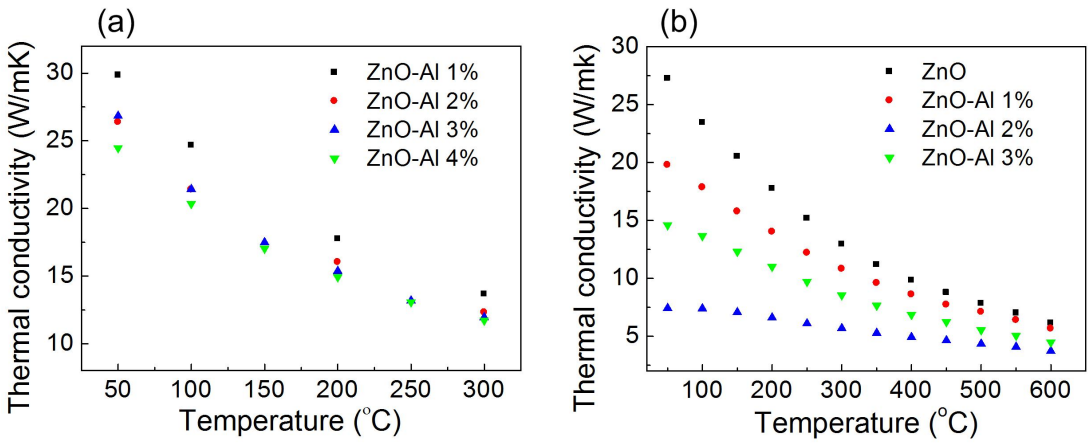

Figure 3.3 Temperature dependence of thermal conductivities of ZnO-Al (a): micro-composites; (b): nano-composites.

Since more than 90% of thermal conductivity is associated with κ_{latt} for conventional ZnO, the major contribution should come from phonon scattering [100]. It is well known that the contribution of phonon-phonon and phonon-electron scatterings is low below the Debye temperature (~ 400 K for ZnO)[6]. The phonon-boundary and phonon impurity scatterings play a dominant role at relative low temperature (below 400 K) to achieve obvious thermal conductivity reduction in low temperature range for both groups. According to the observations from SEM and XRD, both series of ZnO-Al composites possess two main differences from pure ZnO: namely presence of precipitates and grain size decrease. Low porosity in both groups is assumed to have similar phonon scattering effect. Both the $ZnAl_2O_4$/ZnO and ZnO/ZnO boundaries will act as the potential sites for phonon scattering. Moreover, the dimension of precipitates and grain size of ZnO-Al nano-composites are much smaller than those of ZnO-Al micro-composites, according to

Figure 3.2. The phonon-boundary scatterings on nano-precipitates may be the important factor to achieve great thermal conductivity reduction in ZnO-Al nano-composites.

For understanding the mechanism of phonon scattering in nano-composites, Raman spectroscopy was utilized. The vibration properties of the nano-composite ZnO-Al samples investigated using laser Raman spectra are shown in Figure 3.4. The wurtzite ZnO belongs to the C_{6v}^4 space group with four atoms per unit cell. From the 12 possible vibration modes only the A_1, E_1, and E_2 are Raman-active optical modes. Further, due to ionic character of Zn–O bonds, polar modes (A_1 and E_1) exhibit large splitting as longitudinal optical (LO) and transverse optical (TO) modes[6]. The appearance of a high intensity, sharp and strong peak around 440 cm^{-1} is attributed to the Raman active optical phonon E_2 mode of the ZnO. It is obvious that the mode 'E_1-high' is much stronger in the ZnO-Al samples in comparison to ZnO without Al. Theoretical reports on phonon confinement in ZnO nanostructure have predicted confined LO phonon wave number to be between A_1 (LO) (574 cm^{-1}) and E_1 (LO) (590 cm^{-1})[119]. Experimental studies have found confined LO phonon modes to appear at 588 cm^{-1} (for 8.5 nm) and 584 cm^{-1} (for 4.0 nm)[120, 121]. We believe the higher intensity at 584.5cm^{-1} is attributed to nanosize secodary phase in ZnO-Al nano-composites. No significant peak shift is observed for any of the phonon modes (inset Figure 3.4). It has been reported that peak shift and broadening of the Raman peaks is observed when quantum dot size approaches to exciton Bohr radius[122, 123]. It is believed that the size of the precipitated phase in ZnO-Al nano-composites is effective for phonon confinement but not small enough to exhibit peak shift and broadening. Therefore, phonon scattering at ZnO/$ZnAl_2O_4$ boundary occurs in both

ZnO-Al micro- and nano-composites, and phonon confinement happens in the homogeneously distributed nano-precipitates and leads to a larger decrease in κ.

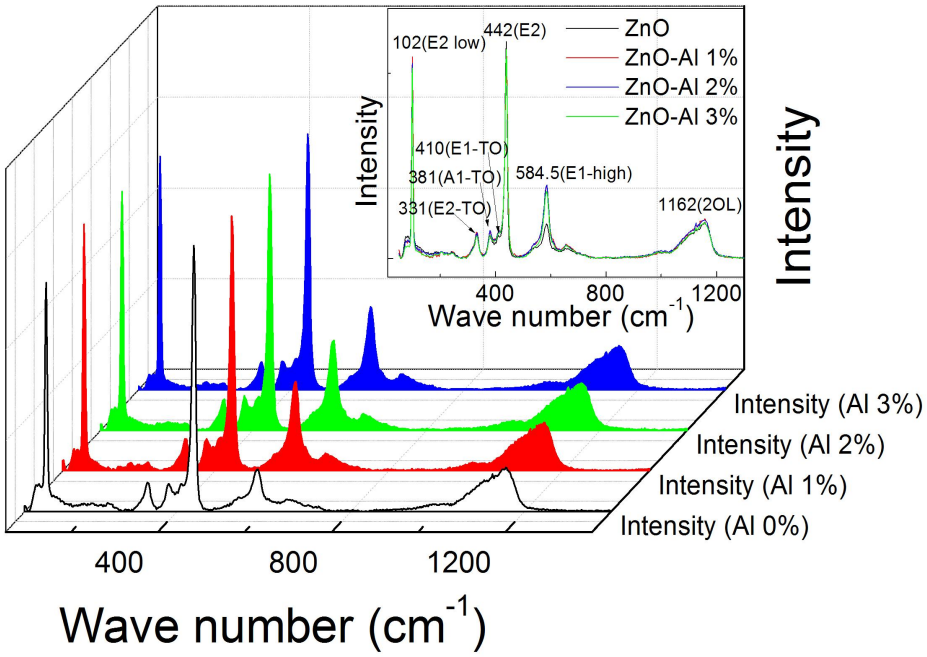

Figure 3.4 Raman spectra of ZnO-Al nano-composites.

Furthermore, κ reduction of ZnO-Al nano-composites varies with the amount of Al. κ drops significantly from pure ZnO to ZnO containing 2% Al and then increases again for 3% Al addition, which indicates the difference of phonon relaxation time. Phonon scattering behavior generally depends on four mechanisms: Umklapp phonon-phonon scattering, phonon-impurity scattering, phonon-boundary scattering, and phonon-electron scattering. So the combined relaxation time can be given as[124]:

$$\frac{1}{\tau_C} = \frac{1}{\tau_U} + \frac{1}{\tau_M} + \frac{1}{\tau_B} + \frac{1}{\tau_{ph-e}} \tag{3.2}$$

where τ_C, τ_U, τ_M, τ_B and $\tau_{ph\text{-}e}$ denote total, Umklapp phonon-phonon scattering, phonon-impurity scattering, phonon-boundary scattering, and phonon-electron scattering relaxation times, respectively. The amount of Al replacing Zn atoms is small (Figure 1.17), because of low Al_2O_3 solubility in ZnO (< 0.3 %)[110]. Since most Al^{3+} ions stay in precipitates, the Umklapp phonon-phonon scattering, phonon-impurity scattering, and phonon-electron scattering in ZnO-Al nano-composites can be considered to be comparable, so not the reason for large κ difference. Because of the formation of nano-precipitates and grain size reduction, phonon-boundary scattering is the key factor for κ variation. The relaxation time can be expressed as[124]:

$$\frac{1}{\tau_B} = \frac{V}{D}(1-p) \tag{3.3}$$

where V is phonon group velocity, D is the dimension of the system, and p is surface roughness. The value of p that is close to 1 means a smooth surface, where the scattering is purely specular and the relaxation time goes to ∞; hence, perfect smooth boundary scattering does not affect thermal transport. The different lattice arrangement at $ZnO/ZnAl_2O_4$ boundary makes p a value less than 1. With increase of Al additive to 2%, the amount of precipitates increases resulting in reduction of κ especially at low temperature range. When Al concentration rises up to 3%, the size of some of the precipitates enlarges to 300-400 nm, resulting an increase in relaxation time and magnitude of κ.

3.3 The Influence of Grain Boundary on Thermal Conductivity

ZnO/ZnO grain boundary is another phonon-boundary scattering center. ZnO grains shrink from ~15 μm for pure ZnO to about 2 μm in ZnO-Al nano-composites (x = 0.03). The grain size in ZnO-Al micro-composites also has a slight decrease with increase in Al content, from around 30 μm to 20 μm. ZnO samples with various grain sizes were synthesized to understand the contribution arising from ZnO/ZnO grain boundary on phonon scattering.

Pure ZnO samples were synthesized using ZnO (~30 nm, purity >99.7%) powders. These samples were sintered subsequently by one-step sintering (1100 °C, 1000 °C and 950 °C for 5 h) and two-step sintering (first heating up to 1000 °C holding for 1 min, cooling to 825 °C holding for 5 h with the rate of 4 °C per min and 20 °C per min, respectively) to achieve different grain sizes. The ZnO samples with grain sizes varied from 1 μm to about 15 μm depending on whether one-step sintering or two-step sintering at different heating rate were synthesized (Figure 3.5a). All the sintered samples have relative density higher than 96%; therefore the porosity is not an effective factor on thermal conductivity here. The ZnO with different grain size exhibit pure hexagonal wurtzite structure, shown in Figure 3.5b.

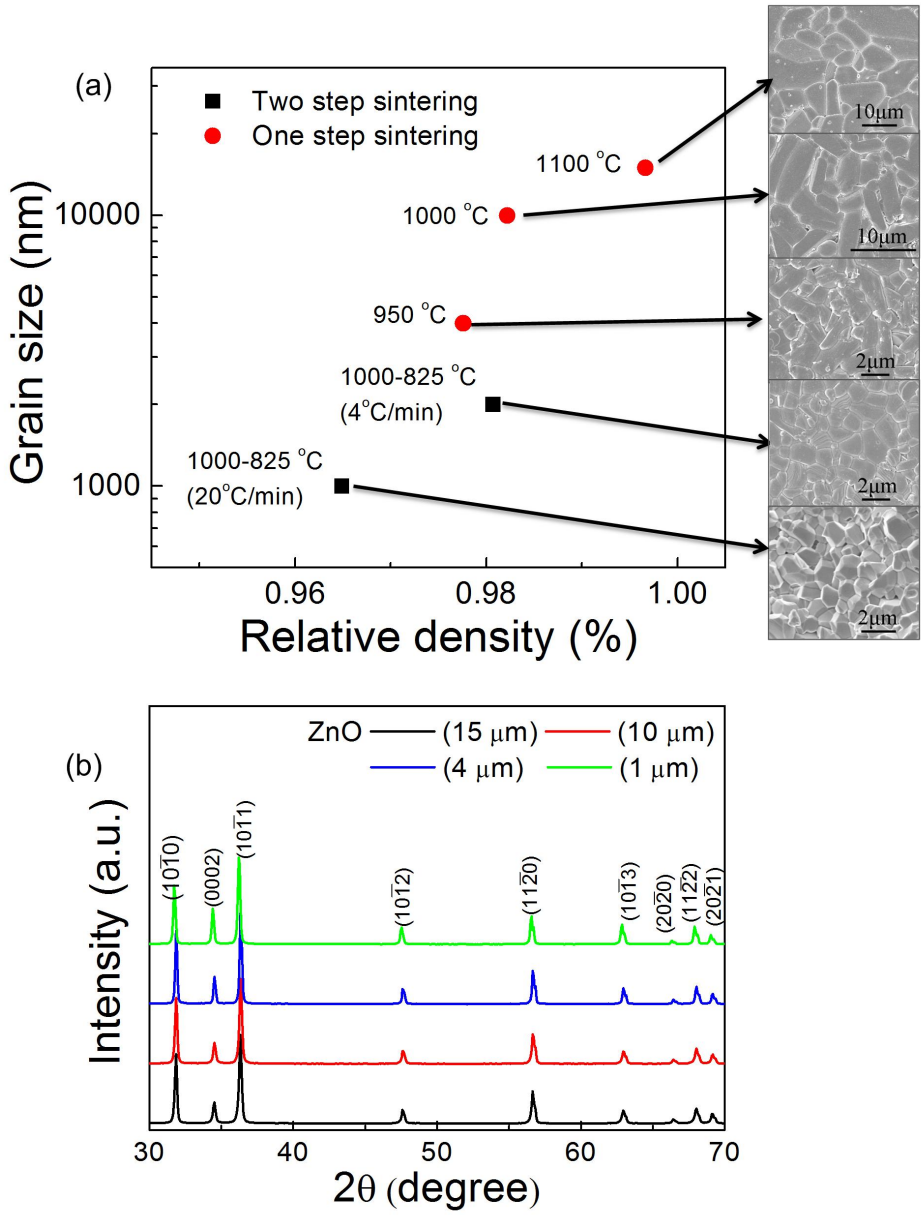

Figure 3.5 (a) Grain size vs. relative density and SEM micrographs of ZnO with different grain size; (b) XRD of ZnO with different grain size.

The thermal conductivity of dense ZnO with different grain size is shown in Figure 3.6. It can be observed that κ reduction with smaller grain size is more evident at relative low temperatures. According to previous discussion (equation 3.3), this phenomenon is result

from phonon-boundary scattering. The κ values at room temperature for ZnO samples with grain sizes of 10 μm, 4 μm, 2 μm and 1 μm are reduced by 10%, 13%, 25% and 28% respectively, compared with the large grain size (15 μm). At elevated temperatures (600 °C), ZnO samples with grain sizes 15 μm, 10 μm, and 4 μm have almost the same κ (the difference is less than 5%). While smaller grains such as 2 μm and 1 μm reveal reduction in κ by ~13% and 18% respectively, compared with largest grain sizes 15 μm. These findings prove that grain size also has contribution towards the reduction in thermal conductivity but smaller than the contribution from nano-precipitates.

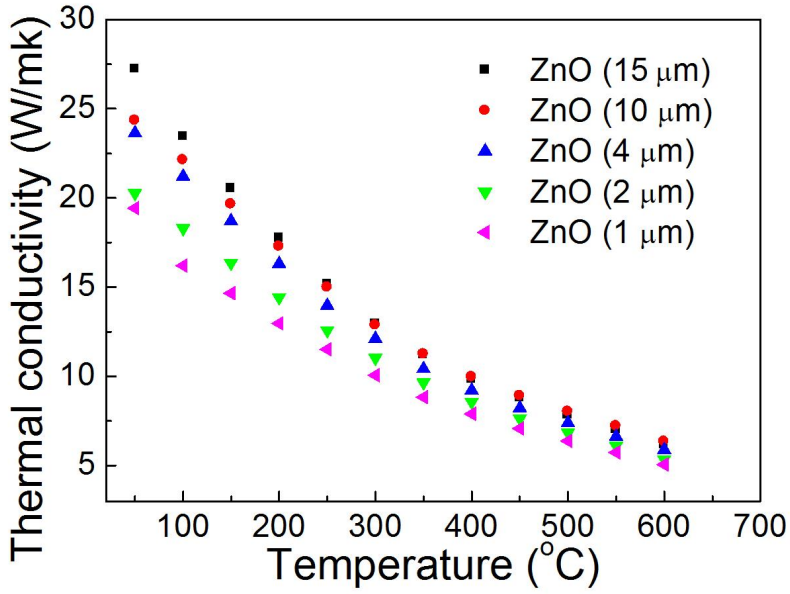

Figure 3.6 Temperature dependence of thermal conductivity of ZnO with different grain size.

3.4 Summary

In summary, Al-modified ZnO samples were synthesized using micron- and nanosize precursor powders through solid-state reaction. Incorporation of aluminum in ZnO leads to the precipitation of secondary phase $ZnAl_2O_4$, which in turn inhibits grain growth. The ZnO-Al micro-composites reveal a continuous decrease in thermal conductivity with increase in Al addition, while the ZnO-Al nano-composites exhibit the lowest magnitudes for 2%Al concentration, which is much lower than that in the micro-composites. At 2 at% Al content, nano-composites exhibit the 3-fold reduction in the values of thermal conductivity. The reduction in thermal conductivity for micro-composites is limited (~15% for ZnO-4% Al). The large κ reduction of nano-composites is mainly attributed to phonon confinement in nanosize precipitates. The investigations on pure ZnO with varying grain sizes (~1 – 15 μm) demonstrate that ZnO grain size also has significant contribution towards the thermal conductivity reduction.

Chapter4 Layered and Correlated Grain Structure in Al-doped ZnO and its Thermoelectric Performance

In this chapter, the bulk Al-doped ZnO with a novel layered and correlated grain structure is found to exhibit sharp reduction in thermal conductivity. The microstructure consists of two-dimensional layered network of oriented grains, which interconnect in third dimension through inter-planar contact, and grains are embedded with nano-precipitates. The contact represents anisotropic connectivity of voids trapped between the grain layers. The effects of the synthesis atmosphere, Al doping concentration, and uniaxial compaction upon the formation of layered and correlated grains are explained. Compared with dense ZnO, Al-doped ZnO with layered microstructure exhibits a 52% decrease in the thermal conductivity across layers while maintaining the high magnitude of electrical conductivity.

4.1 Formation of Layered-and-correlated-grain ZnO

The powders for bulk ZnO sample were synthesized by chemical reaction as steps in Figure 4.1. The powders were synthesized using zinc nitrate hydrate [$Zn(NO_3)_2 \cdot 6H_2O$] and aluminum nitrate hydrate [$Al(NO_3)_3 \cdot 9H_2O$] (1- 3 at%) with oxalic acid [$(COOH)_2 \cdot 2H_2O$] as a precursor and ethanol as a solvent. The mixture, viscous white gel, was stored for 24 hours for uniformity and then dried at 80°C for 12 hours. All the dry gel products were subsequently calcined at 600°C for 2 hours with 10°C/min heating and cooling rate under nitrogen flow.

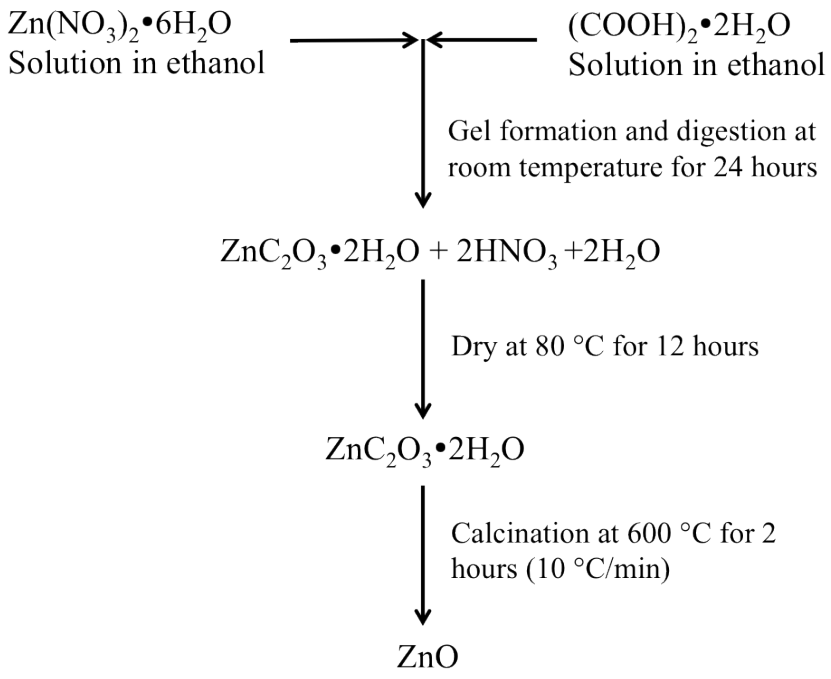

Figure 4.1 The steps involved in sol-gel synthesis for ZnO powders[125].

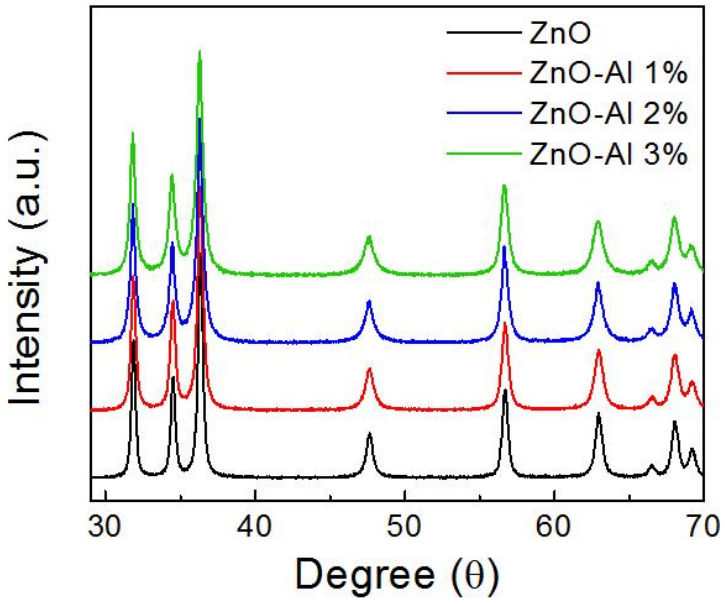

Figure 4.2 XRD patterns of synthesized ZnO- *x*%Al (*x*=0, 1, 2, 3) particles.

XRD results from chemical synthesized Al-doped ZnO powders are shown in Figure 4.2. All the synthesized powders exhibit only hexagonal wurtzite-type ZnO phase, indicating that Al element stays in the lattice of ZnO particle. The morphology of as-synthesized Al-doped ZnO powders is shown in Figure 4.3a-c. All Al-doped ZnO powders show sphere shape, which is distinct from that of un-doped ZnO powders, which is long bar shape with dimensions on the order of micro meter scale (Figure 4.3d). The powder size distribution was measured using Particle size analyser and listed in Figure 4.4. The particle sizes of the Al-doped ZnO powders are all in the narrow range of 82-92 nm that is much smaller than ZnO powders. It indicates that Al doping impedes the particle grow during synthesis.

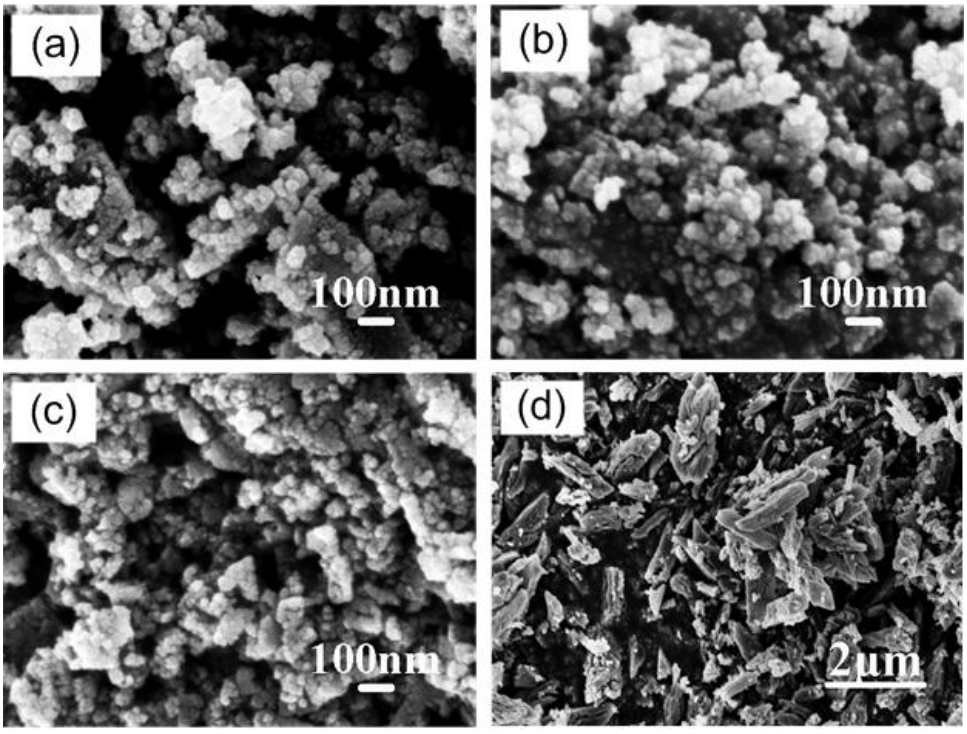

Figure 4.3 SEM micrographs of ZnO particles synthesized by sol-gel process (a) ZnO-1%Al, (b) ZnO-2%Al, (c) ZnO-3%Al; and (d) pure ZnO

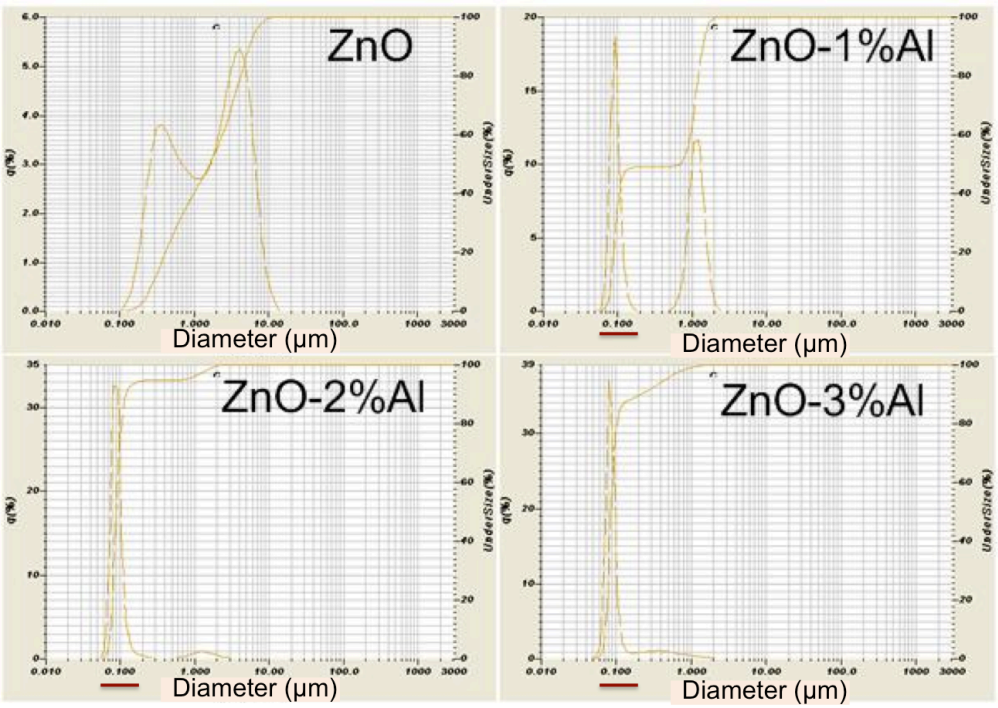

Figure 4.4 Particle distribution from synthesized ZnO- *x*% Al particles.

All bulk samples were sintered using $Zn_{1-x}OAl_x$ (x=0.01, 0.02, 0.03) nanopowders. Al-doped ZnO powders were pelletized using uniaxial press into pellets with about 15 mm diameter and 1.5 mm thickness. Pellets were sintered at 1200 °C for 5 h in sealed quartz tubes under the following vacuum conditions: 10^{-1}, 10^{-2}, 10^{-3}, and 10^{-5} Torr. For studying microstructure formation, pellets were also sintered at relative low temperatures 800-1100 °C, under vacuum (10^{-5} Torr), air and nitrogen.

Bulk ZnO-Al samples (1200 °C 5 hours, under 10^{-5} Torr condition) exhibit varying porous structures consisting of 5-10 μm grains interspersed by nano-precipitates, as shown in Figure 4.5a-c. The Al concentration coupled with vacuum condition is essential ingredient in the formation of the layered microstructure. The

ZnO-1%Al (Figure 4.5a) has higher density in comparison to the samples with higher Al doping, and the ZnO grains exhibit random orientation. The ZnO-2%Al ceramic shows a self-formed correlated grain structure arranged in layers (Figure 4.5b). The ZnO-3%Al ceramics also exhibit a layered and correlated grain structure with large amount of nano-precipitates on grain surface. In 2% and 3% Al-doped samples, the cross-sectional long interspaces are found to distribute themselves parallel to the sample surface.

XRD spectra (Figure 4.5d) from bulk ZnO-*x*%Al (*x*=1, 2, 3) demonstrate the formation of a hexagonal wurtzite type ZnO phase. A small fraction of the gahnite phase $ZnAl_2O_4$, referred to as second phase precipitates[55, 56, 58] can be detected when Al amount is 2% and 3%. As seen in zoomed-in XRD spectrum in Figure 2d, when the Al doping increases so does the intensity of XRD peaks from the gahnite phase. This change indicates that with the increase of Al doping amount more $ZnAl_2O_4$ precipitates have formed. There are few $ZnAl_2O_4$ precipitates in ZnO-1%Al. The amount of second phase precipitates is consistent with the SEM images. EDS analysis for typical ZnO-3%Al (10^{-5} Torr) confirms that the Al concentration in precipitates is higher than that in the ZnO grain (Figure 4.5e).

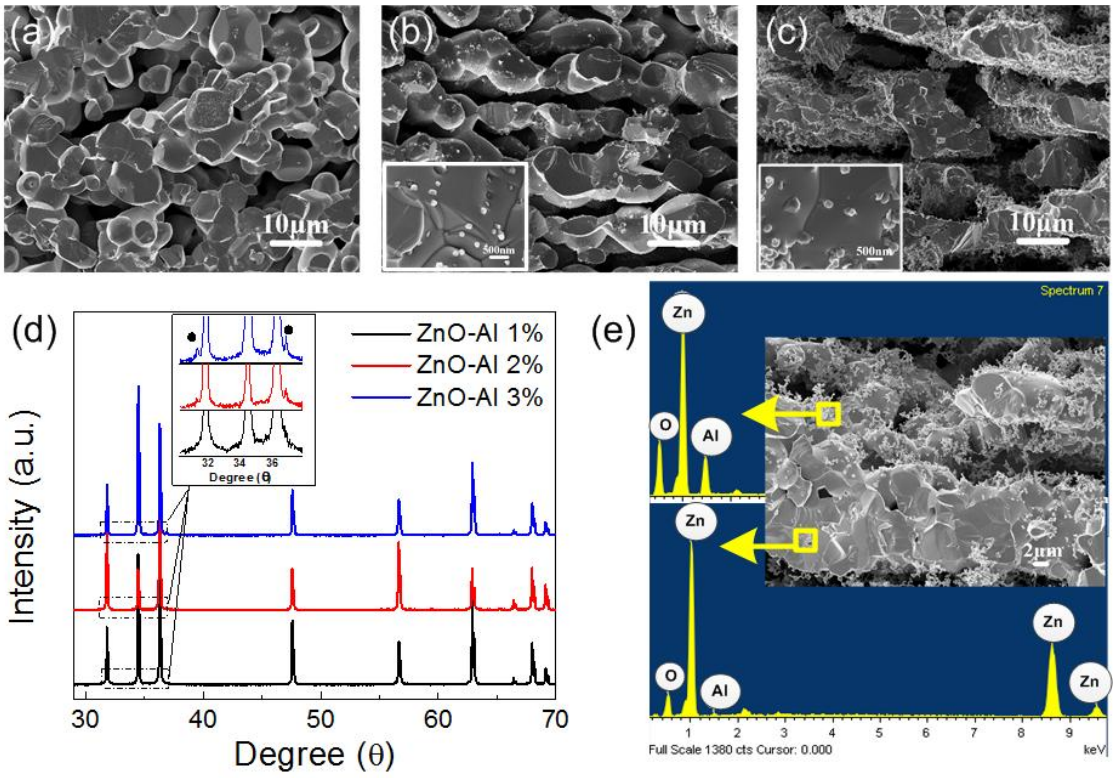

Figure 4.5 Cross-sectional SEM micrographs of ZnO pellets after sintering under 10^{-5} Torr (a) ZnO-1%Al, (b) ZnO-2%Al, (c) ZnO-3%Al with the high-magnification inset image showing the $ZnAl_2O_4$ phase (The brighter particles are $ZnAl_2O_4$ precipitates). The grain layers are parallel to the pellet surface. (d) XRD from sintered ZnO-*x*%Al (*x*=1, 2, 3) pellets sintering under 10^{-5} Torr with the inset of a zoomed-in vision of the data from the dotted box where black dots indicate peaks from $ZnAl_2O_4$. The XRD data are normalized. (e) EDS area scanning of ZnO-3%Al sintering under 10^{-5} Torr (top square is on grain surface and bottom square is on cross-section of grain).

The porous structure happens in all ZnO-Al bulk samples under vacuum conditions 10^{-1}, 10^{-2}, 10^{-3}, and 10^{-5} Torr. The samples synthesized under the high vacuum condition (10^{-5} Torr) exhibit slight better-organized correlated grain

structure (inter-connection of grains in 2D and inter-connection of layers in 3D) than that under relative low vacuum condition, such as 10^{-2} Torr shown in Figure 4.6.

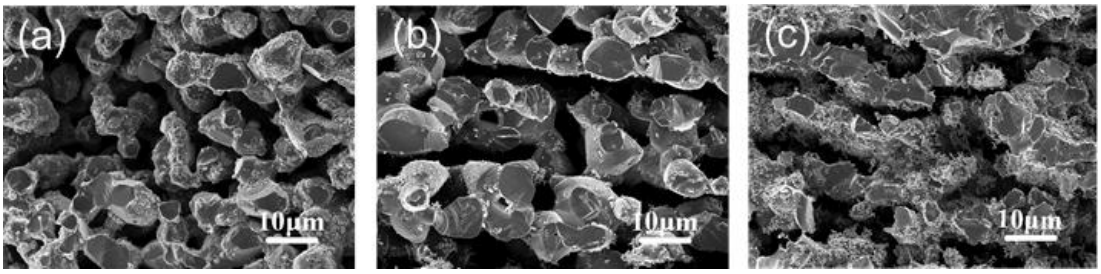

Figure 4.6 SEM micrographs of ZnO pellets after sintering under 10^{-2} Torr (a) ZnO-1%Al, (b) ZnO-2%Al, (c) ZnO-3%Al. The grain layers are parallel to the surface.

4.2 Mechanism of Structure Development

This part provides the understanding behind the formation of layered and correlated grains. To investigate the effect of synthesis atmospheres, experiments were conducted under three different conditions: vacuum (10^{-5} Torr), air and nitrogen, on the composition ZnO-2%Al, which exhibits the optimum orientation of layers under vacuum sintering condition. To understand the grain growth in different atmospheres, relative low synthesis temperatures (800 to 1100°C) were used.

According to the microstructure evolution tracing in Figure 4.7, the sintering atmosphere plays a critical role in the formation of the correlated grain structure. Under 10^{-5} Torr condition, at 800°C, the necking between nanosize grains starts to occur preferring horizontal direction (parallel to pellet surface). At 900°C, grain grows to about 400nm in conjunction with the precipitation, which is shown in the

insert figure. The horizontal grain growth becomes more obvious. With increasing sintering temperature, the grains connect to each other into layers resulting in the formation of voids with well-defined interspacing. At 1100°C, most layers consist of single layer of grains. With the same composition, however, ZnO samples sintered in air and nitrogen do not exhibit correlated grain structure. Pore smoothing and shrinking are observed at 1000°C in both Air and N_2 conditions. At 1100°C, most pores are isolated in the corner of the grain boundaries. By comparing the microstructure in N_2 and Air, there is no measurable effect from the solely nitrogen (low oxygen partial pressure) in an inert atmosphere.

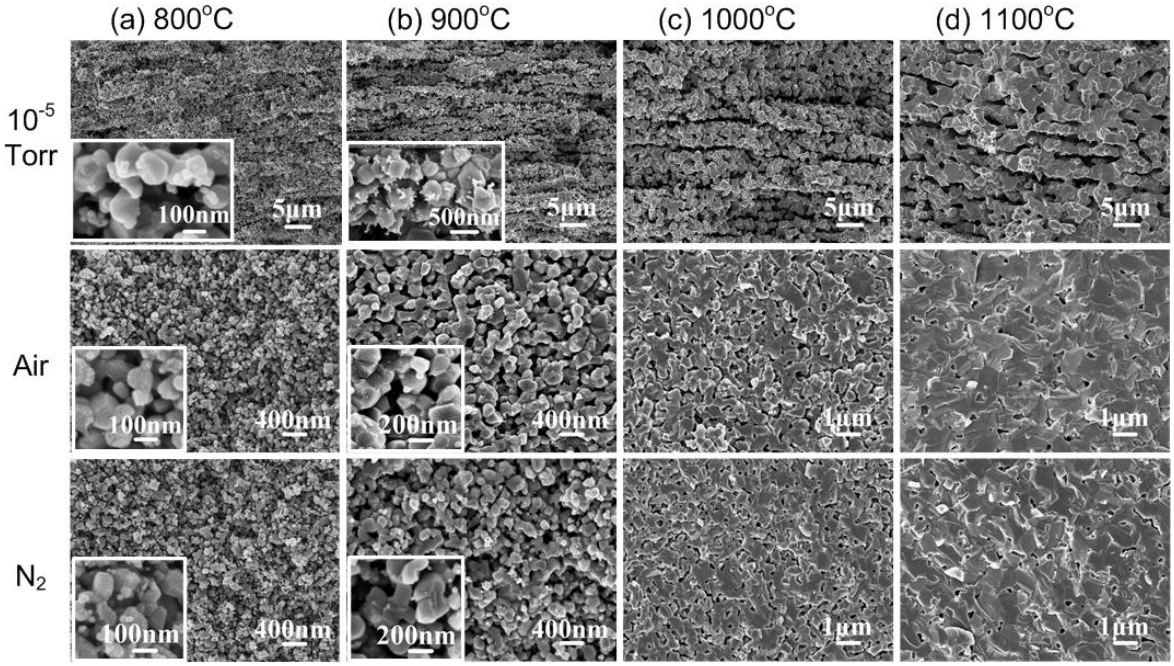

Figure 4.7 SEM micrographs from a cross-section of ZnO-2%Al bulk pellets after sintering at 800, 900, 1000, 1100°C under 10^{-5} Torr, air, and nitrogen, for 5 hours. Insets are higher magnification images. The surface of pellets is parallel to horizontal direction.

The average porosity values of ZnO-2%Al after sintering under vacuum10^{-5} Torr and Air at varying temperatures are displayed in Figure 4.8a. The samples sintered in air show continuous densification with increase in sintering temperature. Nevertheless, with higher synthesis temperature, the samples sintered in vacuum show lower porosity first and the porosity remains around 25% above 1000°C sintering temperature. Figure 4.8b shows that the grain size of both groups exhibits increasing trend with higher sintering temperature but the one in vacuum condition displays larger grain size expansion. According to the inset of Figure 4.8b, the pore sizes of samples in air slightly expand and shrinkage occurs above 1000°C. The pore of samples synthesized under vacuum, however, exhibit larger size with higher temperature. The pores under vacuum grow larger together with grain size. This is a typical coarsening phenomenon.

The solid-state sintering process is driven by the reduction in surface free energy of the consolidated mass of particles. There are typical six sintering mechanisms: lattice diffusing from grain boundary to neck, grain boundary diffusion, viscous diffusion, surface diffusion from particle to neck, lattice diffusion, and vapor transport/ gas-phase transport. The first three mechanisms lead to neck growth and densification. While the later three mechanisms result in neck growth and structure coarsening. The coarsening process reduces the driving force for densification. For ZnO, one important mechanism of grain growth at a relatively high temperature is controlled by the vaporization rate of ZnO[126].

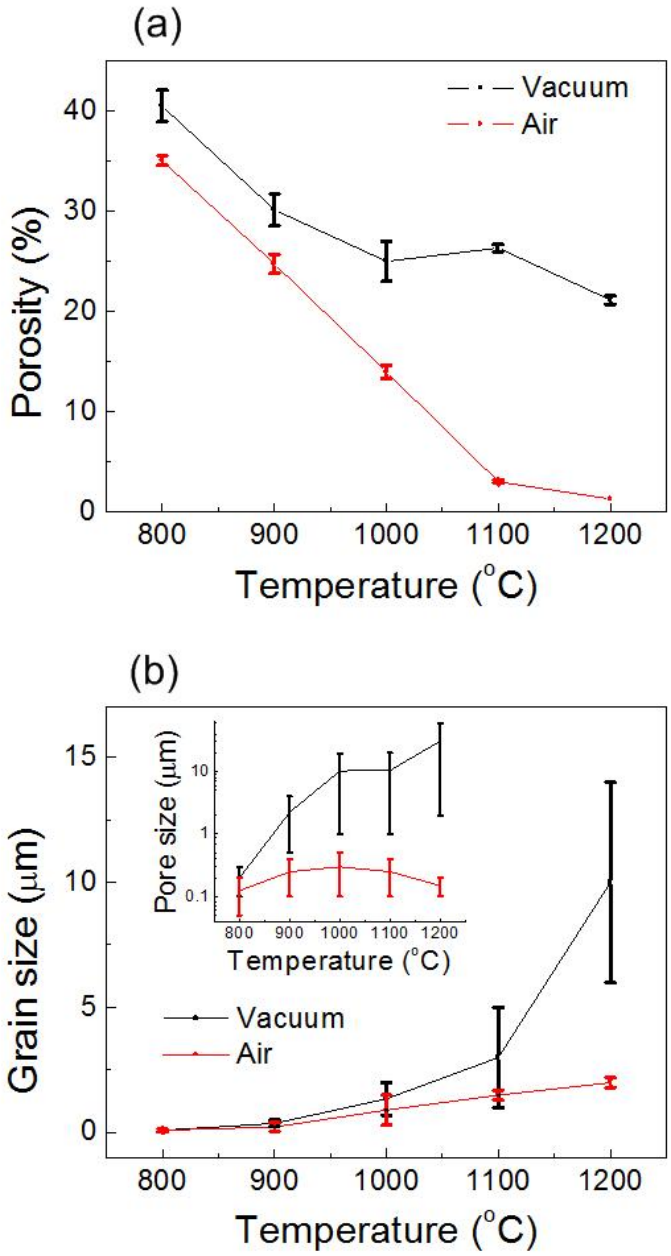

Figure 4.8 (a) Porosity of ZnO-2%Al bulk pellets after sintering in vacuum and air at varying synthesis temperatures. Quantitative microscopy was applied to determine the porosity. (b) Grain size of ZnO-2%Al sintered in vacuum and air at varying synthesis temperatures. Inset shows the pore dimension (The large variation of pore size of samples in vacuum is due to pore dimension anisotropy)

Above 900°C, particles were observed on the inside surface of quartz tube in Figure 4.9 and was detected as ZnO_x (x>1) by EDS (Table 4.1). At higher sintering temperature, more particles can be seen on the quartz. This indicates that zinc oxide gas filled the tubes during sintering and deposited on quartz during cooling down. The ZnO gas pressure is larger at higher temperature. The physical sintering (vapor transport) is one of the mechanisms of ZnO grain growth. The vacuum condition in a sealed tube together with large nanoparticle surface area enhances the sublimation of ZnO whereby vapor transport plays a dominating role during the sintering. Increasing the sintering temperature enhances the vapor transport, which simultaneously reduces the driving force for densification owing to its coarsening effect[127]. Therefore, coarsening by the vapor transport mechanism enlarges the grain size accompanied by the pore growth also, leading to the correlated grain structure with relatively high porosity. Interior of the layer with cluster of grains, another mechanism referred to as curvature-driven boundary migration[127], induces the densification in each layer at temperatures of 1100°C. Curvature-driven boundary migration also promotes the motion of pores trapped between the layers.

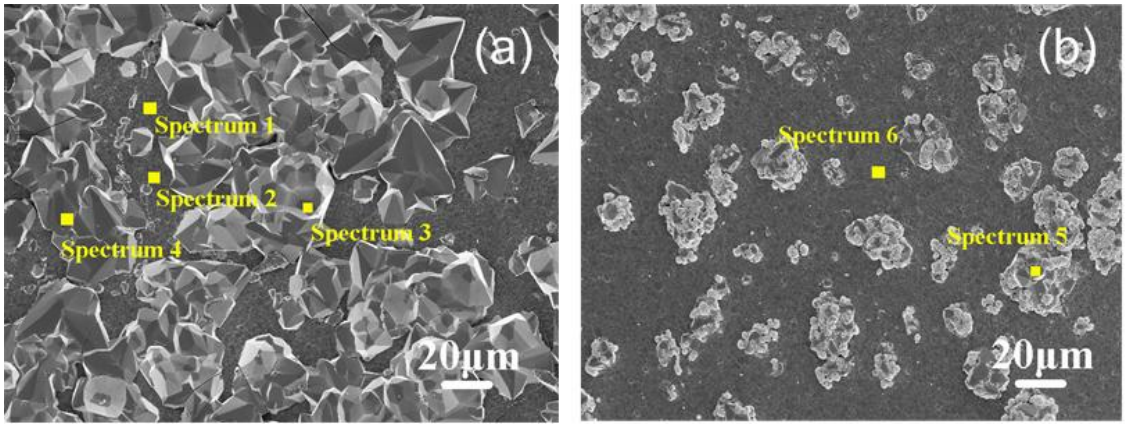

Figure 4.9 SEM micrographs from inside surface of quartz tube (a) 10^{-5} Torr, 1100°C, (b) 10^{-5} Torr, 900°C and elements analysis is listed in Table 4.1

Table 4.1 Elements analysis from the inside surface of quartz tube (used under 10^{-5} Torr, and at 1100 °C and 900°C). The micrographs are shown in Figure 4.9.

Location	O (Atomic%)	Si (Atomic%)	Zn (Atomic%)
Spectrum 1	59.69	15.21	25.10
Spectrum 2	57.64	15.47	26.89
Spectrum 3	58.26	-	41.74
Spectrum 4	53.24	-	46.76
Spectrum 5	57.41	-	42.59
Spectrum 6	47.70	16.96	35.35

The second phase also has effect on the correlated grain structure. Based on the XRD results in Figure 4.10, the peak intensity of second phase $ZnAl_2O_4$ increases with synthesis temperature under both vacuum and nitrogen. The second phase formed at higher temperature (1000°C) in comparison to the samples synthesized

in vacuum, which indicates that the vacuum condition helps in the formation of $ZnAl_2O_4$. ZnO vaporization results in Al enrichment on grain surface causing the formation of $ZnAl_2O_4$ second phase. The precipitates on the surface prevent grains belonging to upper and lower layers from connecting and favour interspaces growth between layers as shown in Figure 4.10c and d. This explains why when the Al concentration is relatively low (1 mole%), the ZnO develops microstructure close to a normal polycrystalline (Figure 4.5a and 4.6a). Thus, vacuum condition coupled with Al concentration leads to the formation of the correlated grain structure.

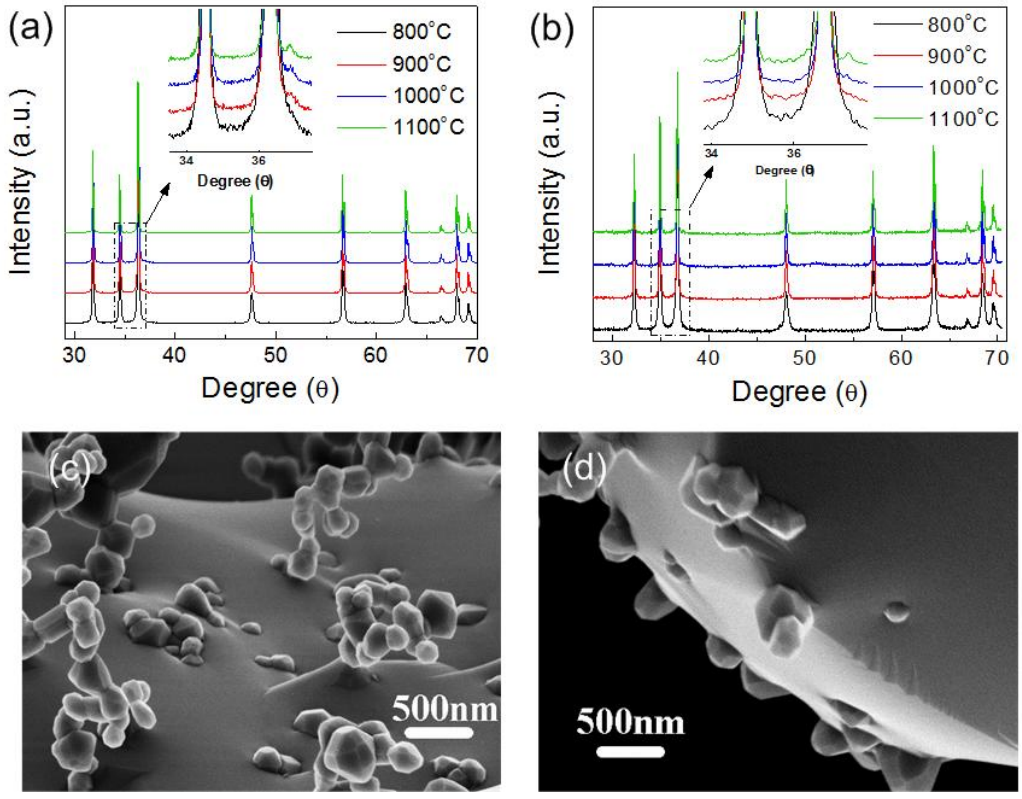

Figure 4.10 XRD of ZnO-2%Al bulk pellets after sintering at 800, 900, 1000, 1100°C in (a) 10^{-5} Torr, and (b) Nitrogen; (c) and (d) SEM micrographs of second phase nano-precipitates on the surface of one ZnO grain (ZnO-2%Al bulk pellet).

A remaining important question is why the network of grains tends to grow horizontally to develop layered structure. The second phase precipitates or pores considered in many of prior studies have symmetric structure as the shape evolution is driven by minimization of the interface energy. The asymmetric precipitate structures have been found in Sb_2Te_3-PbTe system, and energetic analysis indicated that lamellar, ribbon-like, and needle-like precipitates are residual of the interfacial energy minimization criterion[128]. The layered and correlated grain structure formation in ZnO also follows the energy minimization criterion. There is no texturing and no obvious anisotropic crystal growth, from the XRD in Figure 4.5d. The horizontal direction of grain growth is probably due to external driving forces. Thick pellets (15 mm diameter, 8 mm thickness) were pressed, diced into cubical shape, and placed in a quartz tube with different direction as shown in the schematic diagram of Figure 4.11a. According to the SEM micrographs shown in Figure 4.11a, the grain layer orientation correlates with the direction of applied pressure during uniaxial pressing. The function of the residual stress in compact powders during and after unloading might be the reason for a layered grain growth.

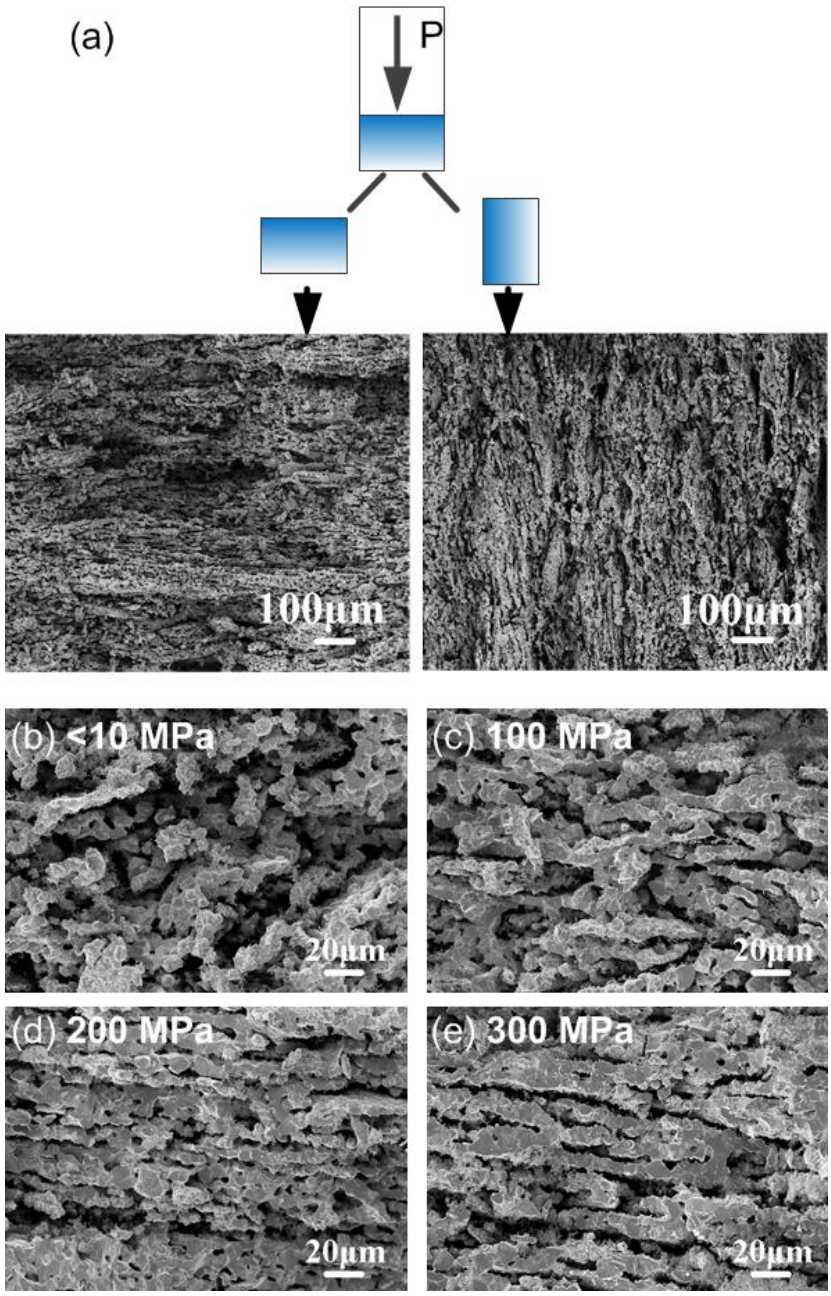

Figure 4.11(a) Schematic diagram of the axial pressing and SEM micrographs from a cross-section of ZnO-2%Al bulk pellets with 90 degree placement during sintering. The surface of left sample is placed in horizontal and the surface of right sample is placed in vertical. The color gradient shows the compaction pressure gradient in the powder compact as a result of wall friction effects. All other sample in this study had a thickness/diameter ratio of 0.13, thus the pressure gradient is negligible. (b)-(e) SEM

micrographs from a cross-section of ZnO-2%Al ceramic pressed under different pressures. The surface of pellets is parallel to horizontal direction.

Different pressing pressures were applied to see the effect on the microstructure (Figure 4.11b-e). Using low pressure (<10MPa), grain growth is not confined in a specific direction clearly. Under higher pressures (100-300MPa), the correlated grains exhibit layered structure formation. At higher pressures, the powder compact displays a stronger spring-back effect[129] during unloading. Since the spring-back is much greater in the axial direction than in the radial direction [130], powder density in the radial direction is larger than that in the axial direction. On the other hand, the stress in the axial (pressing) direction is much larger than that in the radial direction. Due to Le Chatelier principle[131], the ZnO sublimation in axial direction is stronger. Therefore grain boundary tends to form and develop perpendicular to that of the press direction.

In short, vapor transport occurring through ZnO sublimation and increased Al solubility resulting through the depleted Zn concentration on particle surface, coupled with the external factors of vacuum sintering condition and uniaxial pressing, cause the formation of layered and correlated grain structure.

4.3 Thermoelectric Performance

In prior investigations, several control parameters that include sintering atmosphere, Al doping amount, sintering temperature, and pressing pressure have been explored to quantify their influence on the evolution of layered and correlated

grain morphology. Sintering atmosphere in conjunction with pressure is an important factor towards tuning the ZnO microstructure and has governing effect on the formation of layered and correlated grain structure. ZnO-2%Al ceramics under 10^{-5} Torr are found to exhibit the microstructure where ZnO grains exhibit well-developed correlated grain structure: 2D network of grains forming layers which are connected in 3D through planar contacts. The thermal conductivity for ZnO-2%Al pellets sintered under different vacuum conditions is shown in Figure 4.12a. The data clearly indicates that all the samples with correlated-grain structure exhibit lower κ than contrast sample. It has been reported that nanosize precipitates distributed uniformly in ZnO with 2 at% Al result in low κ of 7.5 and 5.7 W/m·K at room temperature and 300 °C respectively[132]. We use this result as a reference point in this study. The contrast data is shown as the brown color plot in Figure 4.12a and the microstructure of sample is shown in inset of Figure 4.12a[132]. The lowest κ is achieved for the Al-doped ZnO ceramics synthesized under 10^{-5} Torr vacuum with magnitude of 5.2-3.0 W/m·K in the measurement temperature range of 323 K to 573 K. These magnitudes are 30% and 52% lower than the contrast sample at 323 K and 573 K respectively. This κ value is 700% lower in comparison to un-doped ZnO without correlated grain structure[5].

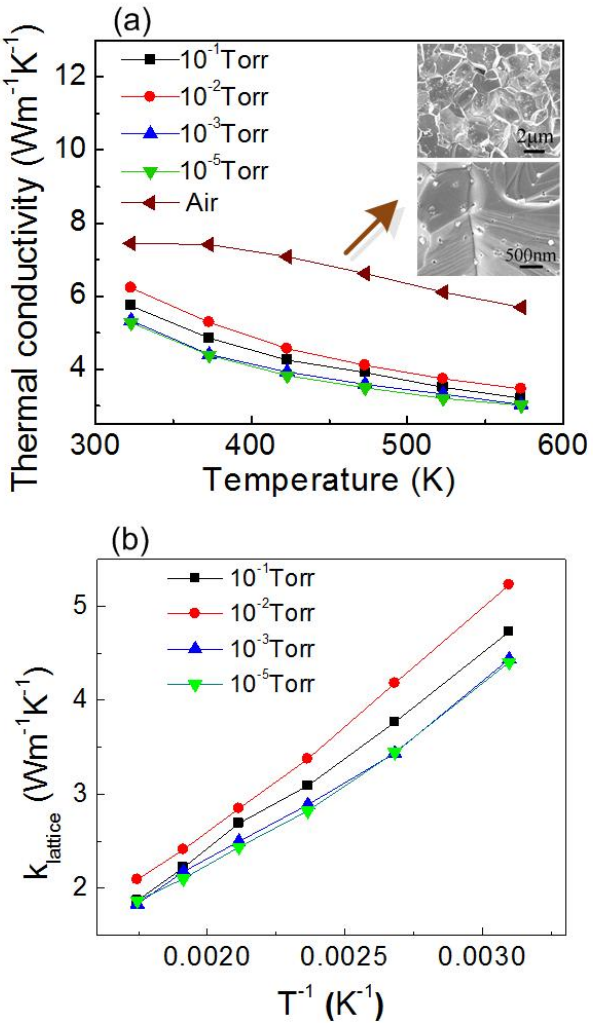

Figure 4.12 Temperature dependence of (a) thermal conductivity, and (b) lattice thermal conductivity. The contrast sample is the identically compacted and dense ZnO-Al 2% sintered under air (insert micrographs is from contrast sample[132]).

For conventional ZnO ceramics, more than 90% of the thermal conductivity is associated with lattice thermal conductivity (κ_{latt}) where contributions arise from phonon transport and the rest is related to the electron motion. The κ_{latt} of sample with layered structure is shown in Figure 4.12b, by subtracting κ_{elec} (calculated by Wiedemann-Franz law) from total κ. Here the value of κ_{latt} includes the influence

from the porosity. For ZnO-Al 2% (10^{-5} Torr), the electronic thermal conductivity is calculated to be 0.86 to 1.14 W/m·K in the temperature range of 323-573 K. The phonon transport impediment in layered correlated grains with greatly reduces the proportion of κ_{latt} in κ. Because of the low electrical conductivity and near zero electronic thermal conductivity for the contrast ZnO-Al 2% sample, its thermal conductivity value can be assumed to be equal to the lattice thermal conductivity value. Thereby, κ_{latt} of ZnO-Al 2% with a layered correlated grain structure are 58% and 32% lower that of the contrast ZnO-2%Al sample at 323 K and 573 K. Since both samples in this study and the contrast sample contain nano-precipitates, we attribute the reduction in κ mainly to the layered and correlated grain microstructure.

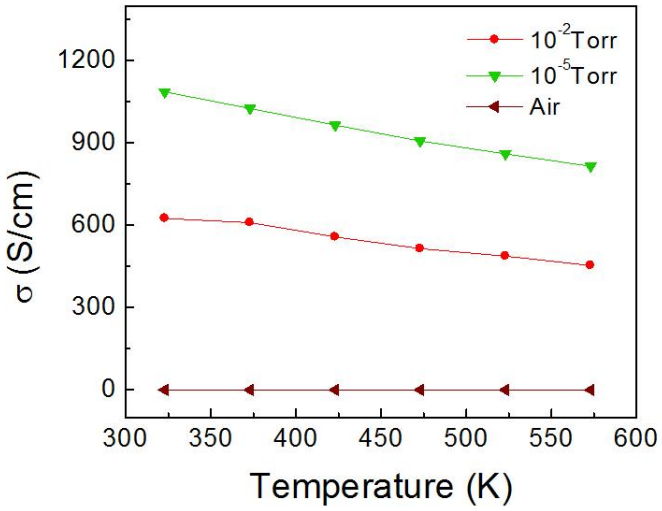

Figure 4.13 Electrical conductivity for ZnO-2%Al with layered and correlated grains.

Figure 4.13 is the electrical conductivity for ZnO-2%Al with layered and correlated grains, which is of 10^3 S/cm similar to that of thermoelectric alloys. The values are greatly enhanced when compared with the ZnO-2%Al ceramics sintered in air. Sintering under vacuum condition creates large amount of intrinsic defects, which enhances the electron concentration. The samples sintered under higher vacuum condition (10^{-5} Torr) exhibit larger electrical conductivity than that under lower vacuum level (10^{-2} Torr). The electrical resistivity of compared ZnO-2%Al is as high as 10^5 Ω.cm, due to the formation of $ZnAl_2O_4$ and Zn vacancy in the present of oxygen[112, 133]. The Zn^{2+} vacancies compensate for the free electrons in ZnO. The influence factors on electrical properties of ZnO are presented in Chapter 5.

The reduction of thermal conductivity for the Al-doped ZnO bulk is ascribed to the correlated grain structure characterized by the presence of 2D network of grains forming layers. Due to the extremely low thermal conductivity of air (0.057 W/m·K), interspacing between grain layers can act as a good thermal insulator. For solids with pores having dimensions exceeding the phonon mean free path of ZnO (about 30 nm), the effective thermal conductivity can be expressed as $\kappa = \kappa_0 \Phi(p)$, where κ_0 is the thermal conductivity of the corresponding dense material, Φ is the factor determined by the porosity p. Several estimations and models for Φ have been proposed in literatures[134-136], and the shape and orientation distribution of voids influences Φ resulting in anisotropic thermal transport properties[135]. Three two dimensional models of pore structures are displayed in Figure 4.14, and the correlated-grain structure can be simply represented by the schematic model

of Case (c). The long interspacing between the grain layers in ZnO is approximated by an ellipsoidal shaped void.

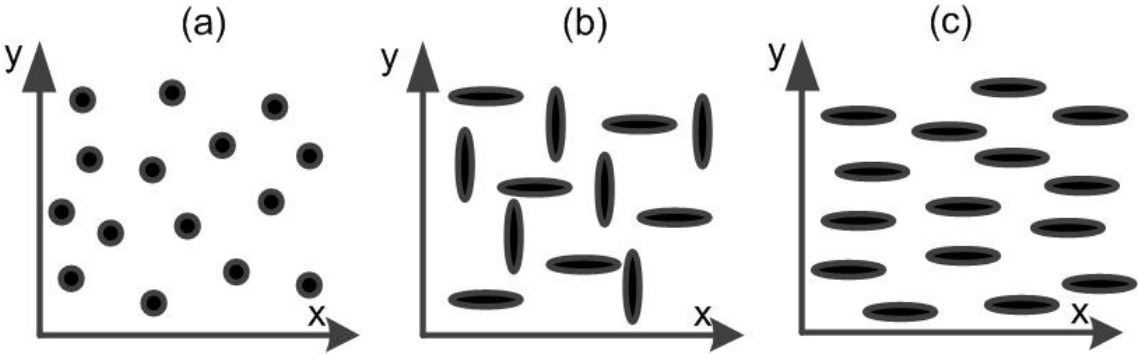

Figure 4.14 Schematic representation of the two-dimensional models of pore structures: (a) circular pores (b) elliptical pores of random orientation, and (c) elliptical pores of same orientation. The aspect ratio of the ellipsoidal pore is 1:4.

According to an estimation performed by Braginsky[136] by taking the aspect ratio of the ellipsoidal pore as 1:4, the factor of porosity Φ was found to be 1-(1+*J*) *p*, when there is no thermal transportation in pores. The magnitude of *J* equals 0.5 for thermal conductivity of pore structure shown in Case (a) and (b) and 0.1 and 0.8 along the x-axis, y-axis in Case (c) respectively. Based on Braginsky's model[136], The effective thermal conductivity exhibits the largest reduction along the y-axis in structure shown in Case (c), for which porosity factor Φ was calculated to be ~0.45 with 30% porosity. This magnitude is in good agreement with the experimental value for the ZnO with layered and correlated grains with 58% reduction of κ_{latt}. Thus, by controlling the interconnection between the grain layers, one can modulate the morphology of void and thus optimize the magnitude of thermal conductivity.

ZnO-2%Al synthesized under 10^{-5} Torr exhibited the lowest magnitude of thermal conductivity. For this sample, the Seebeck coefficient (*S*) was measured to be -58 to -72 μV/K in the temperature range of 323 to 573 K (Figure 4.15a). This results in the Power Factor (P. F.) as high as 3.67×10^{-4} W/mK^2 at room temperature, which is about 20 times larger than that of ZnO-Al nano-composites reported recently[56]. With increasing measurement temperature, the power factor increases to 4.78×10^{-4} W/mK^2 at 423 K and then slightly decreases to 4.16×10^{-4} W/mK^2 at 573 K since the σ decrease faster than the increase of Seebeck coefficient. We expect that the power factor could rise again at higher temperature because of the square dependence of *S* in P. F. and the increasing trend of *S* reported in literature[5, 56, 58].

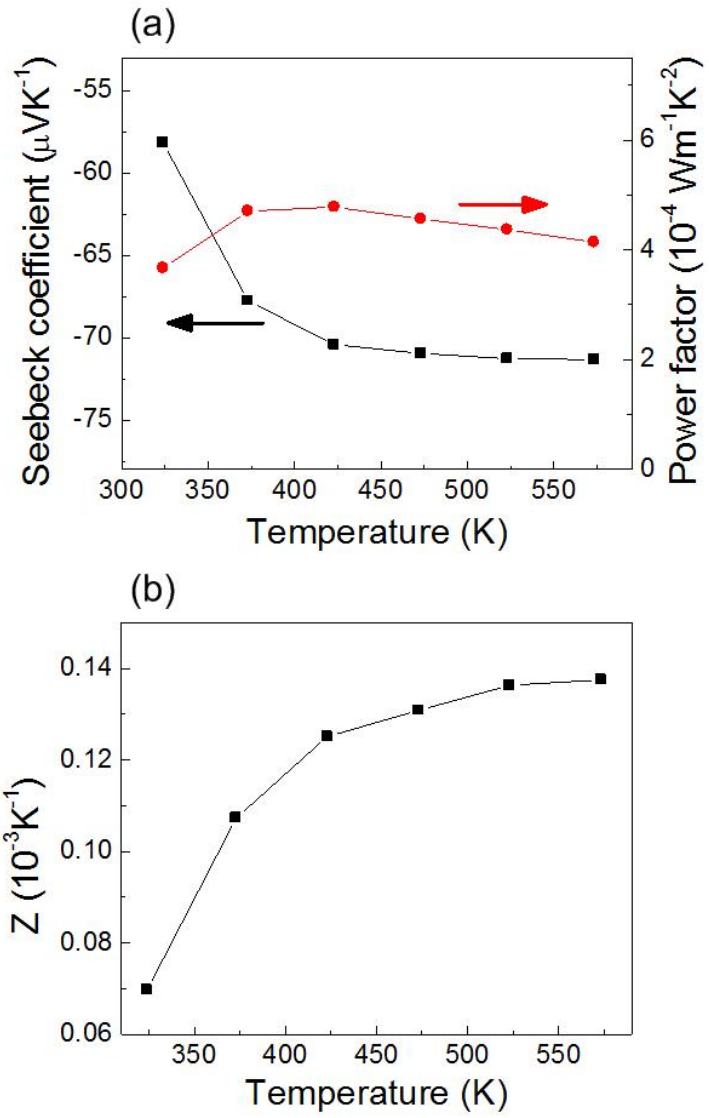

Figure 4.15 Temperature dependence of (a) Seebeck coefficient and calculated Power Factor, and (b) figure of merit Z for ZnO-2%Al sample synthesized under 10^{-5} Torr.

The figure of merit (Z) of ZnO-2%Al (10^{-5} Torr) is shown in Figure 4.15b as a function of temperature. The room temperature Z value 0.07×10^{-3} K^{-1} is about 3 times larger than that reported by Tsubota[100]. The Z value increases with

temperature and reaches $0.14\times10^{-3}K^{-1}$ at 573 K, which is also larger than the results reported in the literature[100].

4.4 Summary

We have synthesized bulk nanostructured ZnO-*x*%Al ceramics by varying doping concentration (x =1, 2, and 3) and sintering atmosphere (vacuum, air and nitrogen). The correlated-grain structure has formed when compacted samples are sintered in vacuum condition and Al additions are 2 at% and 3 at%. This microstructure consists of two-dimensional layered network of oriented grains, which interconnect in third dimension through inter-planar contact, and grains are embedded with nano-precipitates. The contact represents anisotropic connectivity of voids trapped between the grain layers. Vapor transport mechanism for grain growth dominates under vacuum leading to coarsening and void formation and therefore resulting in correlated grain structure. The vacuum condition also facilitates ZnO sublimation, promoting the formation of Al-rich secondary phase on grain surface, which favors development of correlated grain structure. The layered grain structure is related to density distribution with spring-back effect owing to uniaxial pressing, giving rise to anisotropic grain growth.

The bulk Al-doped ZnO with a layered and correlated grain structure is found to exhibit sharp reduction in thermal conductivity. Compared with the dense ZnO-2%Al with nano-precipitates, there are 30% and 52% decrease in the thermal conductivity (at 323 and 573 K) of ZnO-2%Al (10^{-5} Torr) across the grain layers. The κ_{latt} has 58% reduction at 323 K, which has a good agreement with the

reference model. The electrical conductivity is found to remain at 1000 S/cm, typical for a thermoelectric alloy. Thus, these correlated-grain structured ZnO ceramic provide enhanced thermoelectric performance, exhibiting power factor 4.78×10^{-4} W/mK^2 at 423 K and figure of merit of 0.14×10^{-3} K^{-1} at 573 K.

Chapter5 Function of the Synthesis Conditions on the Variation in Electrical Properties of Thermoelectric ZnO

Thermoelectric property of ZnO is largely influenced by its electrical property. Aluminum is the most common and effective dopant in ZnO. In order to achieve better understanding of the electrical behavior in nanostructured ZnO bulk, a systematic study on nature of Al doping and defect chemistry in ZnO under different sintering conditions has been performed in this chapter.

A study of the electrical resistivity and Al doping as a function of sintering temperature is discussed in 5.1. At constant Al addition, the electrical resistivity of ZnO exhibits a sharp decrease with increase in sintering temperature due to higher carrier density resulting from Al^{3+} substitution on Zn^{2+} sites. On the other hand, the segregation of Al in secondary phase, $ZnAl_2O_4$, promotes Zn^{2+} vacancy formation in ZnO and consequently increases the electrical resistivity. The mechanism controlling the large change in electrical resistivity of dense ZnO, ranging from insulator (~10^7 Ω.cm) to semiconducting regime (~ 0.1 Ω.cm) has been discussed in this section.

The electrical conductivity of non-stoichiometric ZnO is dependent upon sintering atmosphere and initial physical condition. The second part of this chapter reveals that the electrical conductivity of ZnO-Al 2% shows a whopping difference under different sintering atmospheres. Low oxygen pressure improves Al doping in ZnO, increases the interstitial Zn and impedes Zn vacancy formation. Mixing ZnO and Al_2O_3 by ball milling and sol-gel chemical synthesized ZnO-Al powders were used as the starting powders, and influence of initial physical condition on electrical behavior of ZnO has been compared.

5.1 Sintering Temperature Dependent Chemical Defects and the Effect on the Electrical Resistivity of ZnO

5.1.1 Synthesis and phase analysis

ZnO modified with 2 mole% Al (simplified as ZnO-Al) were synthesized using nanosize precursor powders of ZnO (~ 30 nm, purity >99.7%, Advanced Materials LLC) and Al_2O_3 (40-50 nm, purity > 99.5%, Alfa Aesar) through solid-state reaction. The mixed powders were pelletized and consolidated using cold isostatic pressing (CIP) at 200 MPa and then sintered at 950, 1100, 1200, 1300, 1400 °C all for 5 h in air. The density of the samples was measured to be 5.37, 5.48, 5.48, 5.47, and 5.44 g/cm^3 respectively using Archimedes' method.

XRD spectra of ZnO-Al samples as a function of sintering temperature are shown in Figure 5.1. These patterns show the formation of a hexagonal wurtzite-type zinc oxide phase (JCPDS # 36-1451). A small fraction of the gahnite phase, $ZnAl_2O_4$ (JCPDS # 5-0669) is detected in all samples, which can be seen clearly in Figure 5.1b. Figure 5.1c shows the change of unit cell volume of ZnO-Al samples sintered in the temperature range of 950-1400 ºC. When the sintering temperature changes from 950 to 1200 ºC, an expansion in unit cell volume can be noticed. The smaller unit cell volume below 1200 ºC sintering temperature is probably caused by the dissolution of ZnO in Al_2O_3 and formation of $ZnAl_2O_4$ phase. With increase in sintering temperature from 1200 ºC to 1400 ºC, there is a slight decrease in unit cell volume, likely because the solubility of Al in ZnO rises with temperature according to the phase diagram of ZnO-Al_2O_3 (Figure 1.17). With increasing temperature, more Al^{3+} ions occupy the Zn^{2+} sites and consequently lead

to a decrease in the volume of unit cell, as ionic radius of Al^{3+} (0.39 Å) in four-fold-coordination is smaller than Zn^{2+} (0.60 Å).

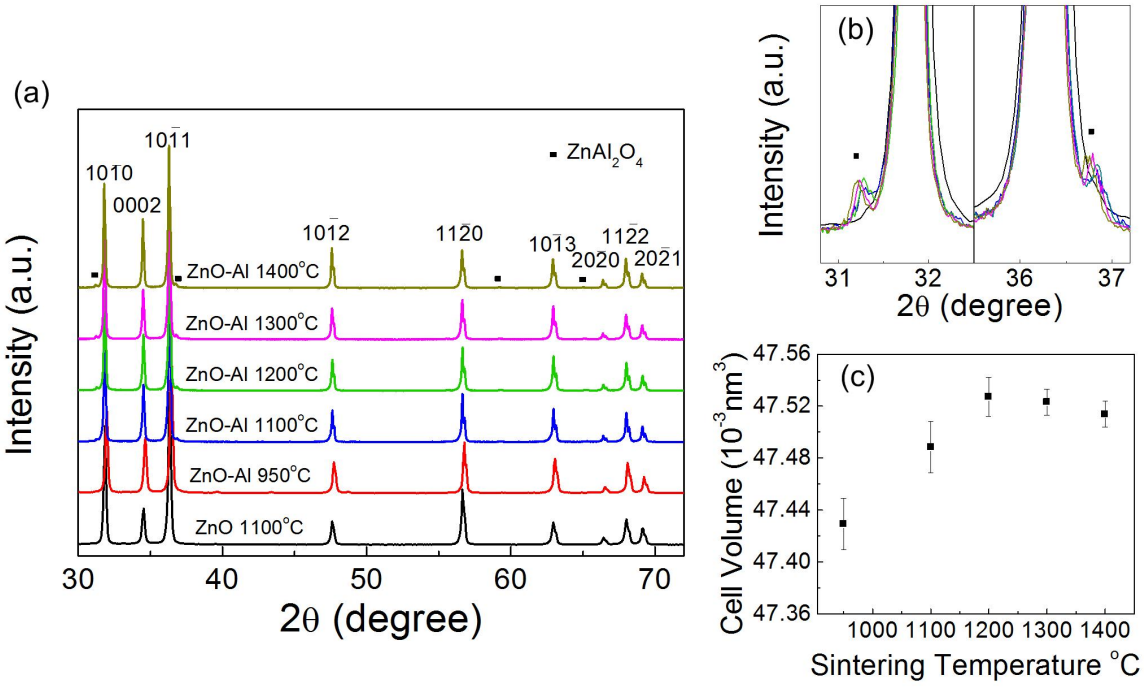

Figure 5.1(a) XRD pattern of ZnO-Al sintered at different temperatures and compared with the pure ZnO sintered at 1100 ºC; (b) higher magnification of the XRD pattern (c) the unit cell volume changes of ZnO-2%Al sintered at different temperatures.

The SEM images of the ZnO-Al ceramics are displayed in Figure 5.2a. All samples are found to exhibit dense microstructure except the ones sintered at 950 ºC, which is in agreement with the measured densities. The average grain size increases with sintering temperature[137] as shown in Figure 5.2b. A small amount of second phase precipitates can be observed in all the ZnO-Al samples in insert figures of Figure 5.2a. At higher sintering temperature, precipitates with larger size are observed in SEM images. The element scanning on a typical ZnO-Al sample sintered at 1300 ºC confirms that the distribution of

aluminum is richer in the precipitate phase (spectrum 1 and 3) as compared with the matrix ZnO (spectrum 2) as shown in Figure 5.2c.

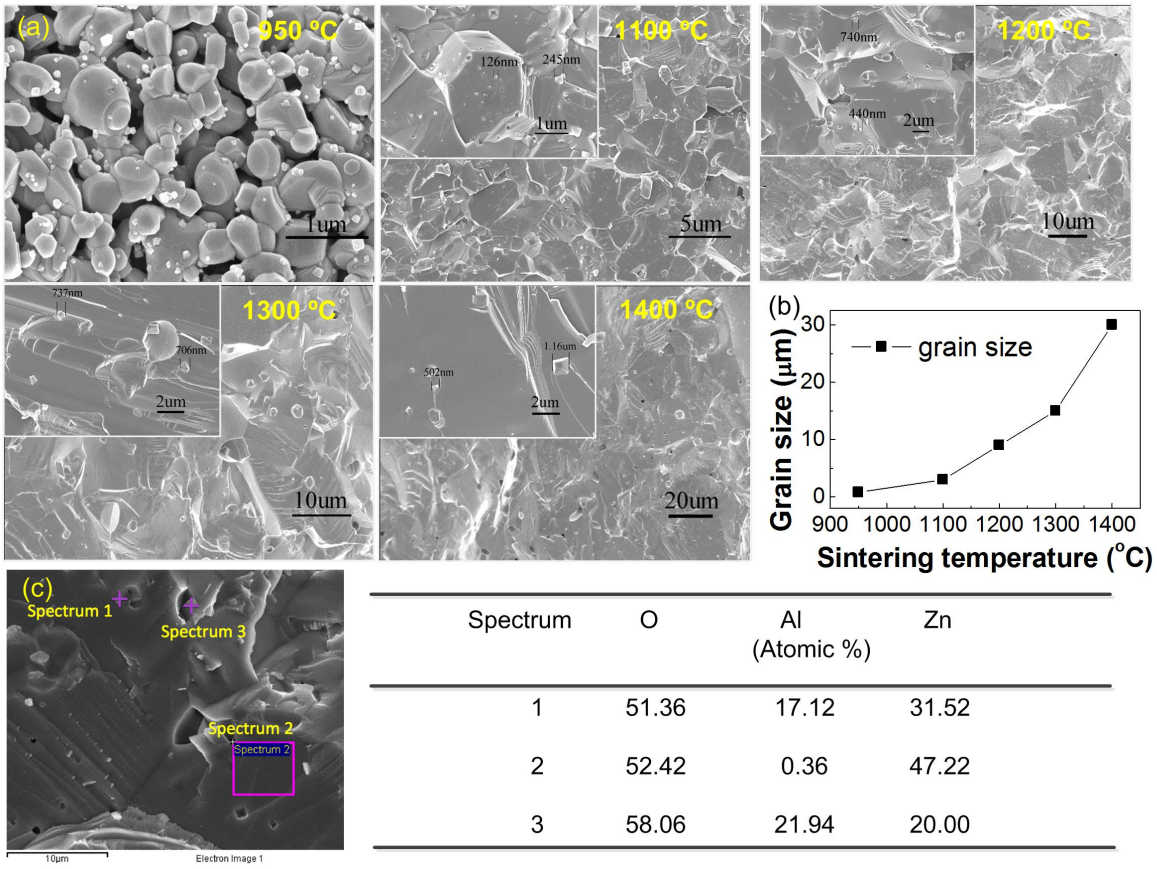

Spectrum	O	Al (Atomic %)	Zn
1	51.36	17.12	31.52
2	52.42	0.36	47.22
3	58.06	21.94	20.00

Figure 5.2 (a) and (b) SEM micrographs and grain size of ZnO-Al sintered at different temperatures. The insert figures are higher magnification images. (c) EDS element scanning of ZnO-Al sintered at 1300 ºC. Table of atomic element compositions is included in the figure.

5.1.2 Electrical resistivity

Electrical resistivity (ρ) of ZnO-Al samples exhibits significant variations as a function of sintering temperature as shown in Figure 5.3a. Electrical resistivity was measured by

Van der Pauw method for relatively low resistivity samples and by voltage-current method for samples with high resistivity. The higher value of ρ at lower sintering temperature (950°C) might be attributed to the porous microstructure (Figure 5.2a). The densities for the samples synthesized in the temperature range of 1100-1400°C are similar, and therefore not a deterministic parameter. With increase in sintering temperature, the values of electrical resistivity decrease sharply, from ~10^6 Ω.cm for 1000°C sintering to ~ 0.1 Ω.cm for 1400°C. According to the Hall effect measurements at room temperature (Figure 5.3a), the main reason for electrical conductivity enhancement with increasing sintering temperature is related to the increase in carrier density. When the sintering temperature increase from 1200°C to 1400°C, the carrier density increases from 1.45×10^{15} to 3.13×10^{18} cm^{-3}. The carrier density values of ZnO-Al synthesized at relatively low temperature (< 1200°C) are not provided since the carrier concentration is low and not detectable.

The variation of ρ as a function of measurement temperature for the typical ZnO-Al synthesized at 1400°C shows the decreasing trend with increase in temperature (Figure 5.3b). Assuming the carrier concentration is constant with measurement temperature, the carrier mobility in the grain is determined by the impurity (doping ions). The impurity scattering decreases at higher temperature while the scattering from lattice increases with temperature. This indicates that the ZnO-Al samples had high concentration of impurities, such as dopant, vacancies or interstitial atoms.

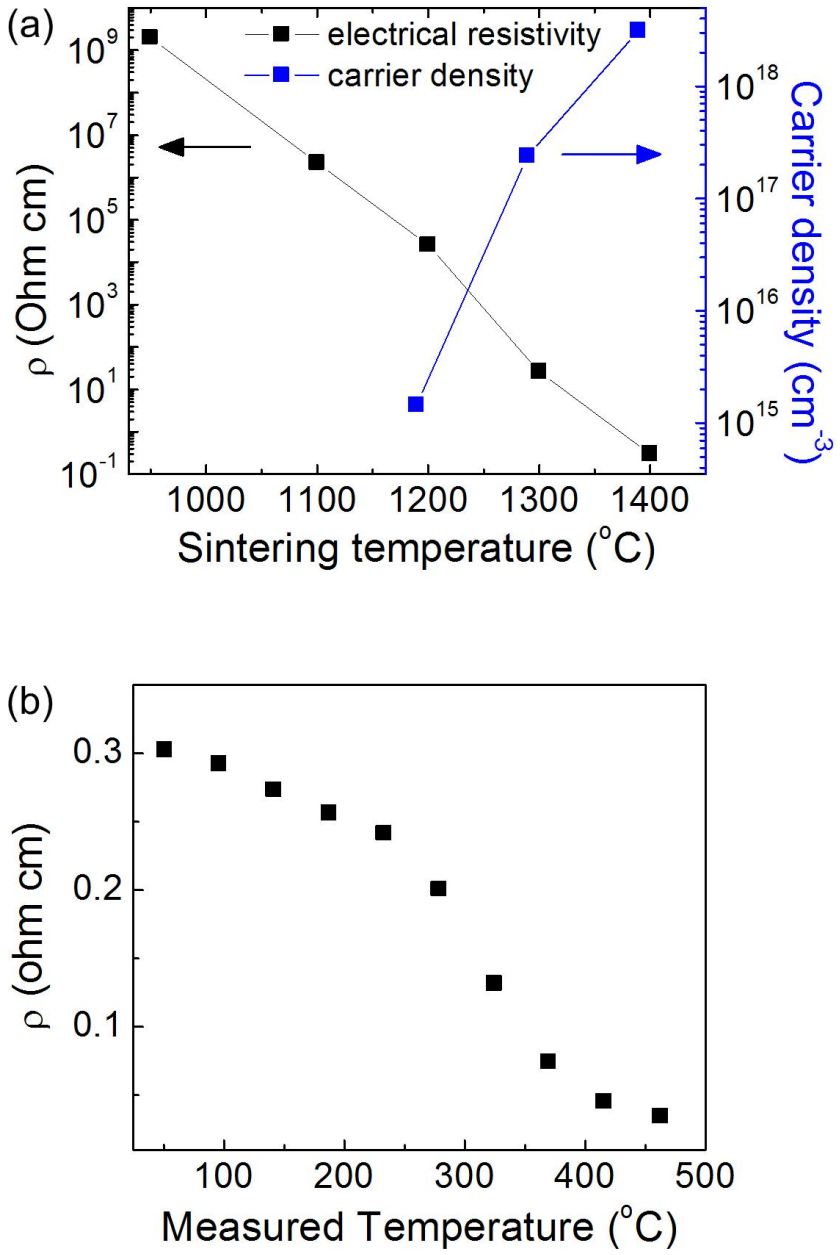

Figure 5.3 (a) Room temperature measurement of electrical resistivity and carrier density of ZnO-Al sintered at different temperatures; (b) Temperature dependence of electrical resistivity of ZnO-Al sintered at 1400ºC.

To understand the variation of resistance in the interior of grain and at the grain boundary, impedance measurements were conducted as shown in Figure 5.4. The

impedance spectrum of ZnO-Al sample sintered at 1100°C exhibits two overlapping semicircles. The proposed equivalent circuit[138-140] for this type of spectra is combination of a resistor R_s and two parallel RC networks (Fig. 5.4). The R_s mainly represents the contact resistance of the sample and the silver electrode, R_g, CPE_g, R_{gb} and CPE_{gb} are resistance and capacitance from grain interior and grain boundary. Here considering the capacitance in material will not be ideal, CPE (constant phase element) is used and defined by CPE-T and CPE-P. CPE is identical to an ideal capacitor when CPE-P equals one. The high frequency (low magnitude of real component Z') and the low frequency (high magnitude of real component Z') correspond to the grain interior ($ZnAl_2O_4$ precipitates) and grain boundary resistance respectively. At higher sintering temperature, the impedance spectra display a single oblate arc, as the time constants for grain interior and grain boundary were identical. The equivalent circuit fitting results show good matches with measured plots and parameters are listed in Table 5.1. After sintering at higher temperature, samples' resistance and capacitive reactance ($(2\pi fC)^{-1}$) from both grain interior and grain boundary decrease sharply, and the corresponding frequency (f_{max}) increases. These indicate the enhancement in electron mobility through grain interior and grain boundary. Significant decreases of Both R_g and R_{gb} contribute to the overall lower magnitude of electrical resistivity at relatively higher sintering temperature. Considering that the thickness of grain boundary is smaller than the grain interior of ZnO-Al, the grain boundary should have larger resistivity than the grain interior, which plays an important role towards electrical resistivity.

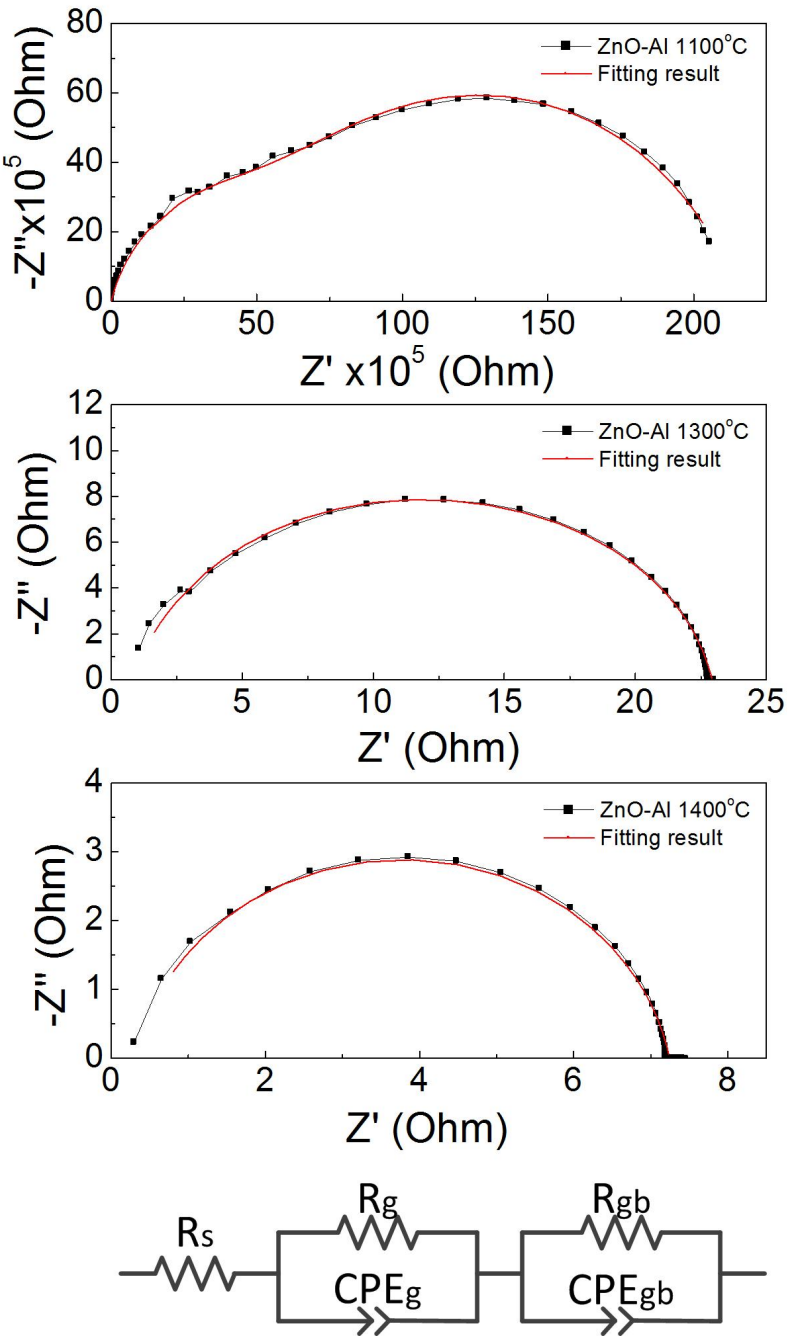

Figure 5.4 The impedance spectra of ZnO-Al sintered at different temperatures and the equivalent circuit model. The fittings in red line are fitted using the equivalent circuit model and the results are listed in table 5.1.

Table 5.1 Parameters obtained by equivalent circuit model fitting of the impedance data.

Sintering Temperature (°C)	1100	1300	1400
R_g (Ohm)	5.0×10^{6}	8.9	1.0
CPE-T_g (nF)	2.8	2.2×10^{2}	3.6×10^{3}
CPE-P_g	0.83	0.97	0.94
$f_g$max (Hz)	11.4	8.13×10^{4}	4.42×10^{4}
R_{gb} (Ohm)	1.7×10^{7}	13.1	5.9
CPE-T_{gb} (nF)	14.1	1.9×10^{3}	1.4×10^{3}
CPE-P_{gb}	0.76	0.89	0.87
f_{gb}max (Hz)	0.664	6.4×10^{3}	1.93×10^{4}
R_s (Ohm)	1.9×10^{-9}	1.0	0.3

The variation of electrical resistivity of samples can be understood through changes in defect chemistry (defects created by doping and intrinsic defects). To better understand the Al doping, absorbance spectra of ZnO-Al samples in the wavelength range of 200-1000 nm were collected as shown in Figure 5.5a. These spectra reveal slight red shift of absorption edge with increase in sintering temperature. Based on the double derivative of absorbance spectra (insert of Figure 5.5a), the optical band gap of doped ZnO was calculated. The values are found to slightly increase from 3.09 eV for the ZnO-Al sample sintered at 1100°C to 3.16 eV for the one sintered at 1400 °C. The widening of the optical band gap in the samples sintered at higher temperature was consistently observed. As

shown in the schematic band structure in Figure 5.5b and c, the associated electrons released from ionized Al atoms occupying the bottom of the conduction band widen the optical band gap. This is commonly known as Burstein-Moss Effect[141]. The occupation of the lowest states in the conduction band enhances the band gap as[142]:

$$\Delta E_g^{Burstein-Moss} = \frac{h^2 k_F^2}{2}\left[\frac{1}{m_e} + \frac{1}{m_h}\right] \tag{5.1}$$

where k_F is the Fermi wave vector, m_e and m_h are the effective mass for electrons in conduction band and holes for valence band. The same phenomenon in Al-doped ZnO thin film was reported by Sernelius et al.[142]. Higher electron concentration in conduction band probably results from the defects created through Al doping, which is consistent with the unit cell volume calculated from XRD. More Al atoms dissolve in the ZnO at higher synthesis temperature resulting in slight unit cell shrinkage.

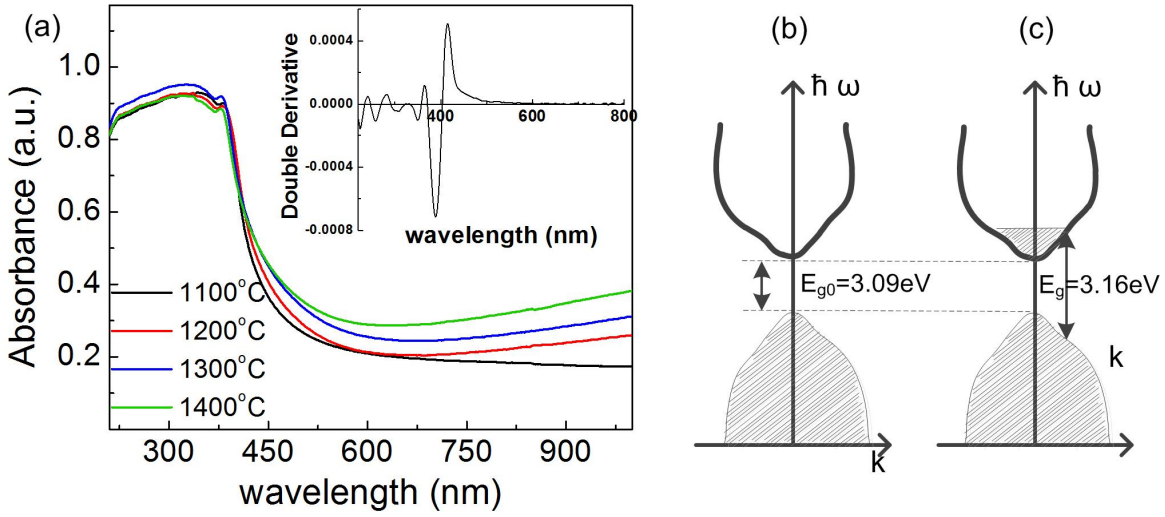

Figure 5.5 (a) UV-VIS-NIR spectra of ZnO-Al sintered at different temperatures and inset is double derivative of the absorbance for band gap; (b) Schematic band structure of ZnO with parabolic conduction and valence bands; (c) Schematic band structure of Al doped ZnO.

The concentration of intrinsic defects varies with the sintering temperature also. Studies on ZnO have shown that the intrinsic defects play an important role on the electrical property[6]. Photoluminescence (PL) spectra at the excitation wavelength of 325 nm for the ZnO-Al samples are shown in Figure 5.6. The PL intensity reduces with increasing sintering temperature owning to the carrier density enhancement. Lupan et al.[143] have reported that the lower carrier density results in the PL intensity augmentation. This again affirms the above discussion that Al doping concentration in ZnO lattice increases resulting in the enhancement of the carrier density. The green luminescence, or deep band emissions observed at 2.5eV and 2.35eV is attributed to the oxygen vacancy (V_O) and zinc vacancy (V_{Zn}) (marked in Figure 6). V_{Zn} has been reported to be the source of green

emission at 2.35 eV and V_O at 2.42- 2.53 eV in several earlier studies[144, 107, 145]. The broad spectral distribution of oxygen vacancies indicates that hybridization may be occurring that results in redistribution of the energy widening the range of these defects.

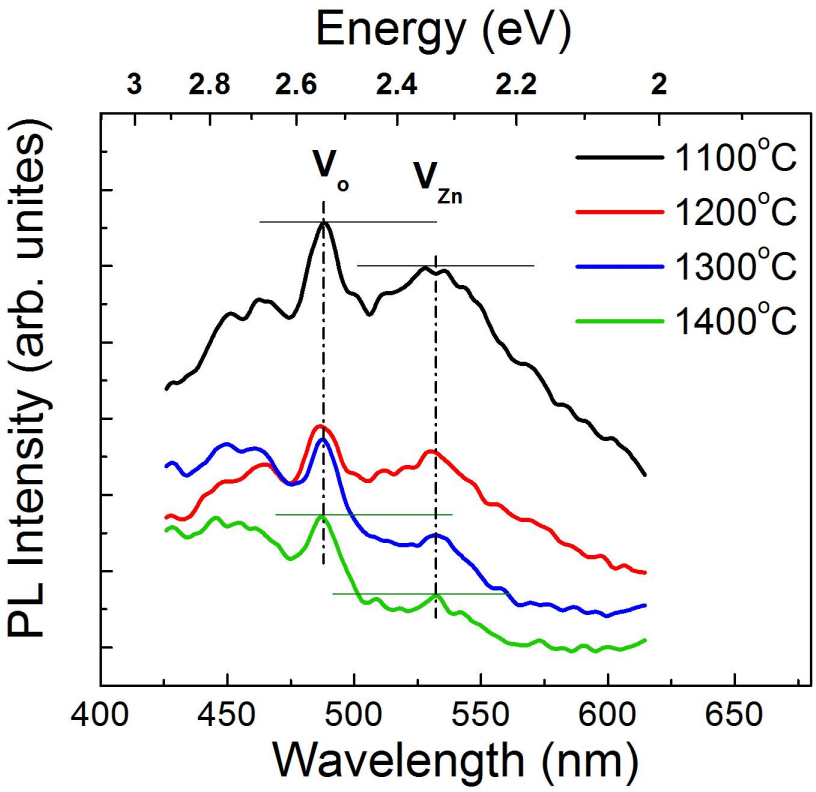

Figure 5.6 The PL spectra of ZnO-Al sintered at different temperatures. The emission energy representing the zinc vacancies and oxygen vacancies is shown in the figure.

The presence of oxygen vacancies is further confirmed by thermally stimulated depolarization current (TSDC) measurements in Figure 5.7. Recently, Matsudo et al.[146] and Yan et al.[147] have conducted TSDC measurement on the piezoelectric ceramics and have shown that large current anomaly around 370°C is related to the relaxation of

oxygen vacancies. We believe that peak observed in the ZnO-Al sintered at 1100°C is also related to the relaxation of intrinsic oxygen vacancies.

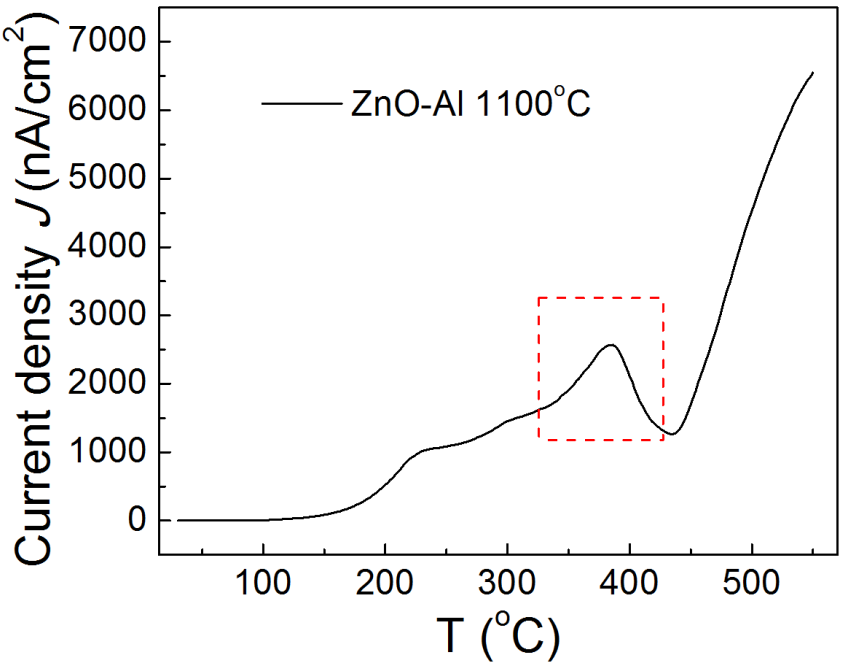

Figure 5.7 Thermally stimulated depolarization current of ZnO-Al 1100°C

The PL intensity ratio of peaks at 480nm and 535nm increases (the emission intensity difference from V_O and V_{Zn} increases) with higher sintering temperature, indicating the relative decrease in population of Zn vacancies. The population of Zn vacancies goes up with decrease in sintering temperature, which is in agreement with the changes in the cell volume. As the electron acceptor, V_{Zn}^{2-} and V_{Zn}^{-} compensate free electrons and in turn contribute towards the reduction of electrical conductivity[6, 107, 108]. In general, ZnO is a native *n*-type semiconductor; thereby, the V_{Zn} appearance is an important factor for high

resistivity of ZnO-Al ceramics sintered at relatively low temperature. Whether oxygen vacancies contribute to the carrier density is still under investigation[6].

Above results provide the explanation for large variations in electrical resistivity with sintering temperatures in Al_2O_3-modified ZnO. In the solid-state reaction of ZnO and Al_2O_3, there are two most likely reactions, namely, Al^{3+} substitution on Zn^{2+} and Al^{3+} forming the gahnite phase[109, 112, 118, 148]. These reactions can be expressed as:

$$Al_2O_3 \xrightarrow{ZnO} 2Al_{Zn}^{\cdot} + 2e' + 2O_o^{\times} + \frac{1}{2}O_2 \tag{5.2}$$

$$ZnO + Al_2O_3 \xrightarrow{ZnO} \mathrm{Zn}Al_2O_4 \tag{5.3}$$

$$Al_2O_3 + (Zn_{Zn}^{\times} + 2e' + \frac{1}{2}O_2)_{ZnO} \xrightarrow{O_2} \mathrm{Zn}Al_2O_4 + (V_{Zn}'')_{ZnO} \tag{5.4}$$

The dissolved Al^{3+} acts as a donor and, subsequently enhances the electrical conductivity according to Eq. (5.2). Secondary phase $ZnAl_2O_4$ is precipitated during the sintering as shown by Eq. (5.3), because of the limited solubility of Al_2O_3 in ZnO. This reaction preferably promotes the generation of Zn^{2+} vacancies (Eq. 5.4), (required oxygen obtained from air) which, in turn, compensates the free carriers, and subsequently reduces the electrical conductivity. All the reactions shown in Eq. (5.2) – (5.4) occur simultaneously and their relative contributions vary with synthesis temperature. At low sintering temperature, such as 1100ºC, the reaction (5.3) or (5.4) are prevalent. Most of the alumina is consumed towards the formation of $ZnAl_2O_4$ phase. Thereby the

concentration of Al^{3+} ions occupying the ZnO lattice is very small. Reverse dissolution of Zn^{2+} into Al_2O_3 creates Zn vacancies that compensate the free electrons. This reaction is well supported by the XRD measurements showing the unit cell dimension shrinkage. Thus, the ZnO-Al samples sintered at relatively low temperature exhibits very high resistivity. With increase in sintering temperature, higher fraction of Al^{3+} ions occupy Zn site releasing free electrons at shallow energy level resulting in higher carrier concentration. Related to the impedance spectrum, the decrease of grain electrical resistivity (ρ_g) with increase in sintering temperature is mainly due to the higher amount of Al incorporation in ZnO matrix. The decrease of grain boundary electrical resistivity (ρ_{gb}) occurs owning to enhanced Al doping at higher sintering temperature, reduced grain boundary area, and better lattice arrangement during at higher sintering temperature.

5.1.3 Summary

This part has been focused on sintering temperature related electrical resistivity of zinc oxide bulk. The dense ZnO-Al samples exhibited a large difference in electrical resistivity ranging from insulator (~10^7 Ω.cm) to semiconductor (~0.1 Ω.cm). Both the resistivity of grain interior and the grain boundary are found to reduce significantly with sintering temperature. At lower temperature, Al mainly exists in the secondary phase $ZnAl_2O_4$, which promotes the formation of Zn^{2+} vacancy and consequently decreases the carrier density. With increase in sintering temperature, higher concentration of Al incorporates in the ZnO, leading to electrical conductivity increase.

With varying temperature, the phase diagram governs the phase evolution between ZnO and Al_2O_3 and thus selection of specific sintering temperature is critical towards defining

the role of Al in ZnO. In order to synthesize ZnO with low thermal conductivity by nanostructures and high electrical conductivity, synthesis techniques that can achieve high doping concentration at relatively low temperature are required. Chemical synthesis technique would be one such possibility to achieve uniform mixture of Al-ZnO and thus enhance the concentration of Al in ZnO [56].

5.2 Role of Sintering Atmosphere and Synthesis Processing on Electrical Properties of Thermoelectric ZnO

As discussed in section 5.1, ZnO-2%Al exhibited a large difference in electrical resistivity at varying sintering temperatures. One important reason for high electrical resistivity is electron compensator Zn^{2+} vacancy, whose formation requires oxygen in sintering atmosphere. As a non-stoichiometric solid, the defects in ZnO are strongly related to surrounding atmosphere. The variation of defects on the other hand influences carrier density too. Therefore the sintering atmosphere is another important condition to control the electrical property of ZnO. In this part, the electrical conductivity of ZnO under different sintering atmospheres and initial physical conditions is investigated; Al doping and chemical defects changes are discussed.

5.2.1 Effect of nitrogen and air on electrical conductivity

ZnO-2%Al samples were sintered at 1400°C for 5 hours, under atmosphere of air and nitrogen. The starting powders were mixing ZnO and Al_2O_3 powders through ball-milling process (same as process in 5.1, using nanosize precursor powders ZnO ~ 30 nm and Al_2O_3 ~ 50 nm). XRD spectra of samples are shown in Figures 5.8a. Both patterns show

the formation of a hexagonal wurtzite-type ZnO phase and a small fraction of the gahnite phase, $ZnAl_2O_4$.

Figure 4.8b-c shows the SEM images from across section of ZnO-2%Al pellets sintered under air and nitrogen respectively. Both samples display a dense structure, embedded with a small amount of second phase precipitates, which can be seen in the insert figures. The sizes of precipitates in both ZnO-2%Al samples are similar. The grain size of ZnO under nitrogen is smaller (about 10μm) than the one under air (above 20μm). Several previous studies revealed that zinc ion diffusion is responsible for the sintering[149-151]. Oxygen diffusion in ZnO lattice is several orders of magnitude slower than zinc diffusion [150]. The oxygen from atmosphere diffuses along ZnO grain boundaries reacts with zinc during the sintering, which speeds up the sintering[150]. Hence, under air, the rate of ZnO sintering and grain growth is faster, compared with condition lack of oxygen.

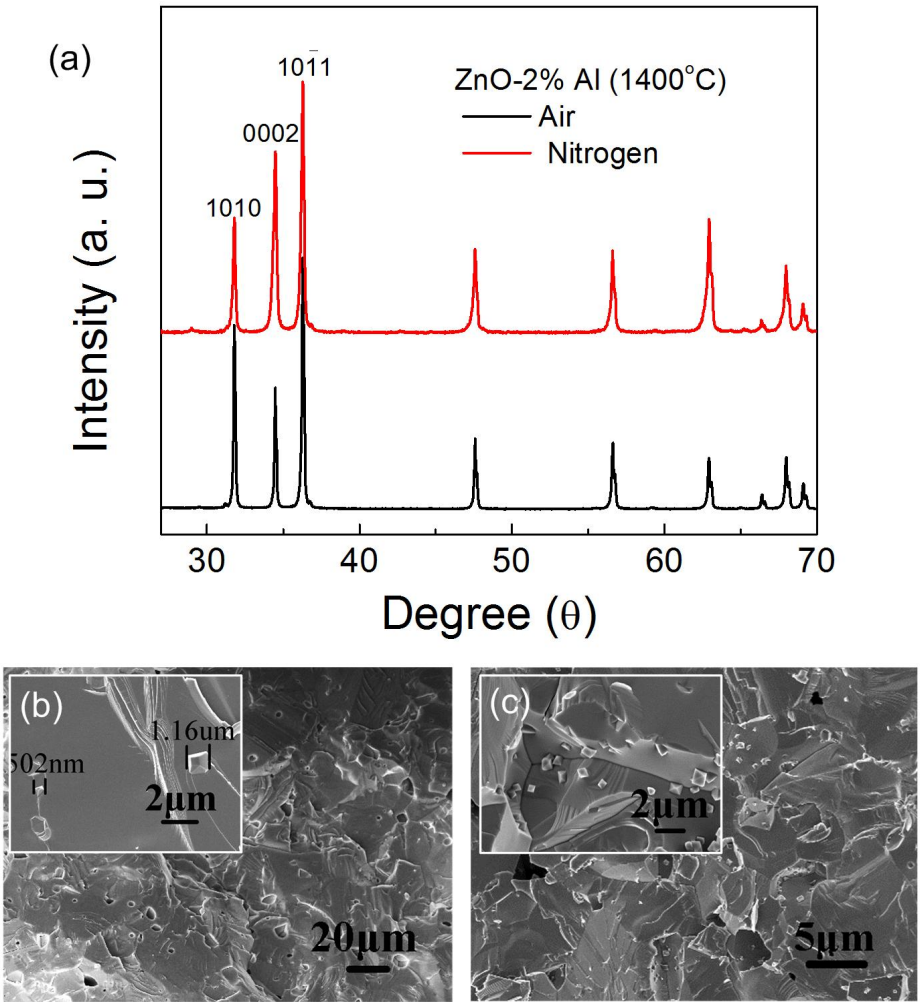

Figure 5.8 (a) XRD of ZnO-2%Al sintered under air and nitrogen at 1400ºC; SEM micrographs (across section) of ZnO-2%Al sintered under (b) air and (c) nitrogen at 1400°C. Insets are higher magnification images showing secondary phase precipitates.

Figure 5.9 shows the electrical conductivity of these two samples. It can be seen that the electrical conductivity of ZnO-2%Al under the nitrogen atmosphere displayed larger values as a function of measurement temperature, about 10 times of that in air. In the

solid-state reaction of ZnO and Al_2O_3 during sintering, there are two most likely reactions [109, 112, 118, 148]. In atmosphere with oxygen, these reactions can be expressed as:

$$Al_2O_3 \xrightarrow{ZnO} 2Al_{Zn}^{\cdot} + 2e' + 2O_o^{\times} + \frac{1}{2}O_2 \tag{5.2}$$

$$Al_2O_3 + (Zn_{Zn}^{\times} + 2e' + \frac{1}{2}O_2)_{ZnO} \xrightarrow{O_2} \mathrm{Zn}Al_2O_4 + (V_{Zn}'')_{ZnO} \tag{5.4}$$

One product of the Al_2O_3 doping reaction is oxygen. Based on the Le Chatelier principle[131], lack of oxygen helps the reaction 5.2 processing forward, which can enhance the amount of Al as dopant in ZnO, resulting in an increase in free carriers. According to reaction 5.4, Zn vacancies are more likely to appear with the existence of oxygen, so nitrogen atmosphere impeded the zinc vacancies formation. Zinc vacancies compensate free electrons and cause a high electrical resistivity[107, 108]. Further, there are more amount of interstitial zinc defects in ZnO bulk sintered under nitrogen. Interstitial zinc plays as electron donor also[107]. Besides, electrical conductivity increases with measurement temperature. Assuming the donor atoms are ionized and carrier concentration is constant with temperature change, carrier scattering is determined by impurity. The impurity scattering decreases at higher temperature while the scattering from lattice increases with temperature.

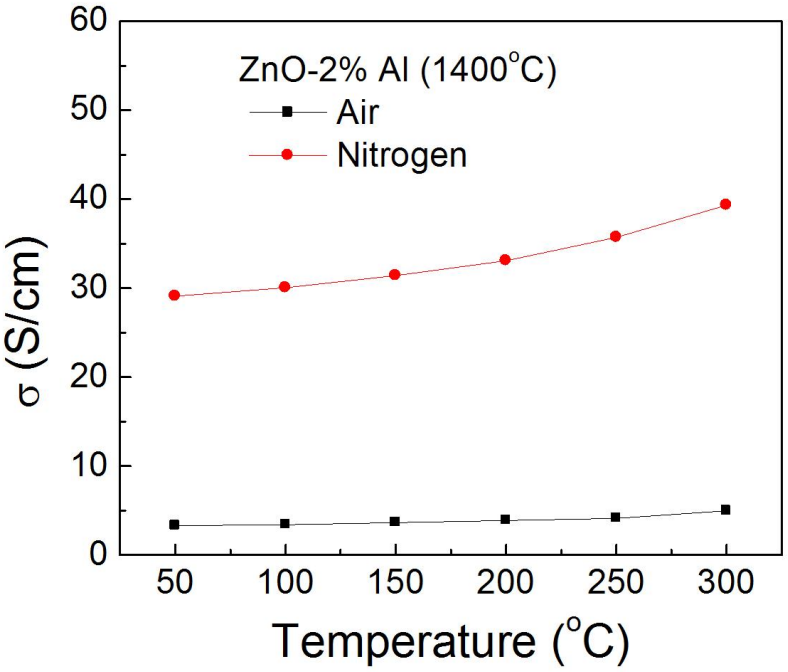

Figure 5.9 Temperature dependence of electrical conductivity of ZnO-2%Al sintered under air and nitrogen at 1400°C.

Though the value of σ of ZnO in N_2 is about 10 times of that in air. Its electrical conductivity is still low compared with good thermoelectric alloys (about 10^3 S/cm). Moreover, the high sintering temperature (1400ºC) promoted the scale of structure into micro-scale, which makes it difficult to fabricate nanostructure and reduce thermal conductivity. Using chemical synthesized doped ZnO powders would be one possibility to achieve high doping concentration at relatively low sintering temperature. The uniform and atomic level mixture of Al atoms and ZnO might improve Al doping in ZnO. In the following section lower sintering temperature (1200 ºC) was carried out under different sintering atmospheres and the sol-gel chemical synthesized ZnO-Al powder were used as starting material.

5.2.2 Effect of sintering atmosphere and chemical synthesis process on electrical conductivity

For better Al atom distribution in ZnO, the chemical synthesis uses zinc nitrate hydrate [$Zn(NO_3)_2$-$6H_2O$], aluminum nitrate hydrate [$Al(NO_3)_3$-$9H_2O$] as dopants (1, 2, 3 mole percent), oxalic acid [$(COOH)_2$-$2H_2O$] as a precursor, and ethanol as a solvent. They were mixed together to yield a viscous white gel, kept 24 hours, dried at 80 °C for 12 hours. The dry gel product was calcinated at 600°C for 2 hours under nitrogen to form ZnO-Al powders. ZnO-2%Al compacts were pressed using chemical synthesized ZnO-Al nanopowders followed by cold isostatic pressing at 200 MPa and sintered at 1200ºC, under different sintering atmospheres: air, nitrogen, 10^{-2} Torr, and 10^{-5} Torr.

The XRD spectra of this group samples are shown in Figure 5.10a. All XRD patterns confirm the formation of ZnO phase and a small fraction of $ZnAl_2O_4$ phase. The amount of $ZnAl_2O_4$ phase is small resulting in weak XRD signal, so hardly to tell the difference of amount. The figure 5.10b-e includes the SEM micrographs of sintered pellets, showing various microstructures and grain sizes. Under air condition, ZnO has grains around 5 μm, with closed pores less than 1 μm located in the corner of grains. Under nitrogen atmosphere, the structure is slight more porous and some pores exhibit long shape, more than 1 μm. The ZnO-2%Al samples sintered under vacuum conditions (10^{-2} Torr and 10^{-5} Torr) exhibit porous structures (about 70% relative density), which are because of vapor transport mechanism for grain growth under vacuum. They consist of 5-10 μm grains interspersed by nano-precipitates. Grains grew in horizontal direction, leaving cross-sectional long interspaces parallel to the sample surface. Both grain size and pore size of

ZnO-2%Al under vacuum are larger than that under air and nitrogen. The low pressure enhances vapor transport sintering mechanism, which drives the grain growth. The layered grain structure in ZnO and the grain growth mechanism have been studied and discussed in detail in Chapter 4.

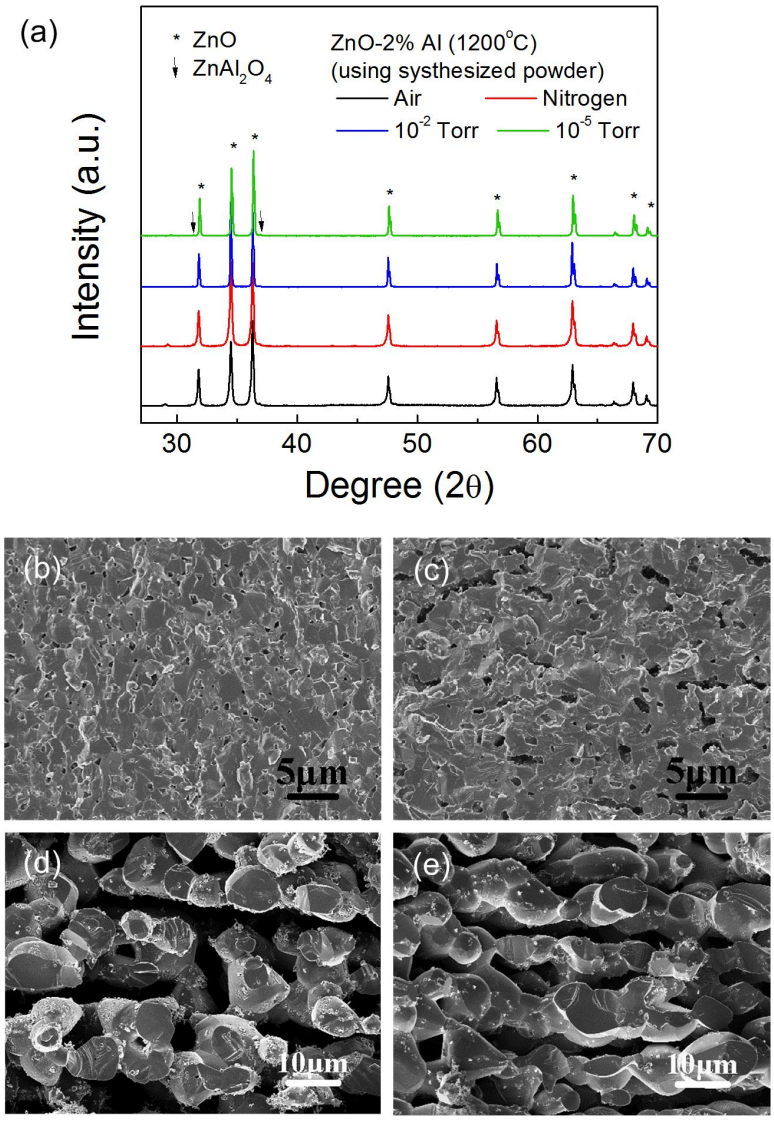

Figure 5.10 (a) XRD pattern of ZnO-2%Al sintered under different atmospheres. SEM micrographs (across section) from ZnO-2%Al pellets using sol-gel synthesized powders at 1200 °C under: (b) air, (c) nitrogen, (d) 10^{-2} Torr, and (e) 10^{-5} Torr.

The electrical conductivity of this series of samples is shown in Figure 5.11. It can been observed that the ZnO-2%Al in air exhibits very high electrical resistivity, round 10^5 Ohm cm, thus very low electrical conductivity, close to zero. The σ of ZnO-2%Al sintered under nitrogen atmosphere is about 480 S/cm at 50°C and decreases to 380 S/cm at 300°C. Comparing ZnO-2%Al sintered under air and nitrogen, the electrical conductivity of the sample in nitrogen has a tremendous improvement. The electrical conductivity of sample in nitrogen is also larger compared with ZnO-2%Al in nitrogen using ball-milled powder (Figure 5.9). Even the later one used higher sintering temperature at 1400°C. As discussed in 5.1, compared with high temperature 1400°C, relative low temperature 1200°C makes smaller amount of Al^{3+} ions occupying the Zn lattice. From this compare, the condition of ZnO powders also has effect on electrical behavior. The impact of initial physical condition (initial powders) on electrical conductivity will be discussed later.

The ZnO-2%Al pellets sintered in vacuum conditions perform even higher σ, which are 660 S/cm and 1150 S/cm at room temperature and decrease to 450 S/cm and 750 S/cm at 300°C, for 10^{-2} Torr and 10^{-5} Torr respectively. These results imply that vacuum condition helps electrical conductivity further enhancement. According to Hall Effect measurement at room temperature, ZnO-2%Al sintered under vacuum 10^{-5} Torr has highest carrier concentration 1.08×10^{20} cm^{-3}, which is higher than that of ZnO-2%Al under 10^{-2} Torr (4.93×10^{19} cm^{-3}) and under nitrogen (1.77×10^{19} cm^{-3}).

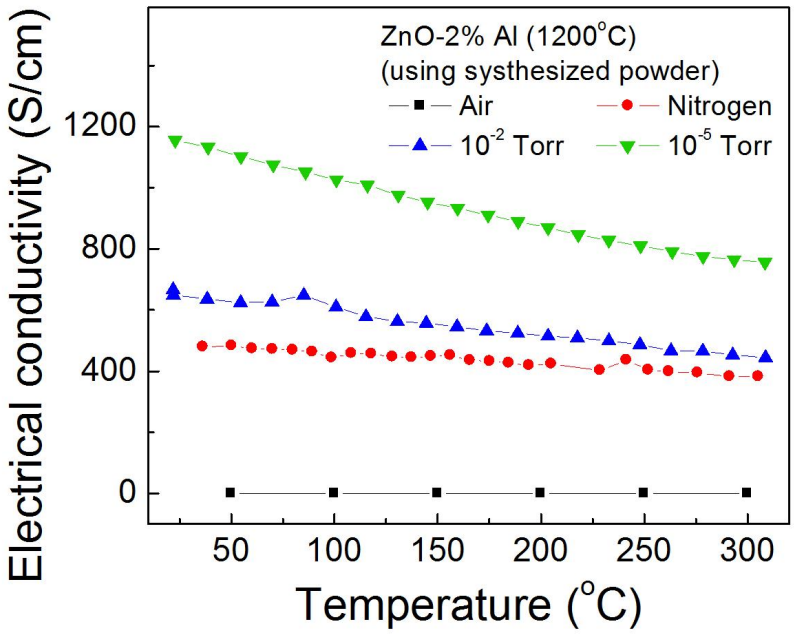

Figure 5.11 Temperature dependence of electrical conductivity of ZnO-2%Al (using synthesized powders) sintered under different atmospheres at 1200ºC.

Atmosphere together with initial physical condition is of importance on the sintering process, chemical defects, and electrical properties. As mentioned in the first comparing experiment, the sintering mechanism of ZnO involves the diffusion transfer of Zn ions from the interior of ZnO powder, giving high defect concentrations on ZnO surface. Under air atmosphere, oxygen is sufficient. O_2 reacts with Zn on surface bringing in less interstitial Zn but more Zn vacancies. The Zn vacancy has been approved as electron compensating center, which has the lowest formation energy of all of the native defects in *n*-type ZnO[107, 108]. The interstitial Zn atoms play as electron donors and are formed as[152]:

$$ZnO = Zn_i^{\times} + 1/2O_2(g) \tag{5.5}$$

High oxygen partial pressure impedes the reaction 5.5 and leads to less interstitial Zn defects. Oxygen in atmosphere also supplies the oxygen for secondary phase, which impedes the Al plays as dopant. According to another study[152], chemisorbed oxygen should be taken into account to explain the electrical property change. The chemisorbed oxygen is found to give electrons at low temperatures, and this effect is hindered in air condition[152]:

$$O_{ads}^{-} = 1/2O_2(g) + e' \quad (5.6)$$

All of above changes give rise to an extreme low electrical conductivity of ZnO-2%Al sintered with plenty oxygen.

Both nitrogen and vacuum conditions are lack of oxygen. According to previous discussion, the lack of oxygen has following functions: (1) helping interstitial Zn formation and increasing carrier concentration; (2) impeding second phase formation and improving Al doping; (3) The release of adsorbed oxygen (O^-_{ads}) at the surface of ZnO is accompanied by a release of electrons[152] at relative low temperature, which is also promoted under low oxygen partial pressure.

The vacuum environment is low-pressure condition and thereby ZnO nanopowder compact have stronger ZnO evaporation than that under nitrogen. Accordingly, the vapor transport mechanism is dominant during the sintering. Because of the low pressure at the beginning, there might be more interstitial Zn in ZnO than that sintered under nitrogen. According to the study in Chapter 4.2, the vacuumed tube was acutely filled with Zn_xO_y

gas at high sintering temperature, and Zn_xO_y deposited on the tube inside wall during cooling down. The element analysis (Table 4.1) on the particles on the tube wall reveals that there are more oxygen atoms than zinc atoms, which indicates interstitial Zn formation. Further, because of strong ZnO evaporation in tube, the atomic percentage of Al in ZnO actually increases. The atomic level mixing of Al and ZnO together with low pressure may influence the Al solubility and doping in ZnO.

To understand effect of vacuum sintering together with chemical powder synthesis process on Al doping in ZnO, different Al amounts were used in sol-gel synthesis. This group of pellets was sintered at 1200 ºC and under 10^{-2} Torr. The electrical conductivity of ZnO with 1-3 mole% Al as a function of temperature is displayed in Figure 5.12a. With higher Al amount, the σ displays larger values. At room temperature, the σ of ZnO-2%Al (666.3 S/cm) and ZnO-3%Al (856.7 S/cm) is about 3.5 and 4.5 times than that of ZnO-1%Al (193.7 S/cm). The σ of all samples decreases with increase in temperature, because of stronger carrier scattering at higher temperature when electron concentration is high. At around 500ºC, the σ of ZnO-2%Al (222.9 S/cm) and ZnO-3%Al (301.2 S/cm) becomes about 4 and 5.4 times than that of ZnO-1%Al (55.9 S/cm). According to Hall Effect measurement at room temperature, ZnO samples with more Al have higher carrier density under the vacuum sintering. The ZnO-3%Al has the carrier density 7.11×10^{19} cm^{-3}, which is larger than that of ZnO-2%Al (4.93×10^{19} cm^{-3}).

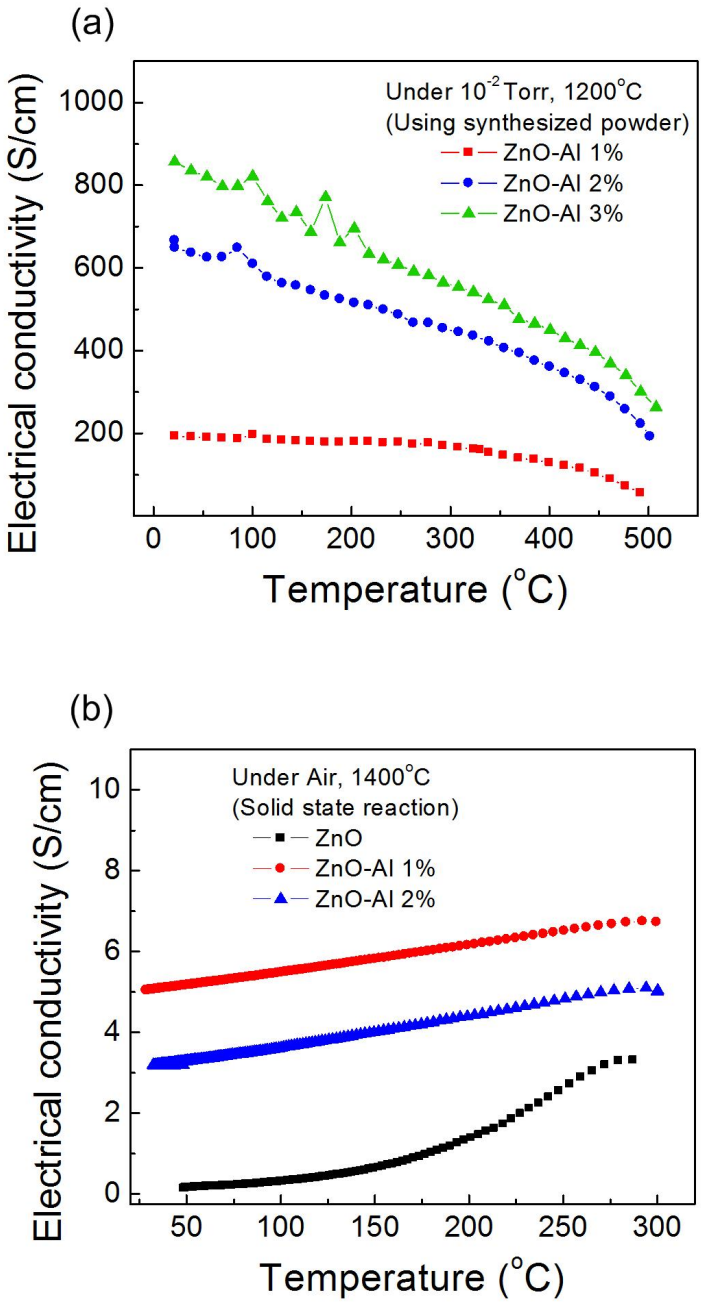

Figure 5.12 (a) Temperature dependence of electrical conductivity of ZnO-Al (using sol-gel synthesized ZnO powders with 1-3 mole% Al) sintered at 1200ºC under 10^{-2} Torr, showing increasing electrical conductivity with percentage of Al. (b) Temperature dependence of electrical conductivity of ZnO-Al (ball-milled ZnO and 0-2 mole% Al_2O_3 powders) sintered at 1400 ºC under air, as comparison.

As comparison, for the ZnO-Al sintered under air by solid-state reaction (Figure 5.12b), the σ of ZnO increases from 0% Al to 1 mole% Al and then decreases again for 2 mole% Al. The increase in amount of Al doesn't further enhance electrical conductivity. It has also been reported that adding 0.25 atom% Al leads to more than a factor of hundred higher σ_{300K} (about 350 S/m) than pure ZnO, but further Al doping amount sharply decreases σ_{300K} to about 1 S/m in air atmosphere [56]. Al doping excess of 0.25 atom % has no effect on carrier concentration increase, but a slight decrease (Figure 5.13). In this reference, compact samples were pressed using powders by chemical synthesis under microwave irradiation. Adding extra amount of Al doesn't further enhance the electrical conductivity, since the solubility of Al in ZnO is limited in air (~ 0.3 at. % at 1400°C). According to phase diagram in Figure 1.17, at lower temperature, such as 1200°C, the solubility is even lower in air condition. Under vacuum condition, however, the Al atoms additional than 1 mole% still work as dopant in ZnO, according to Figure 5.12a. More amount of Al can play as dopant in ZnO during vacuum sintering, resulting in carrier concentration and electrical conductivity enhancement.

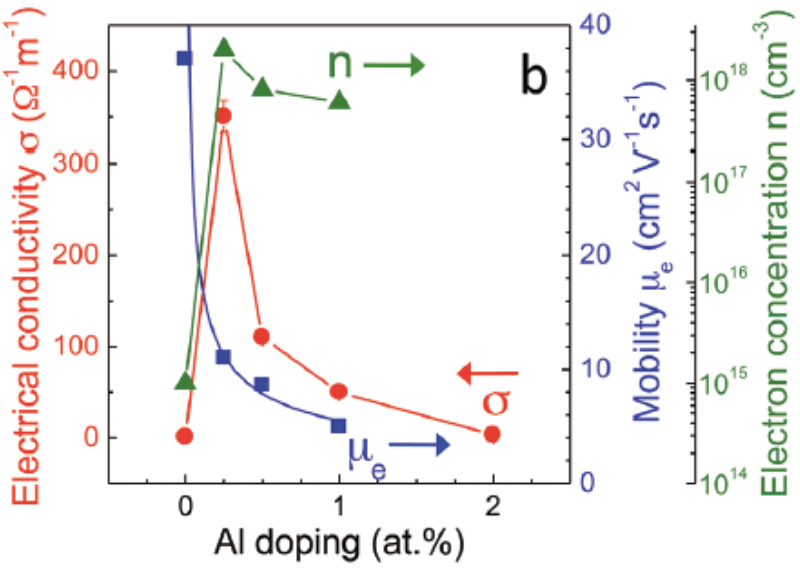

Figure 5.13 Electrical conductivity σ, electrical concentration n, and Hall mobility μ_e of ZnO nano-composite pellets as a function of Al-doping[56].

The initial physical condition is another factor in electrical conductivity variation. Comparing Figure 5.9 and Figure 5.11, it is obvious that ZnO-2%Al using chemical synthesis powders has electrical conductivity more than 10 times higher than ZnO-2%Al using ball-milled powders ZnO and Al_2O_3, both of which were sintered in nitrogen. The former was sintered at higher temperature 1400ºC than later one at 1200ºC. When both sintered at 1400ºC and under nitrogen, ZnO-2%Al bulk using chemical synthesis powders has electrical conductivity more than 30 times of ZnO-2%Al using ball-milled powders (Figure 5.14). This result indicates that using sol-gel chemical synthesis process to prepare nanopowders improves the electrical conductivity of sintered ZnO-Al bulk.

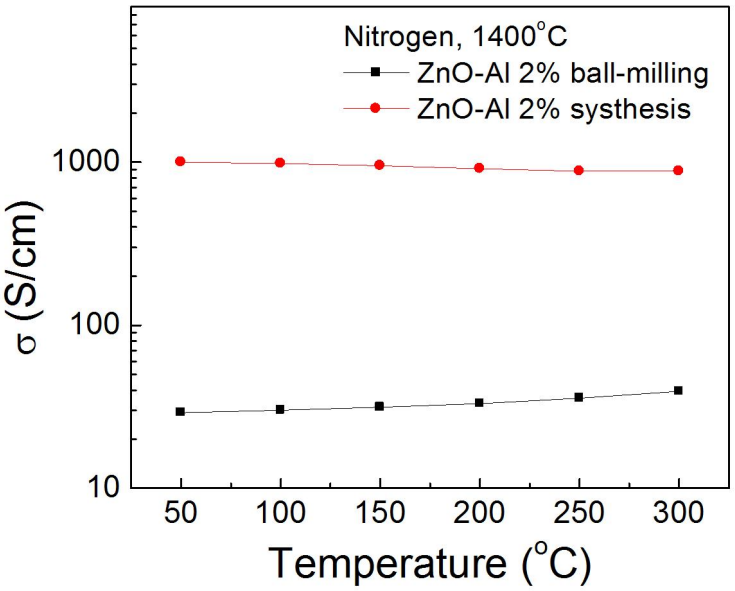

Figure 5.14 Temperature dependence of electrical conductivity of ZnO-2%Al using ball-milling and chemical synthesis starting powders.

It can be deduced that, the atomic mixing of Al atoms in ZnO and lattice imperfection in nanopowders are the factors to improve electrical conductivity. Al doping takes place inside of chemical synthesized ZnO powder at atomic level, which doesn't need to overcome the diffusion barrier. The precipitation of $ZnAl_2O_4$, on the other hand, happens through the Al aggregation. In ball-milled powders, however, the Al basically stays in Al_2O_3 powders; even they are well mixed with ZnO. The doping reaction happens on the interface of ZnO and Al_2O_3 by Al atoms diffusion. Moreover, calcination of ZnO powder was carried under nitrogen. The environment lack of oxygen causes the increase of interstitial Zn, known as electron donor.

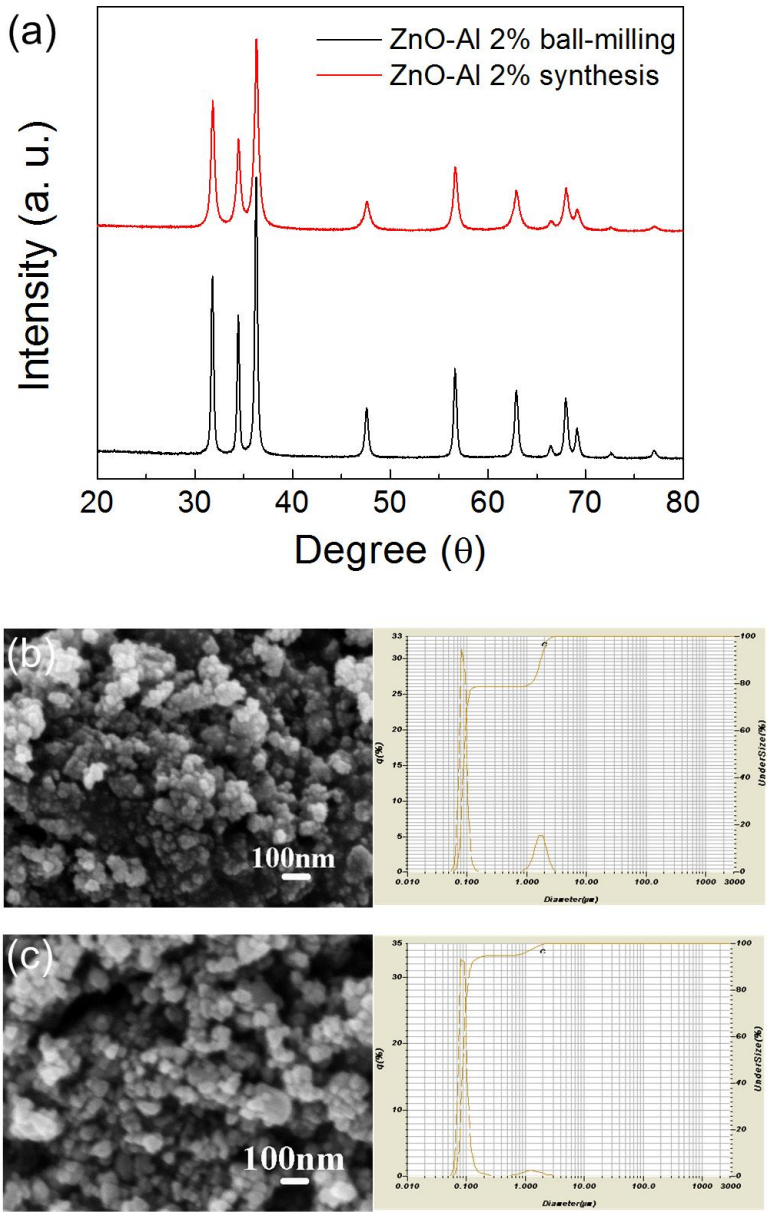

Figure 5.15 (a) XRD of ZnO-2%Al powders after ball-milling and chemical synthesis; SEM micrographs and size distributions of particles made from (b) ball-milling and (c) sol-gel chemical synthesis.

To prove the different Al status in two powders, the comparison of ZnO-Al nanopowders prepared by ball-milling and chemical synthesis is following. XRD patterns, SEM micrographs and particle size of ZnO-Al powders by chemical synthesis and by ball-milling process are displayed in Figure 5.15. The XRD patterns show that both powders are consist of only zinc oxide phase. Using chemical synthesis, the XRD peaks are broader, implying the low crystallization and imperfect lattice. Through SEM micrographs and particle size analysis, both powders are uniform in size, around 80nm. So there is no big difference of the surface ratio of two kinds of powders.

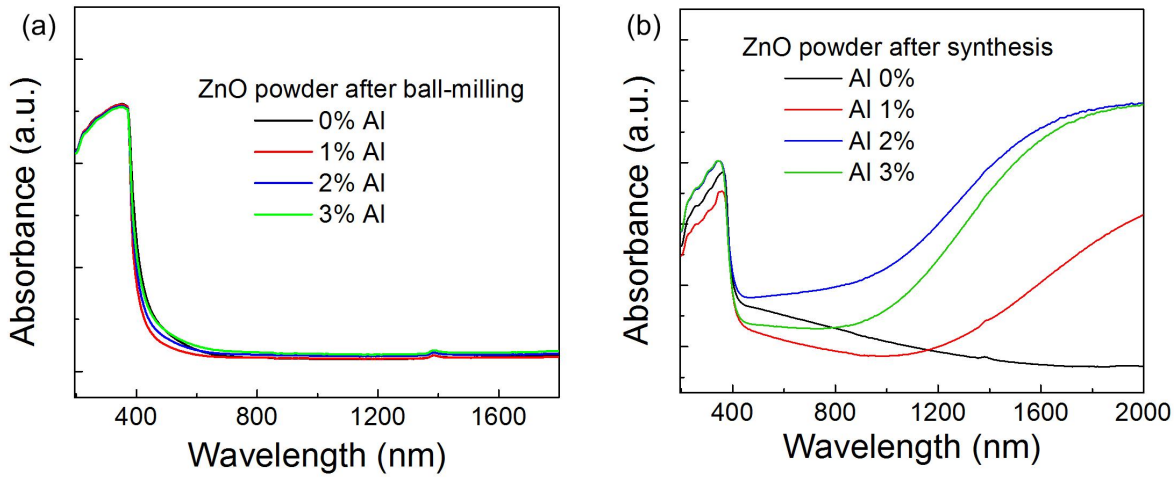

Figure 5.16 UV-VIS-NIR spectra of ZnO-*x*%Al (*x*=0-3) by (a) ball-milling and (b) sol-gel chemical synthesis.

The absorbance spectra of these two powders with different Al additions are displayed in Figure 5.16. Ball-milled ZnO-Al powders don't show negligible changes. This indicates structure of ball-milled powders is almost same as pure ZnO and Al doesn't

enter in ZnO lattice or even a little. In the case of sol-gel chemical synthesis, the absorbance curve bends up higher at high wavelength range for ZnO with Al. During synthesis process, Al^{3+} ions mix with Zn^{2+} ions in the first step, resulting in the atomic level mixing of Al atoms in ZnO. Al atoms in ZnO matrix modify the ZnO absorbance behavior, especially at high wavelength[153]. The absorbance increases from ZnO without Al to ZnO-2% Al and slightly decreases for ZnO-3%Al. It is possible that a little $ZnAl_2O_4$ has formed in ZnO-3%Al powders during calcination, which has high opacity in high wavelength range.

5.2.3 Summary

The second part of Chapter 5 discussed the effect of sintering atmosphere and starting powder on the electrical behavior of zinc oxide. With different atmosphere, ZnO-2%Al samples perform a large difference in electrical conductivity. Using ball-milled powders, ZnO-2%Al bulk sample sintered under nitrogen shows electrical conductivity 10 times of that under air. Using chemical synthesized powders, ZnO-2%Al bulk sample sintered under vacuum and nitrogen shows much higher electrical conductivity than that under air, more than 10^7 times difference. This great distinction is because of low oxygen pressure and synthesis process. Lack of oxygen improves Al to play as dopant in ZnO, and on the other hand impedes the formation of Zn^{2+} vacancy and increases the interstitial Zn. The low-pressure sintering condition further help the electrical conductivity enhancement, since more amount of Al can play as dopant in ZnO during vacuum sintering. The sol-gel chemical synthesis technique achieves the atomic level mixing of Al atoms in ZnO and therefore also improves the Al doping in ZnO.

Chapter6 Enhanced Thermoelectric Performance in PbTe-PbS Nanocomposites

In this chapter, microstructure and thermoelectric properties of $PbTe_{0.9}PbS_{0.1}$ under different thermal treatment are presented. The transmission electron microscopy (TEM) reveals the presence of nano-precipitates in the alloy as a result of annealing induced nucleation and growth. PbTe specimen with PbS phase precipitates display a significant reduction in thermal conductivity with enhanced Seebeck coefficient. The 47% reduction in lattice thermal conductivity in 400°C annealed sample is attributed to the phonon scattering on precipitates. Moreover, the annealed alloys display higher electrical conductivity at room temperature than that of melted alloy. The maximum figure of merit ZT for $PbTe_{0.9}PbS_{0.1}$ is found to be of 0.76 at 300°C.

6.1 Introduction

PbTe is good thermoelectric material with a high figure of merit around 300°C. Recently, significant efforts have been placed on the investigation of nanostructures in semiconducting thermoelectric alloys[2, 73]. PbTe-based material systems, such as LASTT ($AgPb_mSn_nSbTe_{2+m+n}$) and SALT ($NaPb_mSbTe_{2+m}$) with nano-inclusions, exhibited successful reduction in thermal conductivity supporting phonon scattering hypothesis[36, 68]. Nanodots formation in PbTe matrix has been investigated in recent years with modifiers such as Sb[37, 85, 86], Bi (BiSb)[84-86], Pb[37, 86], SnTe[87], and Ag_2Te[88]. Most precipitates in PbTe-based alloys are spontaneous formed nanocrystals, with the size between several nanometers to around 50nm, which is close to the free mean path of PbTe (19 nm)[82]. These precipitates have difference composition from matrix, resulting in lattice misfit and

large interface roughness. These nanoscale inclusions were found to block the propagation of mid-to-long-wavelength phonons hence intensely reducing the κ_{latt}.

PbTe-PbS undergoes spinodal decomposition during the heat treatment. The varying shape and sizes of structures is determined on composition and temperature of heat treatment [154]. For PbTe-*x*%PbS (*x*=4, 8, 16, 30), sample annealing at 500°C has been found to result in nanoscale coherent heterogeneities [91]. The nucleation and growth for precipitates (size < 50 nm) were observed in PbTe system with PbS composition in the range of 4%-16%[91]. While PbTe system with 16% PbS were found to have spinodal-laminated structures with the period of about 2 nm[91]. For different amounts of PbS in PbTe matrix, the boundary temperature of the solid solution and phase separation is distinct. Different annealing conditions are expected to result in varying structural changes and distinct thermoelectric performance. However, there are few studies about understanding the effect of annealing temperature on the microstructure and thermoelectric properties in PbTe-PbS alloy.

For thermoelectric materials, power factor is another important parameter of *ZT* (the product of Seebeck coefficient (α) square and electrical conductivity (σ). In PbTe-*x*%PbS alloy, the S atoms stay in two phases after secondary phase precipitation: PbTe matrix and PbS phase, playing different role in the electrical properties. The PbS secondary phase could influence carrier scattering and sulfur in PbTe matrix could modify the band structure of PbTe, both consequently modulating the electrical conductivity and Seebeck coefficient of PbTe. However, the function of S atom in PbTe-PbS alloy after heat treatment on the electrical properties is still not clear.

This study focuses on PbTe-PbS system for superior thermoelectric performance and cost-effective fabrication process. Ten-mole percent sulfur in lead is able to bring precipitates and doesn't weaken the good Seebeck coefficient of lead tellurium. We investigated the phase separation in the $PbTe_{0.9}PbS_{0.1}$ composition, which exists in the compositional regime where phase separation occurs as a result of nucleation and growth at and below 500°C[89]. The impact of annealing treatment on the nanostructure and the thermoelectric properties was analyzed.

6.2 Nanocomposites Synthesis and Analysis

Bulk $PbTe_{0.9}PbS_{0.1}$ alloy was prepared from the reaction of Pb (100 mesh, purity 99.95%, Alfa Aesar), Te (60 mesh, purity 99.999%, Alfa Aesar), and PbS (purity 99.9%, Alfa Aesar) with 0.055% PbI_2 (purity 99.9985%, Alfa Aesar) as dopant. This mixture was kept in a graphite crucible sealed in a quartz tube under high vacuum (10^{-6} Torr). The mixed powders were melted into uniform liquid in an inductive furnace for 2 min, and then rapidly cooled down. Then the alloys were further annealed at 400 and 500°C under 10^{-6} Torr vacuum for two days. Here alloy samples after 400 and 500°C annealing are referred to as PbTe-PbS-400 and PbTe-PbS-500. The sample before annealing is named as PeTe-PbS.

The $PbTe_{0.9}PbS_{0.1}$ system in this chapter is designed to have distribution of S atoms at Te lattice point in PbTe and in secondary PbS phase after annealing. The phase diagram of PbS-PbTe[89] is shown in Figure 6.1a. The composition used in this study is marked in a red line. With continuous temperature decrease, from liquid phase to solid solution, the S atoms first stay in PbTe alloy. At and under 500°C, part of S atoms stay in PbS phase.

When temperature decreases fast, the sulfur and lead atoms did not have enough time to nucleate and separate out. When alloys are annealed at temperature just below the boundary of phase transformation, Gibbs free energy drives sulfur and lead atoms to form the precipitation of PbS phase. The relatively high temperature provides energy to atoms to overcome diffusion barrier from the matrix. According to previous studies, both nucleation and growth, and the spinodal decomposition occur in $PbTe_{(1-x)}PbS_x$ alloy under annealing[91]. It is discovered that nucleation and growth occurs especially when $x < 0.16$; the spinodal decomposition regime can happen in $0.08 < x < 0.9$; both phenomena happen in $0.08 < x < 0.16$[91]. The nanocrystals formed by nucleation and growth has been reported to be more effective in scattering phonons[90, 91]. Nucleation has been considered as a kind of phase transition with large compositional difference and smaller size. The interface roughness between two phases is expected to be large in nucleation and growth along with the large compositional contrast. However, spinodal decomposition generally exhibit small compositional difference but large in extent.

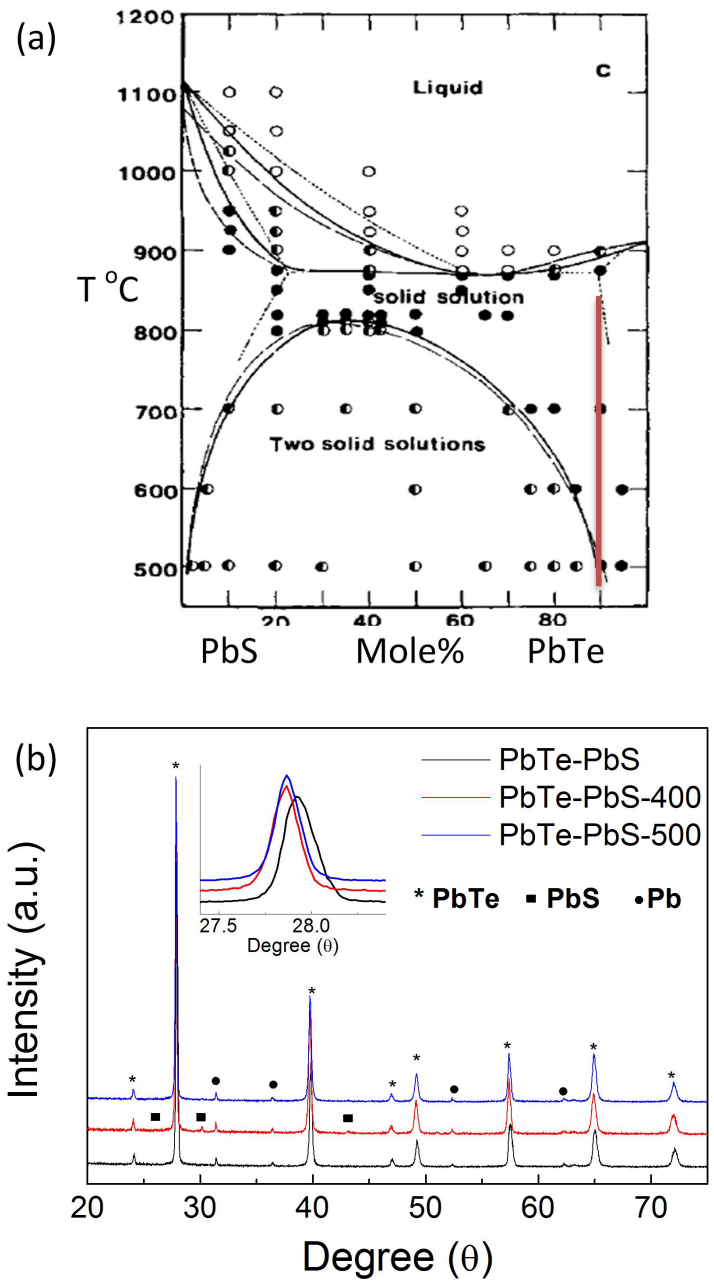

Figure 6.1 (a) The phase diagram of PbS-PbTe[155]. The red line shows the phase transformation with temperature at composition of PbTe -10% PbS; (b) XRD of melted PbTe-PbS alloy and alloys after two-day annealing. The inset is zoomed-in vision of one PbTe peak.

The XRD spectra (Figure 6.1b) were recorded from the ground alloy powders before and after annealing. These XRD patterns confirm the formation of PbTe main phase. After annealing the sample at 400°C, one can observe PbS phase as secondary phase. No obvious peaks from PbS are observed in the XRD spectra for the alloy annealed at 500°C suggesting very small amount of PbS. According to previous research, after annealing at 500°C, the existence of PbS in PbTe-PbS 8% is not visible through conventional XRD[91]. And at temperature above 500°C, the PbS was found to dissolve in the matrix of PbTe-PbS 8%[154]. Rather, in this research, the precipitation of PbS is evidenced by a shift in the major PbTe peaks toward lower value of 2θ[90], as shown in the inset of Figure 6.1b. The lattice parameters increase in PbTe alloy after annealing as a result of less substitution of S for Te in PbTe matrix. All alloys are found to contain a small amount of Pb phase as a Te deficient system because of relative low boiling temperature ~988^{o}C of Te (slight higher than the melting temperature of PbTe ~924^{o}C). Since all samples have a small amount of Pb phase, it is assumed to have similar effect on the thermoelectric properties.

In order to investigate precipitates in PbTe-PbS-400, high resolution transmission electron microscopy was performed, shown in Figure 6.2. Nano-precipitates with size less than 5 nm are homogeneously distributed in PbTe matrix as shown in Figure 6.2a. The HR-TEM image of a larger precipitate (10×20 nm) is shown in Figure 6.2b, revealing a series of dislocations at the interface as a result of the strain relaxation. As observed from this HR-TEM image, the orientation of the precipitate (please see FFT patterns from the matrix and precipitate) is different than that of the matrix, suggesting incoherent interface of the precipitate. The diffraction pattern from the precipitate and the matrix is shown in Figure 6.2c. The splitting of diffracted spots appears to be originated

from the cubic PbTe matrix and cubic PbS second phase. In PbTe-PbS-400 sample, no spinodal structure is found.

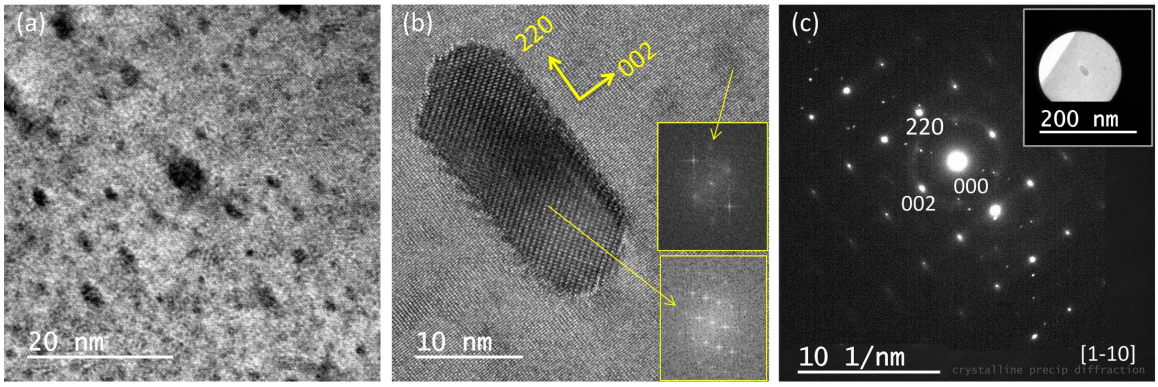

Figure 6.2 Characteristic TEM images of PbTe-PbS-400 (a) wide distributed nano-precipitates; (b) high magnification TEM image showing a precipitates having incoherent interface with PbTe matrix; the insets of (b) are FFT patterns from the precipitate and matrix shown; and (c) Electron diffraction pattern from area of a precipitates and matrix shown in the inset of (b).

6.3 Thermoelectric Properties

Figure 6.3a displays the electrical conductivity (σ) from melted and annealed PbTe-PbS samples. It can be seen that the electrical conductivity decreases with the temperature in the range of room temperature (R. T.) to 300°C. The σ of PbTe-PbS alloy is found to reduce from 1245.6 S/cm at R. T. to 559.4 S/cm at 300°C. After annealing, PbTe-PbS-400 displays slight higher σ 1290.2 S/cm at R. T., and reduce to around 415 S/cm at 300°C. PbTe-PbS-500 is found to exhibit higher value 1578.6 S/cm at R. T., but decrease rapidly to 415 S/cm at 300°C. The results indicate that annealed alloys display higher electrical conductivity at room temperature than that of melted alloy. With increasing

measurement temperature, the electrical conductivity of annealed alloys is found to decrease faster resulting in lower value at relative high temperature.

The decrease in electrical conductivity as a function of measurement temperature can be explained by assuming a power law $\sigma \approx \sigma_0 T^{\alpha}$ [37]. The exponent α extracted from the data is -1.45, -1.63, and -1.96 for PbTe-PbS, PbTe-PbS-400 and PbTe-PbS-500 alloys. For the $PbTe_{0.9}S_{0.1}$ alloy, the exponent α is larger than that of PbTe with PbS precipitates, which indicates electrical conductivity decrease slower with increasing measurement temperature for solid $PbTe_{0.9}S_{0.1}$. The Seebeck coefficient (Figure 6.3b) of annealed alloys is found to vary almost linearly with the temperature, which suggests that the carrier concentration is almost constant with temperature variation. Thereby the power exponent α is derived from the temperature dependence of carrier mobility, which is a function of scattering time. Electrons are scattered by the thermal vibrations of the lattice as well as precipitates and nuclei (for precipitates) in annealed samples. The precipitates provide the additional interface scattering, which contribute to the power exponent decrease. The PbS precipitates in PbTe-PbS-500 might be small because of small super-cooling degree, and might be effective to scatter charge carriers.

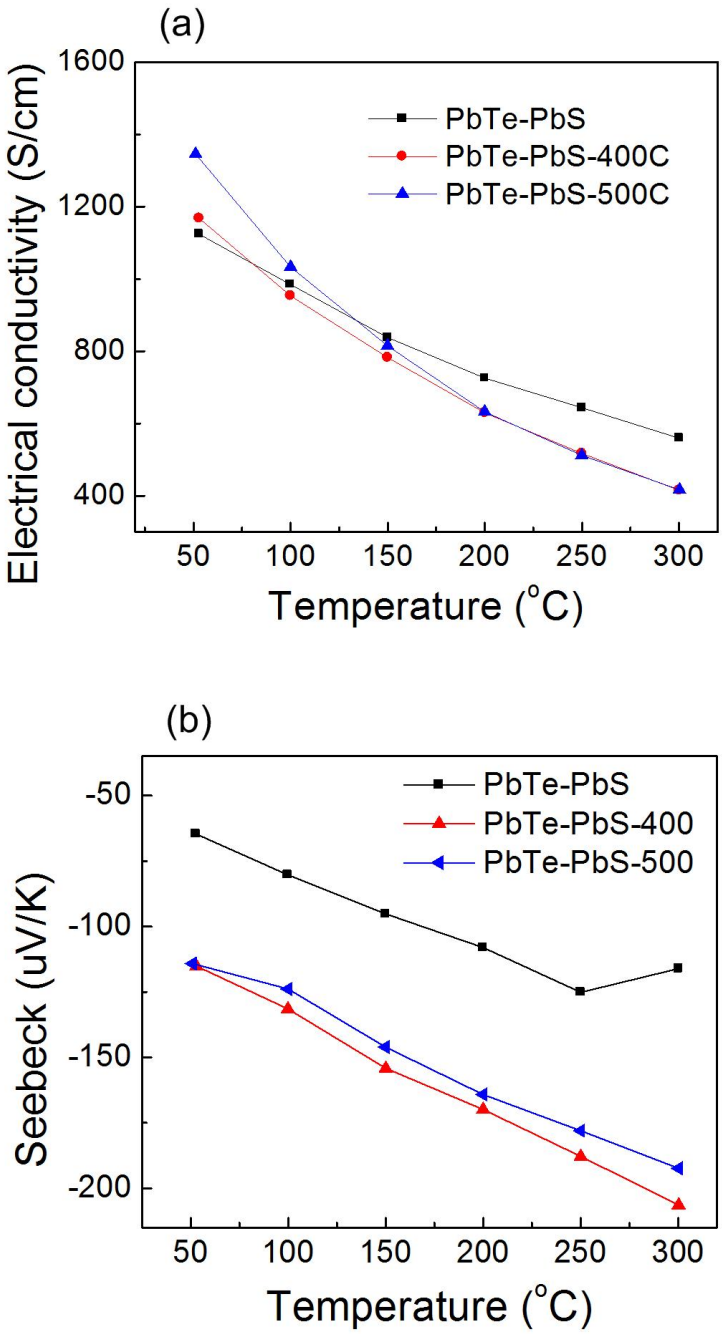

Figure 6.3 Temperature dependence of (a) Electrical conductivity, (b) Seebeck coefficient of PbTe-PbS, PbTe-PbS-400, and PbTe-PbS-500 alloys.

The carrier concentration from Hall Effect measurement at room temperature is found to be 0.99×10^{19}, 1.39×10^{19}, and 1.14×10^{19} cm^{-3} for PbTe-PbS, PbTe-PbS-400, and PbTe-PbS-500, respectively. The charge carrier concentration is higher in alloy with the PbS precipitation. The dopant of PbTe in this paper is PbI_2, which has been previously reported to be an excellent dopant for PbTe due to the similarity in atomic radii of iodine and tellurium; however, it is not considered a good dopant in PbS system because of large difference in ionic radii between iodine and sulfur[90]. With less distribution of the sulfur atoms in PbS precipitates, more iodine atoms replace the tellurium to contribute free electrons in PbTe.

Figure 6.3b presents the Seebeck coefficient (α) of PbTe-PbS alloys before and after annealing as a function of temperature. All alloys have negative Seebeck coefficients over the entire temperature range, indicating n-type conduction. The annealing process greatly improves the absolute value of Seebeck coefficient. The maximum value of α at room temperature is found to be -115 μV/K for PbTe-PbS-400, which further increases almost linearly up to -206 μV/K at 300°C. This result demonstrates that the precipitation of PbS out from PbTe matrix leads to an enhancement in the absolute value of Seebeck coefficient.

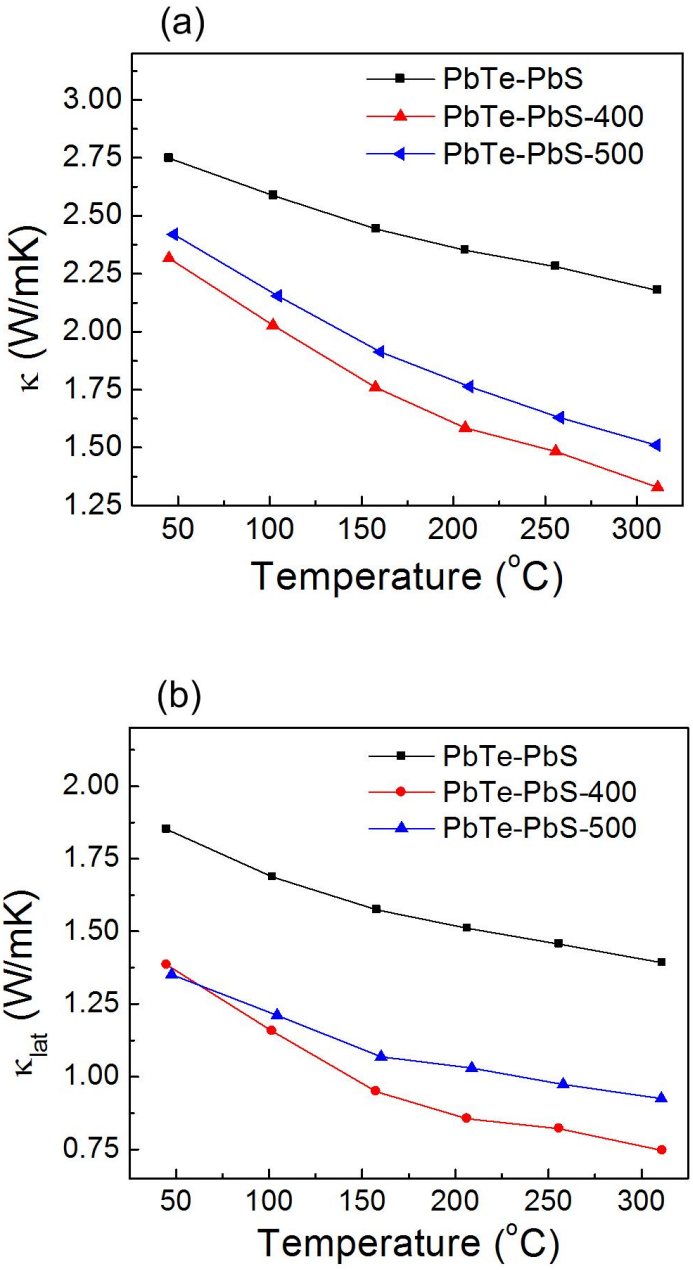

Figure 6.4 Temperature dependence of (a) thermal conductivity and (b) lattice thermal conductivity of PbTe-PbS, PbTe-PbS-400, and PbTe-PbS-500 alloys.

The thermal conductivity (κ) of annealed PbTe-PbS is smaller over the entire temperature range in comparison to that of melted PbTe-PbS (Figure 6.4a). The κ value at

300°C is found to reduce from 2.18 W/mK for PeTe-PbS to 1.51 W/mK for PbTe-PbS-500, and 1.32 W/mK for PbTe-PbS-400, suggesting a maximum 40% decrease. The derived κ_{latt} is calculated and plotted in figure 6.4b. In the temperature range of measurements, a larger reduction of κ_{latt} is observed for both PbTe-PbS-400 and PbTe-PbS-500 samples, which accounts for the overall thermal conductivity reduction. The κ_{latt} value at 300°C is observed to reduce from 1.39 W/mK for PeTe-PbS to 0.92 W/mK for PbTe-PbS-500 and 0.74 W/mK for PbTe-PbS-400, achieving maximum 47% decrease. The lower lattice thermal conductivity of both PbTe-PbS-400 and PbTe-PbS-500 is attributed to the effective phonon scattering on PbS precipitation in line with the microstructure analysis. The PbTe-PbS-400 specimen exhibits lower κ and κ_{latt} than PbTe-PbS-500 at whole measurement temperature. In PbTe-PbS-400 system, the driving force for secondary phase separation is larger even at lower annealing temperature.

The enhanced Seebeck coefficient and reduced thermal conductivity of annealed alloys have a direct impact on the thermoelectric figure of merit *ZT*, which exhibits much higher value than origin melted alloy (Figure 6.5). PbTe-PbS-500 performs ZT value up to 0.59 at 300°C, whereas PbTe-PbS-400 is found to show higher ZT value ~0.76. This ZT value is more than three times higher than that of PbTe-PbS.

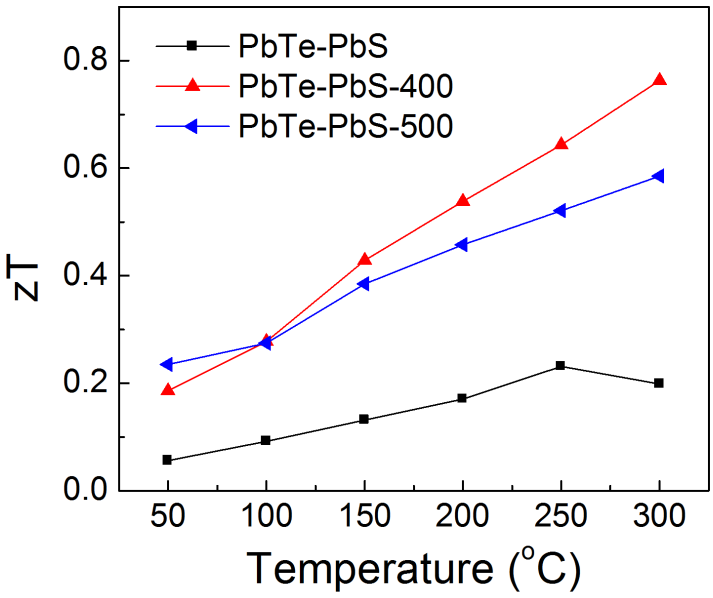

Figure 6.5 Figure of merit for PbTe-PbS, PbTe-PbS-400, and PbTe-PbS-500 alloys, as a function of measurement temperature.

6.4 Summary

In summary, this chapter has discussed the thermal treatment on $PbTe_{0.9}PbS_{0.1}$ and corresponding microstructure changes. These microstructure changes are further correlated with the thermoelectric properties improvement. The annealed alloys are found to exhibit precipitate structures as a result of nucleation and growth. After heat treatment, alloys display higher electrical conductivity than that of melted alloy at room temperature. The precipitation of PbS is found to enhance the carrier concentration in the system. Yet with increasing temperature, the decrease of electrical conductivity is faster due to scattering lead decreased mobility of charge carriers. The annealing process greatly has an impact to improve the value of Seebeck coefficient. Furthermore, PbTe-

PbS after annealing exhibits a significant decrease in thermal conductivity. The lower value of the thermal conductivity 1.32 W/mK was achieved in PbTe-PbS-400 alloy at 300 °C as a result of strong phonon scattering on nano-precipitates. These concomitant effects result in three times enhanced ZT ~ 0.76 at 300°C for 400°C annealed $PbTe_{0.9}S_{0.1}$.

Chapter7 Conclusion and Future work

7.1 Conclusion

In this study, I proposed and studied two structures in Chapter 3 and Chapter 4: precipitates and layered-correlated-grain in bulk ZnO to address the challenge of high thermal conductivity. Bulk ZnO with $ZnAl_2O_4$ nano-precipitates achieved 3-fold reduction in thermal conductivity, which is greater than that in ZnO with micron precipitates. This large κ reduction is mainly attributed to phonon confinement by nanosize precipitates. ZnO grain boundary area also has a contribution towards lowering the thermal conductivity. The bulk Al-doped ZnO with a novel self-formed layered and correlated grain structure is also found to exhibit sharp reduction in thermal conductivity. Compared with the dense ZnO-2%Al with nano-precipitates, there are 30% and 52% decreases in the thermal conductivity of ZnO-2%Al across the grain layers at 323 K and 573 K. This microstructure consists of two-dimensional layered network of oriented grains, which interconnect in third dimension through inter-planar contact, and grains are embedded with nano-precipitates as well. The mechanism of layered and correlated grain structure is mainly related to vacuum sintering, secondary phase, and compact pressing. This ZnO ceramic with layered and correlated grains provides enhanced thermoelectric performance, exhibiting figure of merit of 0.14×10^{-3} K^{-1} at 573 K.

The Chapter 5 studied the electrical property of Al-doped ZnO under the variation of temperature, atmosphere, and initial physical condition. Al atoms stay either in ZnO matrix or $ZnAl_2O_4$ secondary phase, which have different influence on the electrical

conductivity. Al doping in ZnO matrix replaces Zn and releases free electrons. While Al existing in the secondary phase $ZnAl_2O_4$ promotes the formation of Zn^{2+} vacancy under the present of oxygen and consequently decreases the carrier density. With increase in sintering temperature, higher concentration of Al incorporates in ZnO lattice, releasing electron carriers, and less Al in $ZnAl_2O_4$ promotes the formation of Zn^{2+} vacancy, leading to a great increase in electrical property. Sintering atmosphere also has a significant impact on electrical conductivity of ZnO-Al samples. At same sintering temperature, ZnO-2%Al samples sintered under vacuum and nitrogen exhibits much higher electrical conductivity than that under air. The electrical conductivity of ZnO-Al sintered in vacuum at 1200 °C is found to achieve 1000 S/cm, typical for a thermoelectric alloy. Lower oxygen pressure improves Al as dopant in ZnO and increases the interstitial Zn, and on the other hand impedes the formation of Zn^{2+} vacancy, all of which enhance the electrical conductivity. Further, sol-gel chemical synthesis technique was used to prepare starting powders, in order to synthesize ZnO with low thermal conductivity by nanostructures as well as high electrical conductivity. The sol-gel process has achieved the atomic level mixing of Al atoms in ZnO and therefore also improves the Al doping in ZnO.

Chapter 6 presents the thermal treatment on $PbTe_{0.9}PbS_{0.1}$, microstructure changes and the influence on thermoelectric properties. The annealed alloys are found to exhibit precipitate microstructure by nucleation and growth. The annealed alloys display higher electrical conductivity than that of the melted alloy at room temperature. The precipitation of PbS improves the doping and carrier concentration, but scatters the carriers especially at relative high temperature. The annealing process greatly improves

the value of Seebeck coefficient. $PbTe_{0.9}PbS_{0.1}$ alloy with nano-precipitates displayed significant decrease in the thermal conductivity. These concomitant effects result in ZT enhancement in annealed alloys.

7.2 Future Work

Further research can be on the following topics:

1. Study the electrical properties anisotropy and optimize the power factor in ZnO with layered and correlated grain structure. Since anisotropic connectivity of voids are trapped between the grain layers, the thermal conductivity across and along the grain layers is different, and the electrical properties across and along the grain layers might be distinct as well, due to different carrier mobility. The high electrical conductivity of ZnO-Al is achieved in vacuum sintering, because of high carrier concentration, which leads to relative low Seebeck coefficient. Low temperature oxygen annealing can be carried out to optimize the carrier density of ZnO with layered grain structure. Because of oxygen, the Al doping and point defects in the ZnO will change to modify the carrier density. More precipitates will uniformly appear on the surface of layered grains, which might further reduce the thermal conductivity. Further, high temperature thermoelectric properties of ZnO with layered and correlated grain structure should be tested. Thermoelectric oxides perform good property at high temperature. And sample's stability in air can be carried out.
2. Enhance the Seebeck coefficient by modifying band structure. It had been predicted and experimental proved that a distortion (resonant levels close to the Fermi level)

of the electronic density of states by doping could enhance the Seebeck coefficient in alloys. Theory work on calculating band structure of doped ZnO can predict possible dopants in ZnO to increase the slope of DOS to enhance the Seebeck. And more experimental work should be done based on the calculation result.

3. Explore thermoelectric performance on ZnO film with oriented elliptical pores. The layered and correlated grain structure in Al-doped ZnO exhibited a low thermal conductivity and promising Z value. Similarly, oriented elliptical pore structure can be produced in film ZnO in plane and the thermal conductivity in plane is expected to be low. For thermoelectric devices, maintain the temperature difference is important. Multi-layer structure in thin film has low thermal conductivity but it's tough to keep a stable temperature difference across the thin firm. If the ZnO can be made into film across the substrate with very low thermal conductivity, and oriented elliptical pores are distributed in plane, the thermal conductivity in plane is low and temperature difference is easy to control.

Reference

[1] D. M. Rowe, in *Thermoelectrics handbook : macro to nano*, edited by D. M. Rowe (Taylor & Francis Group, LLC, CRC Press, 6000 Broken Sound Parkway NW, Suite 300, Boca Raton, FL 33487-2742, 2006).

[2] G. J. Snyder and E. S. Toberer, Nat Mater **7**, 105 (2008).

[3] G. Chen, M. S. Dresselhaus, G. Dresselhaus, J. P. Fleurial, and T. Caillat, Int Mater Rev **48**, 45 (2003).

[4] J. R. Sootsman, D. Y. Chung, and M. G. Kanatzidis, Angew Chem Int Edit **48**, 8616 (2009).

[5] M. Ohtaki, T. Tsubota, K. Eguchi, and H. Arai, J Appl Phys **79**, 1816 (1996).

[6] U. Özgür, Y. I. Alivov, C. Liu, A. Teke, M. A. Reshchikov, S. Doğan, V. Avrutin, S. J. Cho, and H. Morkoç, J Appl Phys **98**, 041301 (2005).

[7] D. D. Pollock, in *CRC Handbook of Thermoelectrics*, edited by D. M. Rowe (CRC Press LLC, 2000 N.W. Corporate Blvd., Boca Raton, Florida 33431, 1995).

[8] http://en.wikipedia.org/wiki/Thermoelectric_effect.

[9] H. J. Goldsmid, in *CRC Handbook of Thermoelectrics*, edited by D. M. Rowe (CRC Press LLC, 2000 N.W. Corporate Blvd., Boca Raton, Florida 33431, 1995).

[10] H. B. Callen, *Thermodynamics* (Wiley,, New York, NY, 1985).

[11] D. Emin, in *Thermoelectrics Handbook Macro to Nano*, edited by D. M. Rowe, 6000 Broken Sound Parkway NW, Suite 300, 2006).

[12] D. K. C. MacDonald, in *Thermoelectricity*, edited by D. ed. (Dover Publications, Mineola, N.Y., 2006).

[13] C. M. Bhandari, in *CRC Handbook of Thermoelectrics*, edited by D. M. Rowe (CRC Press LLC, 2000 N.W. Corporate Blvd., Boca Raton, Florida 33431, 1995).

[14] N. F. Mott, Jones, N., *The Theory of the Properties of Metals and Alloys* (Dover, New York, NY 1958).

[15] M. Cutler, J. Leavy, and R. Fitzpatrick, Physical Review **133**, A1143 (1964).

[16] D. M. R. C. M. Bhandari, in *Thermal Conduction in Semiconductors* (University Press, Oxford, 1979).

[17] W. M. Jones, Norman H. , *Theoretical Solid State Physics* (Courier Dover Publications, 1985).

[18] J. P. Heremans, V. Jovovic, E. S. Toberer, A. Saramat, K. Kurosaki, A. Charoenphakdee, S. Yamanaka, and G. J. Snyder, Science **321**, 554 (2008).

[19] L. Hicks and M. Dresselhaus, Phys Rev B **47**, 16631 (1993).

[20] J.-F. Li, W.-S. Liu, L.-D. Zhao, and M. Zhou, NPG Asia Materials **2**, 152 (2010).

[21] R. Venkatasubramanian, E. Siivola, T. Colpitts, and B. O'Quinn, Nature **413**, 597 (2001).

[22] V. Fano, in *CRC Handbook of Thermoelectrics*, edited by D. M. Rowe (CRC Press LLC, 2000 N.W. Corporate Blvd., Boca Raton, Florida 33431, 1995).

[23] G. S. Nolas, D. T. Morelli, and T. M. Tritt, Annu Rev Mater Sci **29**, 89 (1999).

[24] C. B. Vining, in *CRC Handbook of Thermoelectrics*, edited by D. M. Rowe (CRC Press LLC, 2000 N.W. Corporate Blvd., Boca Raton, Florida 33431, 1995).

[25] I. Terasaki, Y. Sasago, and K. Uchinokura, Phys Rev B **56**, 12685 (1997).

[26] M. Shikano and R. Funahashi, Applied Physics Letters **82**, 1851 (2003).

[27] T. Okuda, K. Nakanishi, S. Miyasaka, and Y. Tokura, Phys Rev B **63** (2001).

[28] T. C. Harman, P. J. Taylor, M. P. Walsh, and B. E. LaForge, Science **297**, 2229 (2002).

[29] T. C. Harman, D. L. Spears, and M. J. Manfra, J Electron Mater **25**, 1121 (1996).

[30] A. I. Hochbaum, R. Chen, R. D. Delgado, W. Liang, E. C. Garnett, M. Najarian, A. Majumdar, and P. Yang, Nature **451**, 163 (2008).

[31] A. I. Boukai, Y. Bunimovich, J. Tahir-Kheli, J. K. Yu, W. A. Goddard, 3rd, and J. R. Heath, Nature **451**, 168 (2008).

[32] G. Pernot, et al., Nat Mater **9**, 491 (2010).

[33] B. Poudel, et al., Science **320**, 634 (2008).

[34] W. Xie, X. Tang, Y. Yan, Q. Zhang, and T. M. Tritt, J Appl Phys **105**, 113713 (2009).

[35] D. Y. Chung, T. P. Hogan, M. Rocci-Lane, P. Brazis, J. R. Ireland, C. R. Kannewurf, M. Bastea, C. Uher, and M. G. Kanatzidis, J Am Chem Soc **126**, 6414 (2004).

[36] K. F. Hsu, S. Loo, F. Guo, W. Chen, J. S. Dyck, C. Uher, T. Hogan, E. K. Polychroniadis, and M. G. Kanatzidis, Science **303**, 818 (2004).

[37] J. R. Sootsman, H. Kong, C. Uher, J. J. D'Angelo, C. I. Wu, T. P. Hogan, T. Caillat, and M. G. Kanatzidis, Angewandte Chemie **47**, 8618 (2008).

[38] G. C. Christakudis, S. K. Plachkova, L. E. Shelimova, and E. S. Avilov, Phys Status Solidi A **128**, 465 (1991).

[39] P. F. Poudeu, J. D'Angelo, A. D. Downey, J. L. Short, T. P. Hogan, and M. G. Kanatzidis, Angewandte Chemie **45**, 3835 (2006).

[40] S. N. Girard, J. He, X. Zhou, D. Shoemaker, C. M. Jaworski, C. Uher, V. P. Dravid, J. P. Heremans, and M. G. Kanatzidis, J Am Chem Soc **133**, 16588 (2011).

[41] K. Biswas, J. He, G. Wang, S.-H. Lo, C. Uher, V. P. Dravid, and M. G. Kanatzidis, Energy & Environmental Science **4**, 4675 (2011).

[42] K. Ahn, M. K. Han, J. He, J. Androulakis, S. Ballikaya, C. Uher, V. P. Dravid, and M. G. Kanatzidis, J Am Chem Soc **132**, 5227 (2010).

[43] K. Biswas, J. He, I. D. Blum, C. I. Wu, T. P. Hogan, D. N. Seidman, V. P. Dravid, and M. G. Kanatzidis, Nature **489**, 414 (2012).

[44] K. Kurosaki, A. Kosuga, H. Muta, M. Uno, and S. Yamanaka, Applied Physics Letters **87**, 061919 (2005).

[45] X. Shi, et al., J Am Chem Soc **133**, 7837 (2011).

[46] W. Y. Zhao, P. Wei, Q. J. Zhang, C. L. Dong, L. S. Liu, and X. F. Tang, J Am Chem Soc **131**, 3713 (2009).

[47] S. R. Brown, S. M. Kauzlarich, F. Gascoin, and G. J. Snyder, Chem Mater **18**, 1873 (2006).

[48] X. W. Wang, et al., Applied Physics Letters **93**, 193121 (2008).

[49] T. Caillat, J. P. Fleurial, and A. Borshchevsky, J Phys Chem Solids **58**, 1119 (1997).

[50] A. Saramat, et al., J Appl Phys **99**, 023708 (2006).

[51] S. Sakurada and N. Shutoh, Applied Physics Letters **86**, 082105 (2005).

[52] H. L. Liu, et al., Nat Mater **11**, 422 (2012).

[53] N. Van Nong, N. Pryds, S. Linderoth, and M. Ohtaki, Adv Mater **23**, 2484 (2011).

[54] S. Ohta, T. Nomura, H. Ohta, M. Hirano, H. Hosono, and K. Koumoto, Applied Physics Letters **87**, 092108 (2005).

[55] M. Ohtaki, K. Araki, and K. Yamamoto, J Electron Mater **38**, 1234 (2009).

[56] P. Jood, R. J. Mehta, Y. Zhang, G. Peleckis, X. Wang, R. W. Siegel, T. Borca-Tasciuc, S. X. Dou, and G. Ramanath, Nano letters **11**, 4337 (2011).

[57] U. S. D. O. ENERGY, 2011).

[58] K. H. Kim, S. H. Shim, K. B. Shim, K. Niihara, and J. Hojo, J Am Ceram Soc **88**, 628 (2005).

[59] M. Ohtaki and R. Hayashi, ICT'06: XXV International Conference on Thermoelectrics, Proceedings, 276 (2006).

[60] M. Ohtaki, S. Maehara, and S. Shige, Twenty-Second International Conference on Thermoelectrics, Proceedings Ict '03, 171 (2003).

[61] M. Ohtaki, H. Koga, T. Tokunaga, K. Eguchi, and H. Arai, J Solid State Chem **120**, 105 (1995).

[62] M. Ohtaki, D. Ogura, K. Eguchi, and H. Arai, Journal of Materials Chemistry **4**, 653 (1994).

[63] S. W. Li, R. Funahashi, I. Matsubara, K. Ueno, and H. Yamada, Journal of Materials Chemistry **9**, 1659 (1999).

[64] Y. Masuda, D. Nagahama, H. Itahara, T. Tani, W. S. Seo, and K. Koumoto, Journal of Materials Chemistry **13**, 1094 (2003).

[65] Y. Wang, Y. Sui, J. Cheng, X. Wang, and W. Su, Journal of Alloys and Compounds **477**, 817 (2009).

[66] Y. Zhang, J. Zhang, and Q. Lu, Journal of Alloys and Compounds **399**, 64 (2005).

[67] A. A. Balandin, Journal of Nanoscience and Nanotechnology **5**, 1015 (2005).

[68] R. Venkatasubramanian, Phys Rev B **61** (2000).

[69] S. K. Saha, The University of Texas at Austin, 2007.

[70] P. Martin, Z. Aksamija, E. Pop, and U. Ravaioli, Physical Review Letters **102** (2009).

[71] J. M. Ziman, *Electrons and Phonons* (University Press, Oxford, 1979).

[72] M. Razeghi, *Fundamentals of Solod State Engineering* (Springer, 2009).

[73] C. J. Vineis, A. Shakouri, A. Majumdar, and M. G. Kanatzidis, Adv Mater **22**, 3970 (2010).

[74] L. Hicks and M. Dresselhaus, Phys Rev B **47**, 12727 (1993).

[75] S. M. Lee, D. G. Cahill, and R. Venkatasubramanian, Applied Physics Letters **70**, 2957 (1997).

[76] S. T. Huxtable, et al., Applied Physics Letters **80**, 1737 (2002).

[77] G. D. M. Per Hyldgaard, Phys Rev B **56**, 4 (1997).

[78] J. C. Caylor, K. Coonley, J. Stuart, T. Colpitts, and R. Venkatasubramanian, Applied Physics Letters **87**, 023105 (2005).

[79] W. S. Capinski and H. J. Maris, Physica B **219-20**, 699 (1996).

[80] W. Kim, et al., Applied Physics Letters **88**, 242107 (2006).

[81] T. C. Harman, P. J. Taylor, D. L. Spears, and M. P. Walsh, J Electron Mater **29**, L1 (2000).

[82] Y. K. Koh, C. J. Vineis, S. D. Calawa, M. P. Walsh, and D. G. Cahill, Applied Physics Letters **94**, 153101 (2009).

[83] M. Fardy, A. I. Hochbaum, J. Goldberger, M. M. Zhang, and P. Yang, Advanced Materials **19**, 3047 (2007).

[84] J. Androulakis, K. F. Hsu, R. Pcionek, H. Kong, C. Uher, J. J. D'Angelo, A. Downey, T. Hogan, and M. G. Kanatzidis, Advanced Materials **18**, 1170 (2006).

[85] A. Gueguen, P. F. P. Poudeu, C. P. Li, S. Moses, C. Uher, J. Q. He, V. Dravid, K. A. Paraskevopoulos, and M. G. Kanatzidis, Chem Mater **21**, 1683 (2009).

[86] J. Q. He, J. R. Sootsman, S. N. Girard, J. C. Zheng, J. G. Wen, Y. M. Zhu, M. G. Kanatzidis, and V. P. Dravid, J Am Chem Soc **132**, 8669 (2010).

[87] J. Q. He, A. Gueguen, J. R. Sootsman, J. C. Zheng, L. J. Wu, Y. M. Zhu, M. G. Kanatzidis, and V. P. Dravid, J Am Chem Soc **131**, 17828 (2009).

[88] Y. Pei, N. A. Heinz, A. LaLonde, and G. J. Snyder, Energy & Environmental Science **4**, 3640 (2011).

[89] S.-H. Lo, J. He, K. Biswas, M. G. Kanatzidis, and V. P. Dravid, Advanced Functional Materials **22**, 5175 (2012).

[90] S. N. Girard, J. He, C. Li, S. Moses, G. Wang, C. Uher, V. P. Dravid, and M. G. Kanatzidis, Nano letters **10**, 2825 (2010).

[91] J. Androulakis, et al., J Am Chem Soc **129**, 9780 (2007).

[92] K. Biswas, J. Q. He, Q. C. Zhang, G. Y. Wang, C. Uher, V. P. Dravid, and M. G. Kanatzidis, Nat Chem **3**, 160 (2011).

[93] H. Itahara, W. S. Seo, S. Lee, H. Nozaki, T. Tani, and K. Koumoto, J Am Chem Soc **127**, 6367 (2005).

[94] V. S. S. D. M. Rowe, N. Savvides, Nature **290**, 2 (1981).

[95] C.-N. Liao and T.-H. She, Thin Solid Films **515**, 8059 (2007).

[96] R. C. H. J. F. Miller, Journal of the electrochemical society **107**, 5 (1960).

[97] T. Ikeda, V. Ravi, and G. Snyder, Acta Materialia **57**, 666 (2009).

[98] T. Ikeda, L. A. Collins, V. A. Ravi, F. S. Gascoin, S. M. Haile, and G. J. Snyder, Chem Mater **19**, 763 (2007).

[99] K. P. Ong, D. J. Singh, and P. Wu, Phys Rev B **83** (2011).

[100] T. Tsubota, M. Ohtaki, K. Eguchi, and H. Arai, Journal of Materials Chemistry **7**, 85 (1997).

[101] L. Han, L. T. Hung, N. Nong, N. Pryds, and S. Linderoth, J Electron Mater **42**, 1573 (2012).

[102] M. Søndergaard, E. D. Bøjesen, K. A. Borup, S. Christensen, M. Christensen, and B. B. Iversen, Acta Materialia **61**, 3314 (2013).

[103] Y. Kinemuchi, M. Mikami, K. Kobayashi, K. Watari, and Y. Hotta, J Electron Mater **39**, 2059 (2009).

[104] T. Teranishi, Y. Mori, H. Hayashi, A. Kishimoto, and X. D. Zhou, J Am Ceram Soc **95**, 690 (2012).

[105] J. Boor, D. S. Kim, X. Ao, M. Becker, N. F. Hinsche, I. Mertig, P. Zahn, and V. Schmidt, Applied Physics A **107**, 789 (2012).

[106] Z. Wang, A. Kulkarni, S. Deshpande, T. Nakamura, and H. Herman, Acta Materialia **51**, 5319 (2003).

[107] M. Willander, O. Nur, J. R. Sadaf, M. I. Qadir, S. Zaman, A. Zainelabdin, N. Bano, and I. Hussain, Materials **3**, 2643 (2010).

[108] X. J. Wang, L. S. Vlasenko, S. J. Pearton, W. M. Chen, and I. A. Buyanova, Journal of Physics D: Applied Physics **42**, 175411 (2009).

[109] K. F. Cai, E. Müller, C. Drašar, and A. Mrotzek, Materials Science and Engineering: B **104**, 45 (2003).

[110] K. Shirouzu, T. Ohkusa, M. Hotta, N. Enomoto, and J. Hojo, J Ceram Soc Jpn **115**, 254 (2007).

[111] J. P. Han, P. Q. Mantas, and A. M. R. Senos, J Eur Ceram Soc **21**, 1883 (2001).

[112] D. Bérardan, C. Byl, and N. Dragoe, J Am Ceram Soc **93**, 2352 (2010).

[113] K.-H. Jung, S.-M. Choi, C.-H. Lim, W.-S. Seo, and H.-H. Park, Surface and Interface Analysis **44**, 1507 (2012).

[114] K. Park and K. Y. Ko, Journal of Alloys and Compounds **430**, 200 (2007).

[115] H. Wang, X. Dong, S. Peng, L. Dong, and Y. Wang, Journal of Alloys and Compounds **527**, 204 (2012).

[116] K. Park and J. K. Seong, Journal of Alloys and Compounds **464**, 1 (2008).

[117] K. Park, J. K. Seong, and S. Nahm, Journal of Alloys and Compounds **455**, 331 (2008).

[118] Z. Zhan, J. Zhang, Q. Zheng, D. Pan, J. Huang, F. Huang, and Z. Lin, Crystal Growth & Design **11**, 21 (2011).

[119] A. J. Kulkarni and M. Zhou, Applied Physics Letters **88**, 141921 (2006).

[120] M. Rajalakshmi, A. K. Arora, B. S. Bendre, and S. Mahamuni, J Appl Phys **87**, 2445 (2000).

[121] V. A. Fonoberov and A. A. Balandin, physica status solidi (c) **1**, 2650 (2004).

[122] V. Fonoberov and A. Balandin, Phys Rev B **70** (2004).

[123] K. A. Alim, V. A. Fonoberov, and A. A. Balandin, Applied Physics Letters **86** (2005).

[124] J. Zou and A. Balandin, J Appl Phys **89**, 2932 (2001).

[125] A. Kumar and J. Kumar, J Phys Chem Solids **69**, 2764 (2008).

[126] G. P. L.F. Norris, J. Am. Ceram. Soc. **46**, 4 (1963).

[127] M. N. Rahaman, *Ceramic Processing* (CRC Press, Taylor& Francis Group, 6000 Broken Sound Parkway NW, Suite 300, 2007).

[128] Y. Y. Liu, L. Q. Chen, and J. Y. Li, Acta Materialia **65**, 308 (2014).

[129] S. J. a. K. G. E. Glass, in *Compaction Science and Technology MRS Bulleting*, 1977), p. 24.

[130] J. G. A. e. K.G. Ewsuk, D.N. Bencoe, D.T. Ellerby, S. J. Glass, D. H. Zeuch, and J.Anderson, in *Improved Ceramics through New Measurements, Processing, and Standards* (Wiley-American Ceramic Society, 735 Ceramic Place Westerville, Ohio 43081, United States, 2002).

[131] G. S. P Joos, Journal of Colloid and Interface Science **145**, 291 (1991).

[132] Y. Zhao, Y. K. Yan, A. Kumar, H. Wang, W. D. Porter, and S. Priya, in *J Appl Phys*, 2012), Vol. 112.

[133] Y. Zhao, A. Kumar, G. A. Khodaparast, A. Eltahir, H. Wang, and S. Priya, Energy Harvesting and Systems **0** (2014).

[134] P. G. Klemens, in *ETPC Procedings*, 1991).

[135] B. Shafiro and M. Kachanov, J Appl Phys **87**, 8561 (2000).

[136] L. Braginsky, V. Shklover, G. Witz, and H. P. Bossmann, Phys Rev B **75** (2007).

[137] R. C. B. Tetsuya Senda, . Am. Ceram.Soc.. **73**, 106 (1990).

[138] J. H. H. J. Lee, J. J. Mashek, T. O. Mason, A. E. Miller, and R. W. Siegel, Materials Research Society **10**, 2295 (1995).

[139] S. Hartner, M. Ali, C. Schulz, M. Winterer, and H. Wiggers, Nanotechnology **20**, 445701 (2009).

[140] R. Shao, S. V. Kalinin, and D. A. Bonnell, Applied Physics Letters **82**, 1869 (2003).

[141] E. Burstein, Physical Review **93**, 632 (1954).

[142] B. Sernelius, K. F. Berggren, Z. C. Jin, I. Hamberg, and C. Granqvist, Phys Rev B **37**, 10244 (1988).

[143] O. Lupan, S. Shishiyanu, V. Ursaki, H. Khallaf, L. Chow, T. Shishiyanu, V. Sontea, E. Monaico, and S. Railean, Solar Energy Materials and Solar Cells **93**, 1417 (2009).

[144] T. M. Borseth, B. G. Svensson, A. Y. Kuznetsov, P. Klason, Q. X. Zhao, and M. Willander, Applied Physics Letters **89**, 262112 (2006).

[145] K. Vanheusden, C. H. Seager, W. L. Warren, D. R. Tallant, and J. A. Voigt, Applied Physics Letters **68**, 403 (1996).

[146] H. Matsudo, K.-i. Kakimoto, and I. Kagomiya, Japanese Journal of Applied Physics **49**, 09MC07 (2010).

[147] Y. Yan, A. Kumar, M. Correa, K.-H. Cho, R. S. Katiyar, and S. Priya, Applied Physics Letters **100**, 152902 (2012).

[148] A. V. Singh, J Appl Phys **95**, 3640 (2004).

[149] L. F. N. a. G. Parravno, J Am Ceram Soc **46**, 449 (1963).

[150] T. K. G. a. R. L. Coble, J Am Ceram Soc **51**, 521 (1968).

[151] V. J. Lee and G. Parravano, J Appl Phys **30**, 1735 (1959).

[152] D. T. Msasuke Takata, and Hiroaki Yanagida, J Am Ceram Soc **59**, 4 (1975).

[153] Y. Qu, Journal of Vacuum Science & Technology A: Vacuum, Surfaces, and Films **11**, 996 (1993).

[154] S. N. Girard, K. Schmidt-Rohr, T. C. Chasapis, E. Hatzikraniotis, B. Njegic, E. M. Levin, A. Rawal, K. M. Paraskevopoulos, and M. G. Kanatzidis, Advanced Functional Materials **23**, 747 (2013).

[155] L. L. Y. C. H. Liu, Mineralogical Magazine **58** (1994).